Physical and Chemical Sciences Center

Research Briefs

2003

Sandia National Laboratories
Albuquerque, New Mexico

A Department of Energy Multiprogram Laboratory

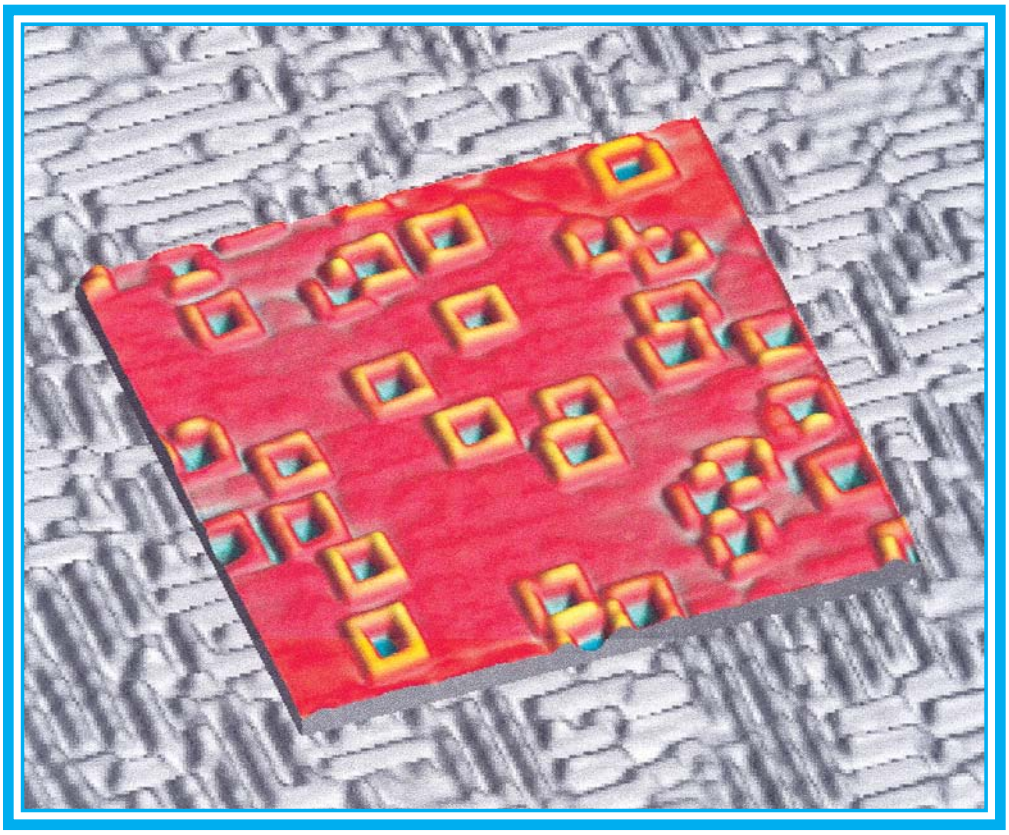

Research Briefs for the Physical and Chemical Sciences Center is published by Sandia National Laboratories. Additional complimentary copies are available by contacting:

Julia M. Phillips
Physical and Chemical Sciences Center, 1100
Sandia National Laboratories
Albuquerque, NM 87185-1427

Phone: (505) 844-1071
Fax: (505) 844-6098
E-mail: jmphill@sandia.gov
url: http://www.sandia.gov/1100/Xcenter1.htm

Research Briefs

Editors
J. M. Phillips
J. A. Nichelason

Production
M. Sheila Wilson

Cover Page: The foreground shows self-assembled quantum dot molecules (QDMs) formed in strained SiGe films. These structures are being investigated as computing elements in quantum cellular automata logic schemes. The background image shows a circuit-like self-assembly with computing elements (QDMs), storage elements (individual quantum dots) and interconnects (quantum wires). While this structure is random , it demonstrates proof-of-principle for assembling complex structures via simple control over growth kinetics. See pages 28 & 29 for further details.

Message from the Director

The Physical and Chemical Sciences Center provides new scientific knowledge in support of Sandia's mission areas–nuclear weapons, energy and infrastructure assurance, nonproliferation and assessments, military technology and applications, and homeland security. We provide science-based solutions for the mission needs of our parent agency, the National Nuclear Security Administration (NNSA), particularly in areas where we have unique expertise. Of equal importance, we also perform focused long-term research in areas that are most likely to have impact on future Sandia missions and national security, particularly in the physical, chemical, and biological sciences that will enable future microsystems. To this end, we focus on six technical thrusts: optical sciences, nanosciences, compound semiconductors, biotechnology, collective hierarchical systems, and science-based solutions for NNSA mission needs. This volume highlights representative research in all of these areas of emphasis.

The activities of the Physical and Chemical Sciences Center are supported by a diverse set of funding sources that reflect the broad impact of our work, both scientifically and programmatically. The research described in this volume illustrates the importance of a strong science base in the physical and chemical sciences for the success of the Department of Energy's various missions. Throughout this work, we have benefited immeasurably from our partnerships with colleagues across the labs, in universities, and in industry. We gratefully acknowledge their collaboration.

We appreciate your interest in our work and welcome your comments and inquiries.

Julia M. Phillips
Director

Table of Contents

Science-Based Solutions for NNSA Mission Needs

Wide Bandgap Compound Semiconductor Science

Nanoscale Structures, Phenomena, and Devices

Science of Surfaces and Interfaces

Table of Contents

Science-Based Solutions for NNSA Mission Needs

Aging of Anti-Stiction, Anti-Friction Self-Assembled Monolayers (SAMs) for Microsystem Interfaces

by B. C. Bunker, T. M. Mayer, M. de Boer, M. Hankins, J. E. Houston, W. L. Smith, B. I. Kim, and K. Crown

Motivation—Excessive interfacial interactions can lock parts together (stiction) or cause high levels of friction in micro-machines (MEMS devices). The current strategy for minimizing friction and stiction involves coating surfaces with thin organic coatings called self-assembled monolayers (SAMS). Unfortunately, desired coating properties are known to degrade with time, particularly if parts are stored in humid environments. The goals of this research are to determine the rate at which film properties change in aggressive environments, probe mechanisms for these "dormancy effects", and identify strategies for developing coatings that are optimized to provide long-term stability.

Accomplishment—SAMS deteriorate in humid environments due to: 1) attack by water of the bonds between the coating and substrate, and 2) rearrangement of molecules within the coating to uncover sticky components (either functional groups used to anchor the SAM to the surface or bare patches in the coating). We are currently evaluating the stability of a range of SAM coatings in which surface anchors, hydrocarbon structures, and processing conditions are varied. Accelerated aging tests have been conducted in which SAMS are exposed for various times to high relative humidities (RH) and elevated temperatures. Changes in coating morphologies have been monitored using atomic force microscopy (AFM). Changes in the adhesive properties of the SAM surfaces have been monitored using a scanning probe system developed at Sandia called the interfacial force microscope (IFM). Results obtained to date indicate that most coatings are unstable in humid environments. AFM results (Fig. 1) suggest that water penetrates the SAMS and disrupts the bonding at the SAM-substrate interface to form spherical blisters (Fig. 1a) or interconnected networks (Fig. 1b). The IFM results confirm that restructuring in humid environments also leads to dramatic increases in the adhesive character of the SAM surfaces (Fig. 2).

Significance—Many SAM coatings used to coat micromachine surfaces are more susceptible to damage in humid environments than initially expected. Some coatings are compromised after only two weeks at 50°C and high humidity. While aging is accelerated at high temperatures and humidities, the dependence of degradation on temperature and humidity is complex. For example, at 100% RH, coatings tend to deteriorate more rapidly at 50°C than at 80°C. Aging effects do not necessarily follow expectations as a function of film composition and processing conditions. For example, films that have been annealed to promote formation of covalent Si-O-Si bonds can degrade faster than unannealed films that are only attached to the surface with hydrogen bonds. More research will be required to unravel the key parameters, such as the kinetics of water diffusion into and out of the films, water concentrations within the films and at the SAM-substrate interface, and interfacial reaction rates in order to develop new coatings to promote long-term stability.

Sponsors for various phases of this work include: Laboratory Directed Research & Development
Contact: Bruce C. Bunker, Biomolecular Materials and Interfaces, Dept. 1141
Phone: (505) 284-6892, Fax: (505) 844-5470, E-mail: bcbunke@sandia.gov

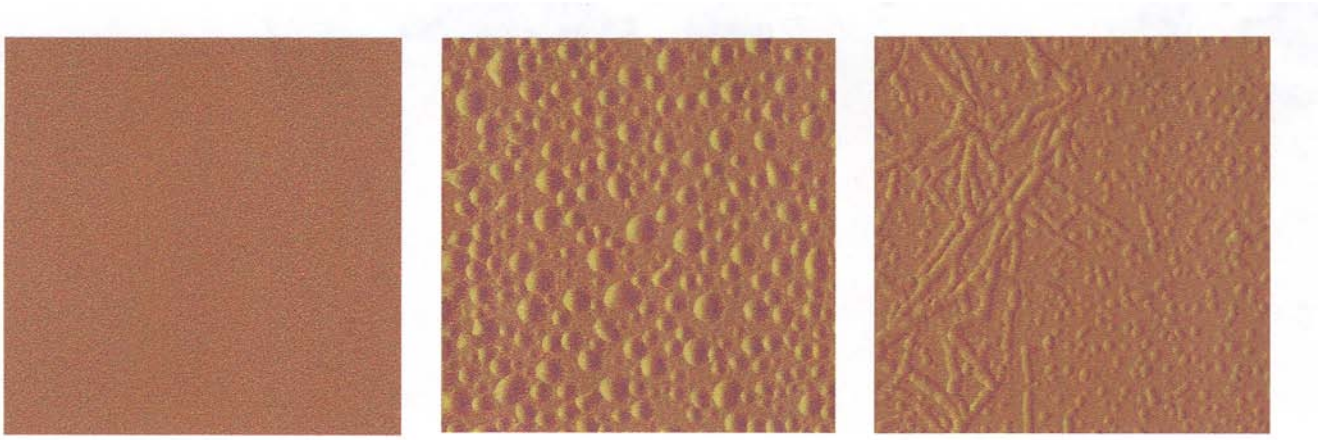

Each image is 5µm x 5µm.

Figure 1. AFM Images of SAM Coatings: (Left) As-fabricated dimethyldichlorosilane (DDMS) coating showing ideal monolayer structure. (Center) DDMS coating after two weeks at 50°C, 100%RH showing formation of spherical blisters. (Right) Octadecene coating after 50 days at 50°C, 80% RH showing formation of interconnected blisters.

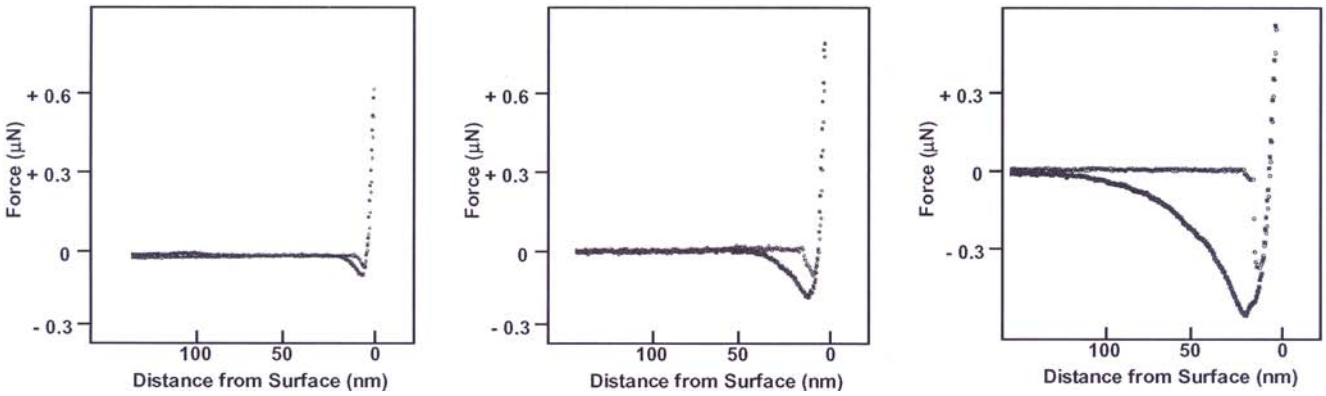

Figure 2. Interfacial force microscope (IFM) normal force vs. distance profiles for octadecene films as a function of exposure conditions. The IFM tip approaches the surface from the left (top trace in each figure) and is then retracted (bottom trace in each figure). Deflections in a negative direction represent attractive, adhesive interactions. The strong positive (repulsive) deflection at the right of each profile is due to mechanical deformations of the tip and substrate when the tip contacts the surface. (Left) Initial film prior to humidity testing. (Center) Film exposed for 50 days, T = 50°C, RH = 80%. (Right) Film exposed for 180 days, T = 80°C, RH = 100%.

Failure Mechanisms in Explosively Driven Power Supplies

by R. E. Setchell, J. D. Keck, S. T. Montgomery, M. U. Anderson, and D. E. Cox

Motivation—In explosively driven power supplies, voltages and currents are generated through shock-induced depoling of ferroelectric ceramic elements. The shock wave is generated by detonating an adjacent explosive charge, resulting in a diverging, attenuating wave structure propagating through the encapsulated volume containing the ceramic elements. Acceptance testing of the material used for high voltage generation (PZT 95/5) is limited by high-voltage breakdowns that occur late in time as the wave propagates through a test sample, particularly at cold temperatures. A fundamental understanding of this and other possible failure mechanisms could have a significant impact on material acceptance rates, design margins, and overall power supply reliability.

Accomplishment—Two developments were necessary in order to obtain new insights into power supply failure mechanisms. The first involved gas-gun techniques for generating diverging, attenuating wave structures similar to those generated by the detonation of a small explosive charge. A number of non-planar impactor designs at various impact velocities were examined in order to establish conditions that mimicked wave properties measured in actual power supplies. The second development was to divide the ground electrode of a poled PZT 95/5 bar into as many as five isolated segments along the bar length. During shock motion along the bar, currents flowing between each segment and ground are monitored independently using current-viewing resistors (CVRs). A resistive load is used to generate an appropriate electric field in the PZT 95/5 bar. A schematic of this experimental configuration is shown in Fig. 1, and typical currents recorded during an experiment are shown in Fig. 2. During shock propagation, the individual CVRs record the depoling current, the load-resistor current producing an electric field, and the charging currents on each segment reflecting their capacitance. In the experiment summarized in Fig. 2, a failure event occurs as the shock is passing from the fourth to the fifth segment. Current spikes indicate the onset of internal conduction in the first segment, which has experienced compression by the highest-strength shock followed by unloading to near-ambient pressures. A conduction "front" appears to be propagating into subsequent segments later in time. Figures 3 and 4 show the initial temperature dependence of other properties that can be obtained from these information-rich experiments.

Significance—These experiments are revealing previously unknown details of failure mechanisms-the "where" and "what," rather than just the "when." By combining these details with the results of extensive studies of PZT 95/5 properties under one-dimensional shock loading we have conducted in recent years, we are able to establish reasonable descriptions of failure processes. We now believe that the failure event shown in Fig. 2 results from PZT 95/5 material near the front of the bar being compressed well beyond its threshold for dynamic yielding, resulting in significant material damage, followed by a loss of dielectric strength during subsequent unloading due to the unsupported shock structure. Shock properties at cold temperatures exacerbate these processes. With such understanding, design parameters now can be critically examined with the goal of minimizing the probability of failures.

Sponsors for various phases of this work include: Nuclear Weapons/Advanced Design and Production Technologies (ADAPT)

Contact: Robert E. Setchell, Nanostructures & Advanced Materials Chemistry, Dept. 1122
Phone: (505) 844-3847, Fax: (505) 844-4045, E-mail: resetch@sandia.gov

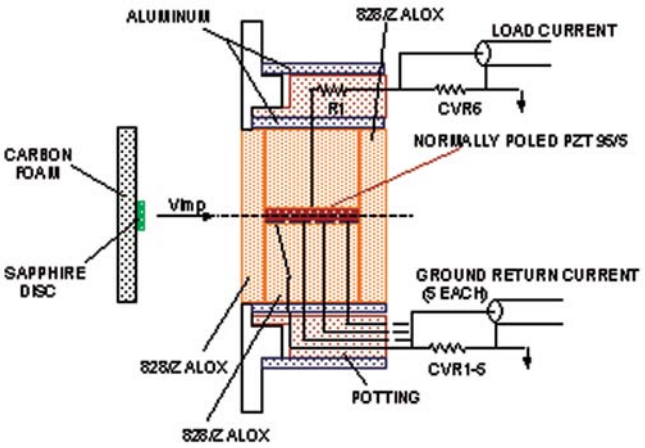

Figure 1. Configuration for "segmented bar" gas gun experiments. Non-planar impact results in a diverging, attenuating shock wave similar to that produced by an explosive charge.

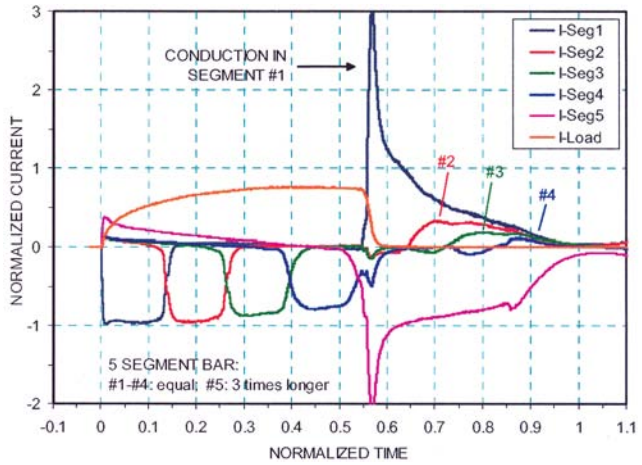

Figure 2. Currents recorded during an experiment at room temperature. The shock wave is entering the last segment when a conductive failure occurs in the first segment.

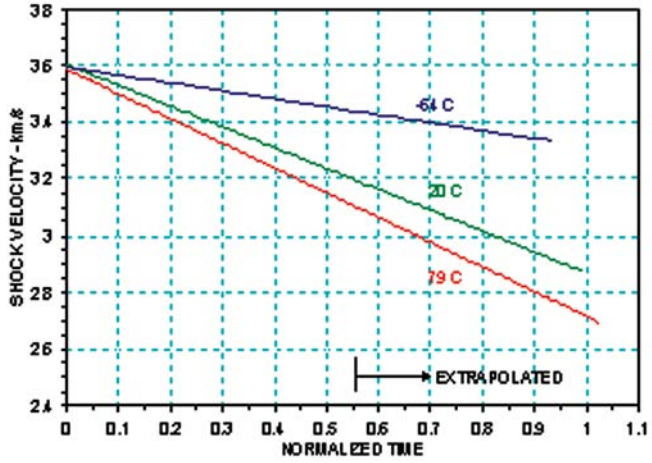

Figure 3. Shock velocity within the PZT 95/5 bars for different initial temperatures. Velocity values are determined from a distance-time fit based on the individual segment currents.

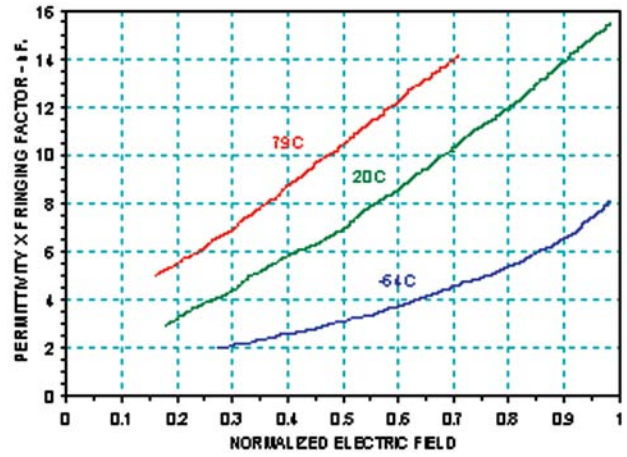

Figure 4. Dielectric properties of the final bar segment prior to shock wave arrival. The trend with initial temperature is consistent with the trend in small-signal measurements of dielectric constant.

Single Event Upsets (SEUs) in Silicon-On-Insulator (SOI) Technology

by G.Vizkelethy, P. E. Dodd, J. R. Schwank, M. R. Shaneyfelt, D. S. Walsh, and B. L. Doyle

Motivation—Silicon-On-Insulator (SOI) technology was thought to be less prone than bulk circuits to Single Event Upsets (SEUs) due to heavy ion hits because of its design. It was believed that the charge deposited in the buried oxide (BOX) and the substrate would not contribute to the charge collection process. Therefore, the SEU cross-sections were expected to be on the order of the gate areas. Recent measurements on Sandia National Laboratories (SNL) SOI SRAMs with thin BOX showed that these cross sections are closer to the sum of the gate and drain areas, which indicated higher than ex-pected charge collection in these circuits. We have performed charge collection and SEU experiments using the SNL nuclear microprobe on actual SRAMs and model circuits to investigate this anomalously high charge collection.

Accomplishment—SOI circuits were considered more radiation hard because the sensitive volume was thought to be much smaller than in bulk circuits. Although there were some experiments several years ago that indicated significant charge collection in MOS structures, they were overlooked because previous SOI circuits had not shown anomalously high SEU rates. That was due to the thick BOX that was several thousands of nanometers. Newer technologies required much thinner BOX layers, on the order of a few hundred nm. After discovering the anomalously high charge collection, it was thought to be due to the formation of a con-ducting "pipe" in the oxide during and shortly after the ion hit. We carried out charge collec-tion experiments on MOS capacitor structures to model the SOI circuits. We found that the charge collection has a very strong dependence on the applied bias. The charge collection was significant at negative biases and practically zero for positive biases for n-type substrates. The opposite was observed for p-type substrates. This result showed immediately that the conduc-tive pipe model was incorrect. Figure 1 shows the charge collection dependence on the applied bias for both n and p-type substrates. The same experiment carried out on p+ and n+ substrates resulted in much lower charge collection. The amount of collected charge decreased with increasing oxide thickness. Based on the above observation we could qualitatively explain the charge collection, which was later proven quantitatively by 3D device codes. When the MOS capacitor is in depletion or inversion mode (negative bias for the n-type and positive bias for the p-type substrate) there is a significant electric field at the oxide-substrate interface. This field increases with decreasing oxide thick-ness. According to the Gunn theorem when the charge generated by the ion hit moves through this field, it will induce charge on the electrodes of the device. The charge collection at zero bias in the case of p-type substrates is probably due to trapped process charge. These results led to a mitigation technique to reduce the charge collection from the substrate below the oxide. Figure 2 shows the charge collection map for SNL SRAMs with and without applying bias to the substrate.

Significance—SOI is a very promising technology to produce radiation hard circuits. It is important to understand the charge collection in these devices. Our experiments showed that, in contrast to the earlier beliefs, these devices have significant charge collection when the BOX layer is thin. The explanation of the model ex-periment helped find a mitigation technique.

Sponsors for various phases of this work include: Nuclear Weapons/Science & Technology, and Defense Threat Reduction Agency (DTRA)
Contact: Gyorgy Vizkelethy, Radiation-Solid Interactions, Dept. 1111
Phone: (505) 284-3120, Fax: (505) 844-7775, E-mail: gvizkel@sandia.gov

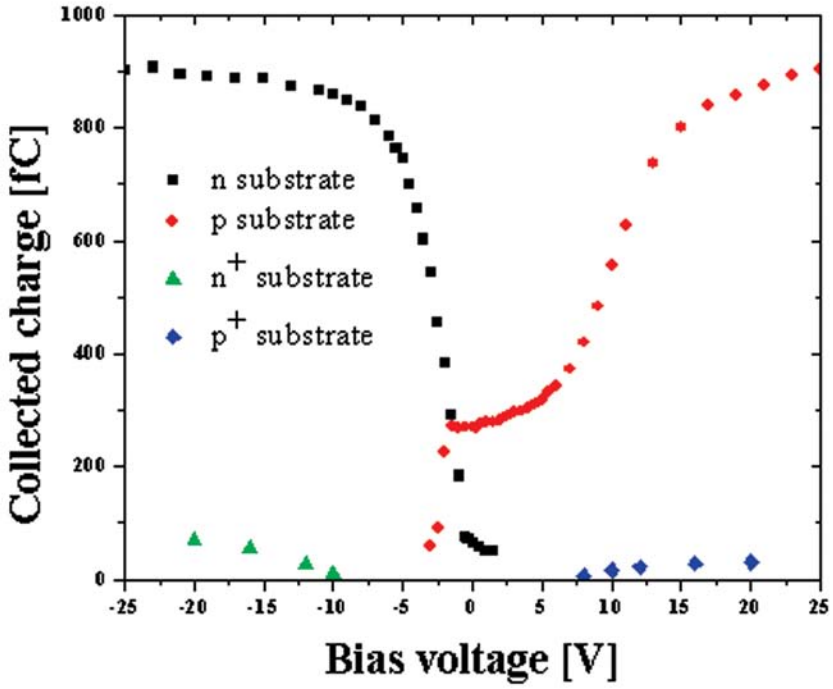

Figure 1. Charge collection as a function of applied bias for MOS capacitors on different substrates.

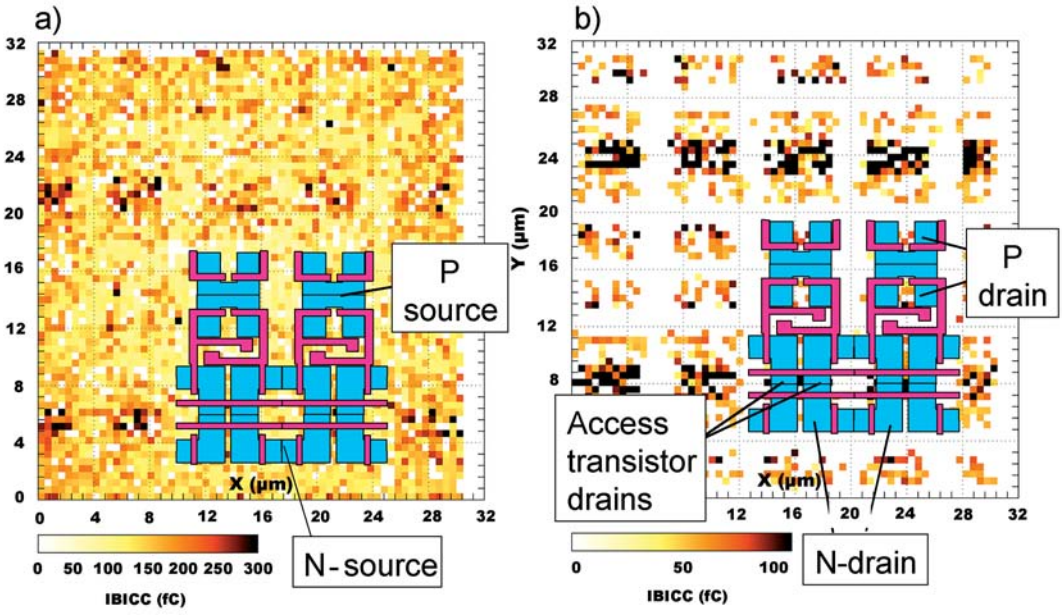

Figure 2. Charge collection maps of SNL SRAMs (n-type substrate) with different biases applied to the sub-strate. The applied negative bias significantly suppresses the charge collection.

Ion-Induced Emission Microscopy (IIEM)

by P. Rossi, B. L. Doyle, D. S. Walsh, G. Vizkelethy, F. D. McDaniel

Motivation—A radically new form of nuclear microscopy, the IIEM, was invented by Sandia a few years ago as an alternate way to perform localized single-ion nuclear analysis, whenever ion beams are difficult to focus or when cost issues are important. The specific challenge Sandia was facing was the measurement of single event effects (SEE) on integrated circuits using high Linear Energy Transfer beams from the Sandia Tandem-Radio Frequency Quadrupole (RFQ) accelerator, operational since spring 2002. These beams have high magnetic rigidity and poor chromaticity, which make the traditional high spatial resolution micro-focusing impossible. The emission microscopy consists of: 1) irradiating the sample with a very low intensity broad ion beam; 2) measuring the impact position of the single ion by exploiting the emission of particles (electrons, ions or photons) from the surface, and 3) relating this position to the effect this ion produces on the sample.

Accomplishment—Our Department already developed prototypes of two types of IIEM, i.e. the IEEM (Ion Electron EM, in Fig. 1), based on emitted electrons and IPEM (Ion Photon EM), based on emitted light. Recent work on the IEEM was aimed at curing some weaknesses in its operation, like the reduced ion flux reaching the sample and the low electron emission yield from a non-metallic surface. Our RFQ, boosting the ion tandem energy, allows us to have one of the most ionizing radiations in the universe (Gold at 374 MeV) with a relatively simple and cheap device. A drawback is the flux limitation due to the highly reduced duty-cycle-fraction of machines of this kind (1/500). We have carried out modifications in the beam line which have dramatically raised the flux. New diagnostics and new control software have boosted the effectiveness and ease of operation, allowing easy SEE measurements.

As for the emitted electron yield, a study of coating materials has been carried out in collaboration with the Italian INFN-SIRAD group, indicating boron-doped diamond to be an outstanding "covering" material, with a yield higher than metals.

IPEM detects the light coming from a phosphor blade or coating superimposed to the sample, to measure the ion impact position with an optical microscope. The ions can come from either an accelerator or a radioactive alpha source ("Table-top" IPEM, in Fig. 2). We have already realized an "accelerator" IPEM, while we have not yet obtained an alpha source of adequate specific activity. An issue is the low spatial resolution, due to the "blooming" of light inside the phosphor. To solve this, we are developing a kind of "black matrix" with proton lithography techniques (collaboration with Singapore University): tiny wires of a micrometric mesh would delimit phosphor pads and contain the light produced in them.

Significance—We have worked to boost IEEM and IPEM to let them become an "every day" laboratory tool. IEEM is now currently used to assess SEE. IPEM promises to find application both for SEE and cellular radiobiological research. This latter should benefit from the IPEM's in-air irradiation capability.

Sponsors for various phases of this work include: Nuclear Weapons/Science & Technology
Contact: Paolo Rossi, Radiation Solid Interactions and Processing, Dept. 1111
Phone (505)844-7302; Fax (505) 844-7775; E-mail: prossi@sandia.gov

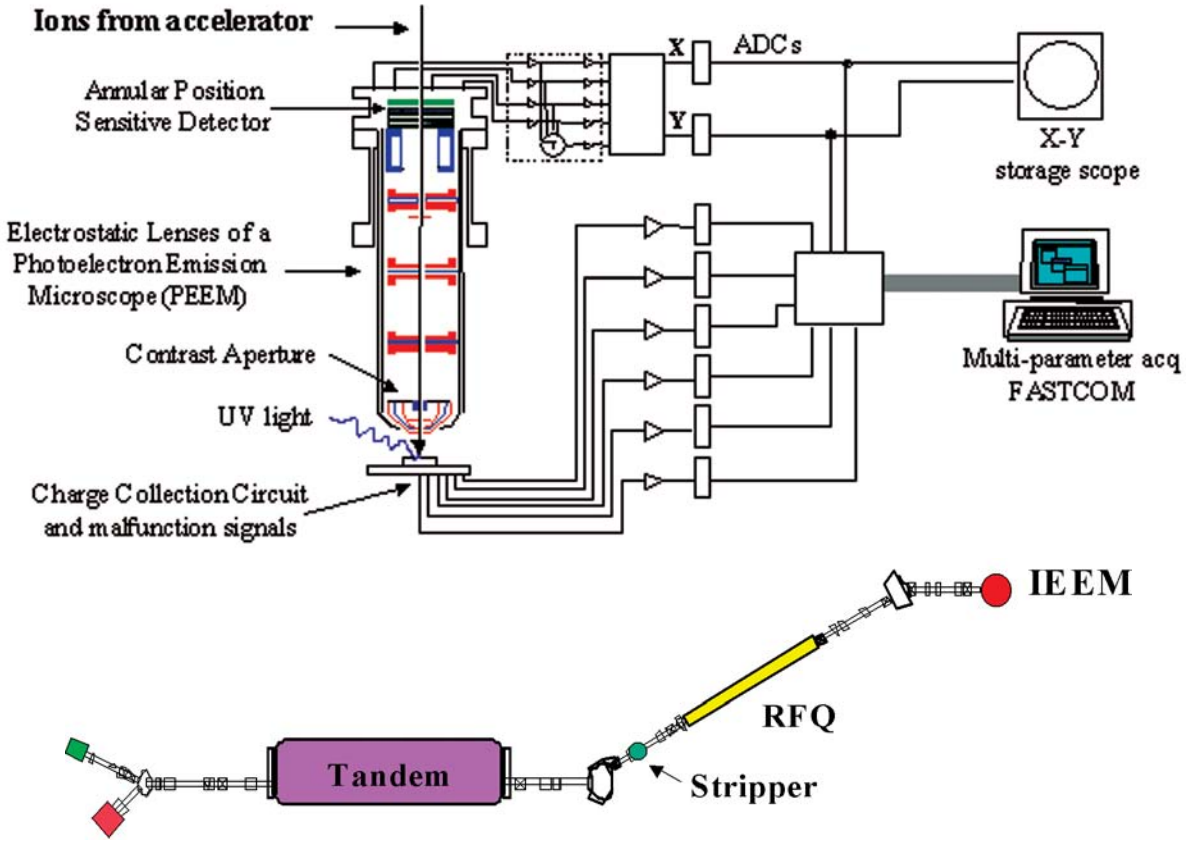

Figure 1. SSNL-IEEM schematics (top) and the Tandem-RFQ beam line (bottom).

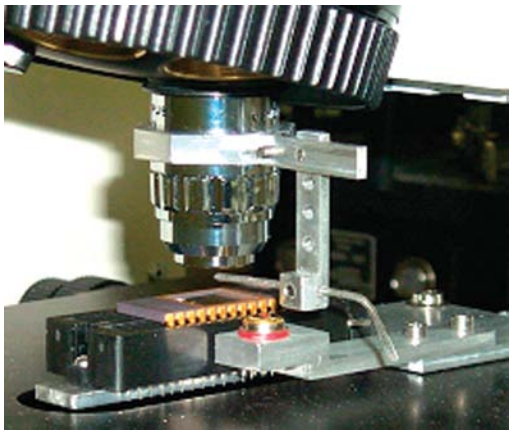

Enlargement shows the position of the lens, the alpha source support (a needle represented by an Allen wrench) and a microchip as a sample. The 1mm size source should be placed at the top of the needle.

Figure 2. Prototype of alpha particle table IPEM, with the "Mepsicron" position sensitive detector (PSD) on top of the microscope.

Wide Bandgap Compound Semiconductor Science

Gallium Nitride Crystal Growth Kinetics from Selective-Area Growth Experiments and 3-D Morphology Evolution Model

by M. E. Coltrin and C. C. Mitchell, Sandia National Laboratories, and D. Du and D. Srolovitz, Princeton University

Motivation—Crystals that grow in nature usually have convex features that form as the crystal grows outward. The fastest growing faces grow to extinction, and the crystal is then bounded by the slowest growing faces. The Wulff construction is a polar plot of the facet-orientation-dependent growth rate. At long time the shape of a grown crystal will match the Wulff shape. For growth of *concave* features, the rules change. The fastest growing faces actually grow to dominance, rather than disappear. We have developed a new approach to measure the intrinsic growth rates of the fast-growing crystal faces in GaN using special patterning in an Epitaxial Lateral Overgrowth (ELO) mask. Concave growth templates are created lithographically to force the "inward" growth geometry The Princeton group (Du and Srolovitz) are developing a 3-D crystal facet evolution model to extract the intrinsic GaN crystal growth kinetics of orientations "missing" from the Wulff shape.

Accomplishment—A representative plan-view scanning electron micrograph (SEM) image is shown in Fig. 1(a). The shape of the original exposed growth zone is shown as the blue hexagonal feature in Fig. 1(b), and as the yellow outline in the each of the images. The unexposed interior and outer regions are covered with a dielectric mask. GaN ELO occurs selectively only on the exposed feature, growing both laterally over the mask and vertically. Shown in Figs. 1(c)-(f) are model simulations of the growth as time proceeds. The and equivalent facets, red faces in the figure, are $(11\bar{2}2)$ aligned parallel to the edges of the hexagonal pattern, and are the fastest growing of the three major faces illustrated. As the ELO feature grows outward from the pattern, the faces grow to extinction. The slowest growing faces, $(11\bar{2}2)$ colored brown in the figure and $(1\bar{1}01)$ aligned 30° from the faces, become larger and bound $(11\bar{2}2)$ the *outside* perimeter at long time. This illustrates the expected behavior for growth of convex features, as seen in the SEM image and calculation, Figs. 1(a) and 1(f). The feature also grows rapidly in the vertical direction, causing the exposed basal plane (0001) to shrink with time. Figure 1(a) shows that inside the feature, i.e., for concave growth, the fast-growing faces are dominant, exactly $(11\bar{2}2)$ opposite of the situation outside the feature. It is evident that the model captures the qualitative aspects of the crystal evolution at the convex and concave corners. However, the center portion of the structure has filled before the outside portion has grown to a hexagon, indicating that the facet rate constants in the simulation are not in the correct ratio.

Significance—Sandia has developed a related GaN defect-reduction technique called Cantilever Epitaxy (CE). We have shown that vertical threading dislocations can be reduced by proscribed variation of the crystal facet morphology during growth. A fundamental understanding of GaN crystal growth kinetics, and especially how it varies with temperature, provides quantitative guidance to control and manipulate the crystal morphology during CE growth and coalescence. Understanding the crystal coalescence in the interior of such features will also give us insight into the coalescence of polycrystalline GaN during the growth and ripening of the initial nucleation layer during heteroepitaxy.

Sponsors for various phases of this work include: DOE Office of Basic Energy Sciences
Contact: Michael E. Coltrin, Chemical Processing Sciences, Dept. 1126
Phone: (505) 844-7843, Fax: (505) 844-3211, E-mail: mecoltr@sandia.gov

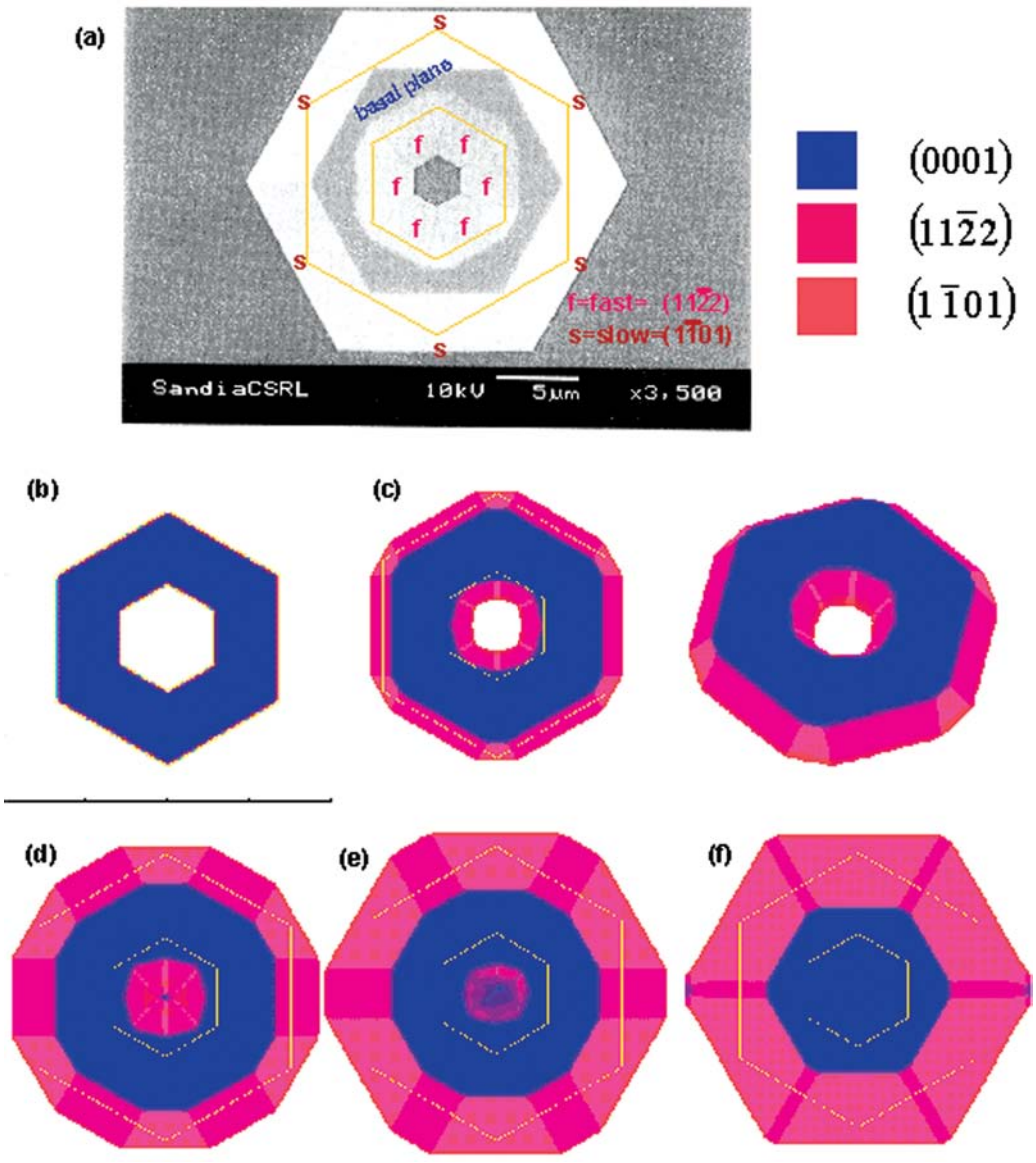

Figure 1. (a) Scanning electron micrograph (SEM) image of a GaN ELO feature grown from a hexagonal annular pattern. Fast-growing $(11\bar{2}2)$ facets are labeled with "f," slower-growing $(1\bar{1}01)$ faces are labeled with "s," and the (0001) basal plane appears as grey, in the plane of the image. The original exposed pattern is shown in blue in part (b). The calculated feature shape at early time is shown in plan view and perspective in part (c). Identification of the crystal facets by color is given at the top right portion of the page. Parts (d) through (f) show how the ELO feature shape evolves as growth proceeds. The simulation clearly shows the fast-growing $(11\bar{2}2)$ faces growing to extinction at the convex corners, i.e., the outer boundaries of the crystal.

Understanding Gallium Nitride Nucleation Layer Evolution

by D. D. Koleske, M. E. Coltrin, K. C. Cross, C. C. Mitchell, and A. A. Allerman

Motivation—The use of GaN nucleation layers (NLs) promotes 2D growth on sapphire and reduces dislocation density in the final GaN film. However, dislocations in GaN grown on sapphire have been observed to originate in the NL, making the study of how they evolve imperative for further dislocation reduction. While low temperature (T) GaN NLs are commonly used to improve GaN growth on sapphire, there is little understanding how the NLs evolve during the ramp to high T and how they influence the high T GaN growth.

Accomplishment—For this study, GaN NLs were grown at 550 °C to a thickness of 30 nm using metalorganic chemical vapor deposition (MOCVD). Once grown, the NLs were heated under hydrogen and ammonia up to 1050 °C and held at 1050 °C before high T GaN growth proceeds. In Fig. 1, atomic force microscope (AFM) images of the GaN NL morphology during the annealing procedure are shown. As shown in Fig. 1, the GaN NL changes from a smooth (1 nm roughness) film to a rough film with nuclei approaching 1 μm in width and 200 nm in height. The nuclei that form on the NL are the initial GaN grains that continue to grow when the Ga source is turned back on. With further annealing of the NL at constant T, the GaN nuclei become smaller in size.

To quantify the GaN NL evolution the AFM images from Fig. 1 and the optical reflectance waveform shown in Fig. 2 were analyzed. Detailed analysis of the reflectance waveform showed that the reflectance signal could be used to extract the GaN NL thickness during the ramp to high T. Since the NL was losing thickness during this ramp and not substantially roughening until T > 1000 °C, the NL decomposition rates were obtained using the reflectance signal. From this work it was determined that the GaN NL decomposed with an activation energy of 2.7 eV, consistent with a rate limiting step of Ga desorption. Analytic fits were developed to fit the initial curvature in reflectance waveform, i.e. points (a-e) in Fig. 2. During decomposition, the desorbed Ga atoms were reincorporated into the growing GaN nuclei as shown in Fig. 1(e-i), reaching a maximum height in Fig. 1(i). Further annealing led to full decomposition of all of the original NL. At this point the GaN nuclei began to decompose and decreased in size as shown in Fig. 1(j-l).

Calculation of the height-height correlation function from the AFM images yielded information on the smoothing process during the NL annealing. It was found that the GaN nuclei shown in Fig. 1(e-j) had a smoothing exponent ($n = 2.3 \pm 0.3$) consistent with an evaporation and recondensation mechanism, while the films in Fig. (a-d, k, l) had a smoothing exponent ($n = 3.7 \pm 0.1$) consistent with a surface diffusion mechanism. The observation of an evaporation and recondensation smoothing mechanism for the growth of the GaN nuclei is entirely consistent with the NL decomposition kinetics mentioned above.

Significance—Heteroepitaxial growth of new materials will become increasingly important because single crystal substrates for these new materials rarely exist. Developing a more complete understanding of hetero-nucleation will aid in quick testing and evaluation of these new material systems. Using GaN as a test case, a clearer physical understanding of the GaN nuclei formation from the NL has been achieved.

Sponsors for various phases of this work include: DOE Office of Basic Energy Sciences, Grand Challenge Laboratory Directed Research & Development

Contact: Daniel D. Koleske, Chemical Processing Sciences, Dept. 1126
Phone: (505) 284-4531, Fax: (505) 844-3211, E-mail: ddkoles@sandia.gov

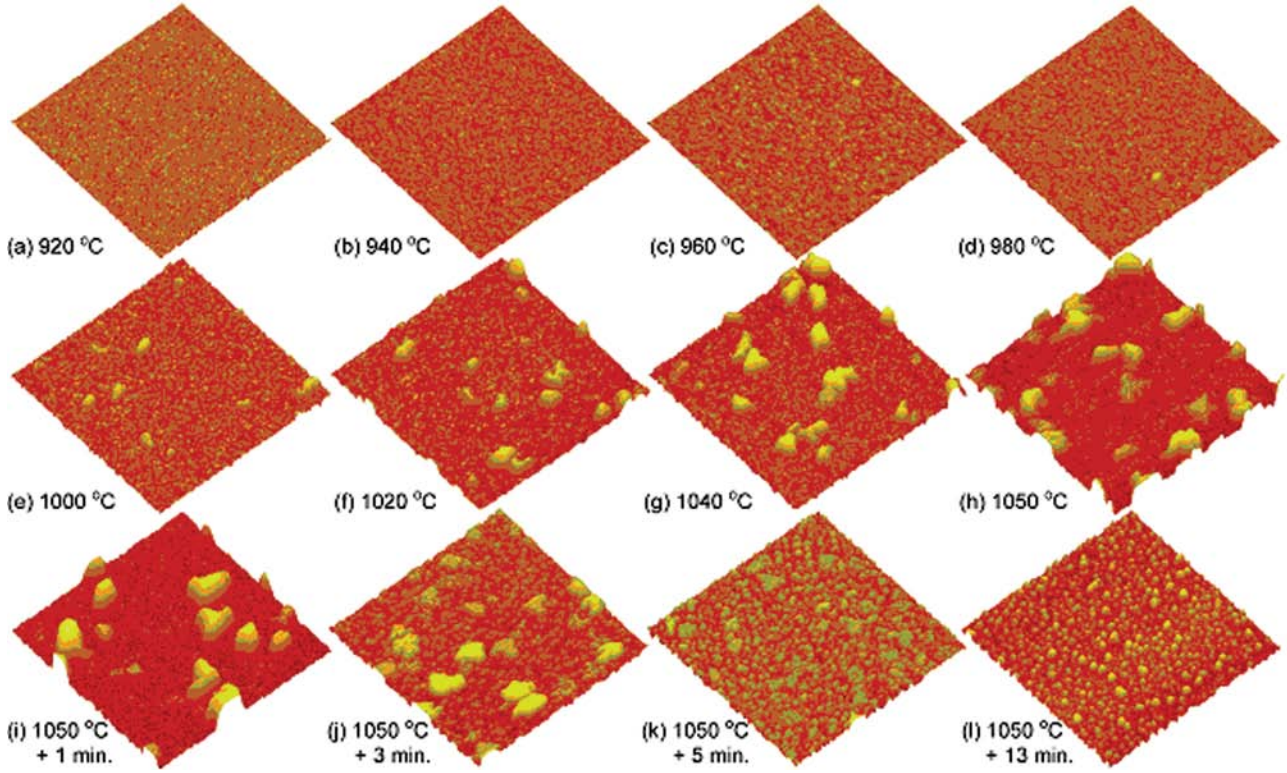

Figure 1. Atomic force microscopy (AFM) images of the GaN nucleation layer morphology for different annealing temperatures and times. The height scale is 200 nm and the scan size is 3 x 3 μm. GaN nuclei reach their maximum size at (i) after ramping to 1050 °C and holding for 1 minute.

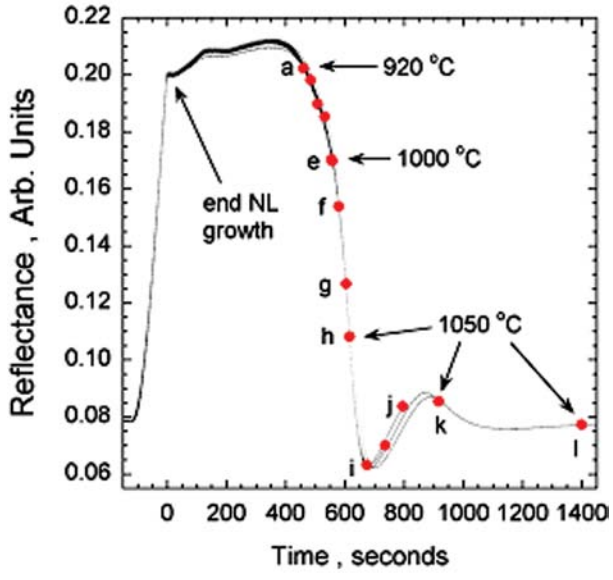

Figure 2. Optical reflectance waveform measured during the anneal to high temper-ature. The letters (a) - (l) denote the stopping point during the anneal and correspond to the AFM images shown in Fig. 1.

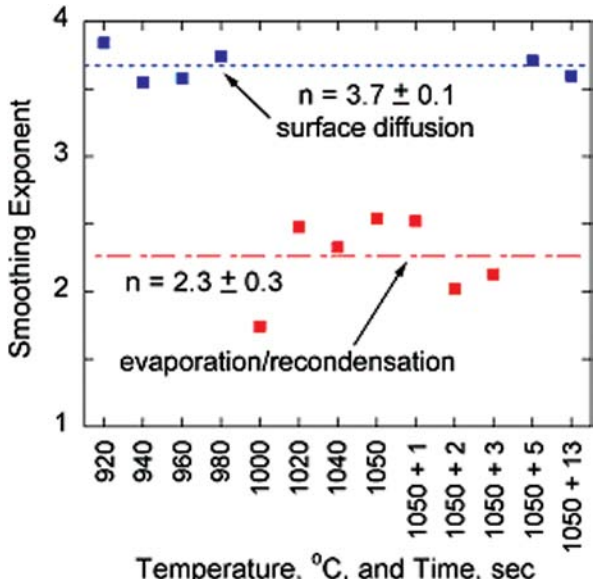

Figure 3. Measured exponents used to determine the smoothing mechanism from the AFM images in Fig. 1. An evaporation and recondensation mechanism accounts for the growth of the GaN nuclei shown in Fig. 1.

Cantilever Epitaxy: Multi-Step Optimization of Growth and Substrate Processing

by C. C. Mitchell, D. D. Koleske, D. M. Follstaedt, K. C. Cross, K. H. A. Bogart, N. A. Missert, A. A. Allerman, P. P. Provencio, M. E. Coltrin

Motivation—For GaN grown on any readily available substrate the large lattice mismatch between GaN and the substrate results in 10^8 — 10^{10} threading dislocations per cm^2. For light emitting devices, these dislocations act as non-radiative centers and ultimately limit device performance. To reduce the GaN dislocation density on lattice mismatched substrates, a unique growth technique, called cantilever epitaxy (CE) has been developed and improved upon at Sandia. This is particularly important for the fabrication of vertical cavity surface emitting lasers (VCSELs) and light emitting diodes (LEDs) below 400 nm.

Accomplishment—Our prior research on CE focused on establishing growth conditions to turn dislocations that originate from the growth zone on top of the post. Once turned these dislocations no longer interfere with device layers that are grown on top. The dislocation turning was accomplished by choosing growth conditions that form a pyramidal gable bounded by $(11\bar{2}2)$ facets on top of the post. After forming the pyramidal gable, the lateral growth rate is increased, causing the dislocations to turn and run parallel to the growth plane. Using this method for dislocation turning, the dislocation density was reduced for GaN CE films by 2-3 orders of magnitude.

Cathodoluminescence (CL) images showed an additional array of dislocations formed during coalescence of the cantilever wings, referred to as dark-block defects. The dark-block regions are observed as discontinuities in optical microscopy and scanning electron microscopy (SEM). Transmission electron microscopy (TEM) showed that the discontinuities are cracks where two misoriented cantilevers joined. Figure 1 shows a scanning CL and SEM image of these defects.

To eliminate the dark-block defects three aspects of CE growth were closely investigated. These steps included the nucleation layer (NL) and gable growth, the lateral growth over the trench, and the morphology of the cantilevers prior to coalescence. The density of the NL affects the quality of the gable, illustrated in Fig. 2. A uniform gable is formed when the NL is dense and uniform. The differences between these two gables can be monitored using optical reflectance. Once the gable is formed, the growth conditions are changed to enhance the lateral overgrowth. The cantilevers must grow laterally and span the trench before the trench fills in. Improvements in the sapphire etching and mask uniformity have aided in the fabrication of sapphire cantilever substrates with deeper trenches, allowing for more latitude in the growth conditions. Prior to coalescence the growth conditions $(11\bar{2}2)$ are again changed to form facets. These facets are then allowed to coalesce and the cantilevers meet smoothly. When these growth criteria are successfully accomplished, GaN CE wafers can be grown with dislocation densities of $5x10^7$ cm^{-2} as shown by CL in Fig. 3.

Significance—Careful optimization of the CE process has led to the elimination of the detrimental dark block defects while producing films with fewer threading dislocations. The fundamental study of how and why GaN crystals coalesce, whether for CE or for planar films, yields valuable information that will lead to the optimization of GaN heteroepitaxy. These films are currently being tested for UV LEDs; preliminary results indicate a significant improvement for wavelengths < 380 nm.

Sponsors for various phases of this work include: Grand Challenge Laboratory Directed Research & Development, DOE Office of Basic Energy Sciences, and DOE Office of Building Technology
Contact: Christine C. Mitchell, Chemical Processing Sciences, Dept. 1126
Phone: (505) 845-3550, Fax: (505) 844-3211, E-mail: ccmitch@sandia.gov

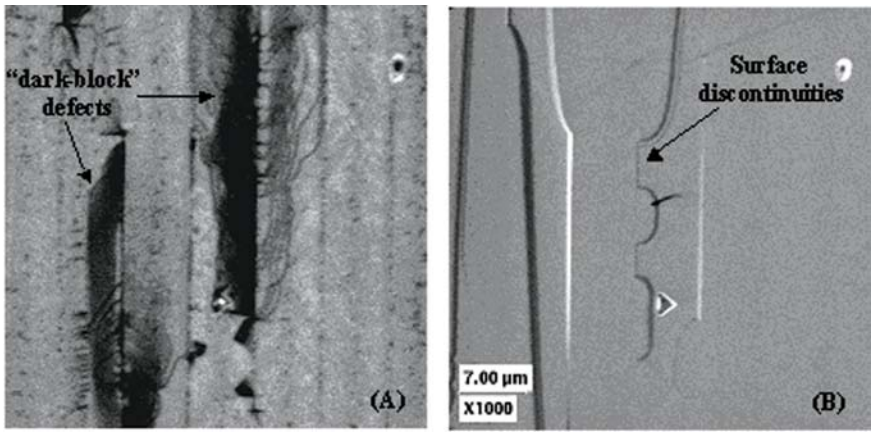

Figure 1. (A) Scanning panchromatic CL and (B) secondary electron (SE) micrographs of a coalesced cantilever substrate where surface discontinuities are present. The surface discontinuities seen in the SE images directly correlate with the "dark-block" defects seen in the cathodoluminescence scan.

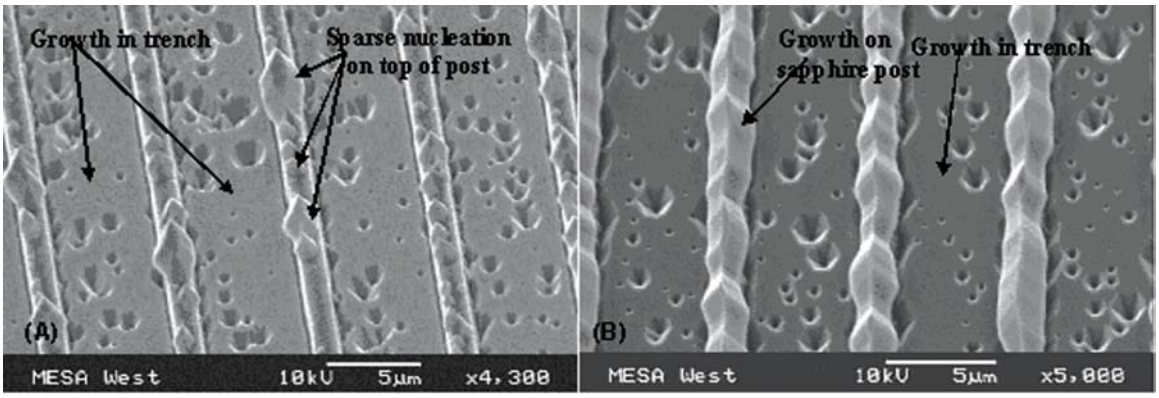

Figure 2. SEM images of (A) a nucleation layer condition that resulted in non-uniform gable formation and (B) a nucleation layer condition where the subsequent gable growth is uniform along the length of the post.

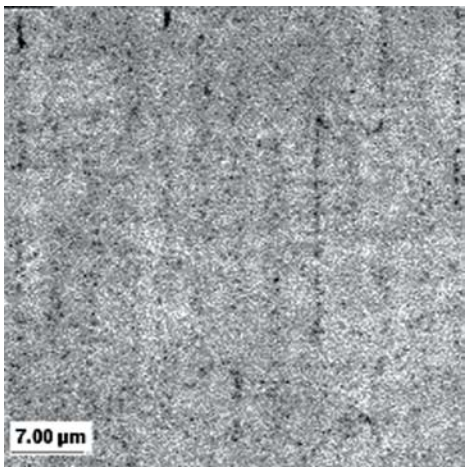

Figure 2. Scanning cathodoluminescence scan of coalesced cantilever epitaxy film without dark-block defects. Overall dislocation density is 5 x 10^7 dislocations/cm^2.

X-ray Diffraction Analysis of Threading Dislocations in GaN Thin Films

by S. R. Lee, A. M. West, A. A. Allerman, K. E. Waldrip, D. M. Follstaedt, and C. R. Abernathy

Motivation—In recent years, GaN has emerged as an attractive new material for optoelectronic and electronic device applications. The wide bandgap of GaN and its alloys enables light-emitting devices with wavelengths spanning the green, blue, violet, and ultra-violet (UV) regimes. Potential applications for these light emitters include efficient solid-state lighting for buildings and UV-based detection of biological agents. The high breakdown field and high mobility of GaN also enables high-speed, high-power transistors operating at frequencies near 10 GHz. These transistors are suitable for making lightweight, compact power-supplies for phased-array synthetic aperture radars. All of these applications use GaN thin films grown on sapphire or SiC substrates. Since heteroepitaxy of GaN on these lattice-mismatched substrates remains challenging, these films contain numerous threading-dislocation defects that limit device performance and lifetime. Thus, convenient methods for accurately measuring the threading-dislocation density are needed to support ongoing work to improve the GaN film quality and to assess the impact of dislocations on device performance.

Accomplishment—We have developed an improved x-ray diffraction (XRD) method for measuring the threading-dislocation density in GaN thin films. The method rests on the fact that the strain fields produced by dislocations cause both inhomogeneous tilting and twisting of the GaN crystal planes and localized incoherence of the crystal lattice. As shown in Fig. 1, these real-space distortions lead to corresponding broadening of the reciprocal-lattice points of the crystal. XRD systematically probes this broadening by measuring the characteristic width of selected Bragg-diffraction peaks. The (*hkl*) dependence of the peak-width broadening is interpreted using a reciprocal-space model that convolves the tilt variance, the twist variance, and the coherence length of the dislocated film. Fitting of the model to experiment uniquely deconvolves the tilt, twist, and coherence-length contributions. The threading-dislocation density then follows using previously developed dislocation theory that relates the deconvolved lattice rotations to the dislocation density. The resultant threading-dislocation density has been benchmarked against transmission electron microscopy (TEM); good agreement is found. Recently, the validated XRD technique was used to measure the threading-dislocation density in high-electron-mobility transistors (HEMTs) with room-temperature mobilities ranging from 231 to 1830 cm^2/V-s. In Fig. 2, we compare the HEMT mobility to the measured dislocation density and find that mobility tends to decrease as dislocation density increases. Importantly, high mobility (> 1800 cm^2/V-s) occurs at low threading-dislocation density (< $1x10^9$ cm^{-2}).

Significance—The XRD method for measuring dislocations has several key advantages. First, unlike TEM, no destructive and time-consuming sample preparation is required. Second, a large sample area is probed; this eliminates point-sampling errors inherent to all microscopy-based methods. Finally, unlike most methods, both low (~$1x10^8$ cm^{-2}) and high (~$1x10^{11}$ cm^{-2}) dislocation-density samples are probed with nearly equal ease. Because of these advantages, XRD measurements of threading-dislocation density are increasingly used to support the development of GaN-related materials and devices at Sandia.

Sponsors for various phases of this work include: Nuclear Weapons/Science & Technology, Grand Challenge Laboratory Directed Research & Development, and Defense Advanced Research Projects Agency
Contact: Stephen R. Lee, Semiconductor Material and Device Sciences, Dept. 1123
Phone: (505) 844-7307, Fax: (505) 844-3211, E-mail: srlee@sandia.gov

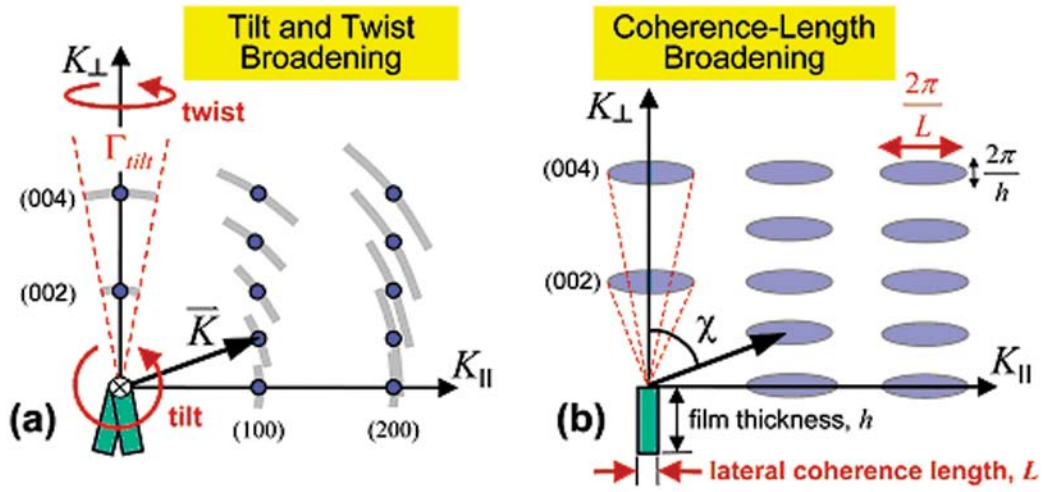

Figure 1. (a) Variations in the tilt and twist orientation of local domains in the GaN epilayer (*green rectangles*) cause purely transverse broadening of the reciprocal lattice (*blue dots*). (b) The finite size of the domains causes additional non-transverse broadening of the reciprocal lattice (*blue ellipses*). (c) Convolution of the broadening contributions due to tilt, twist, and coherence length yields the total peak width, Γ_{hkl}, at each reciprocal-lattice point.

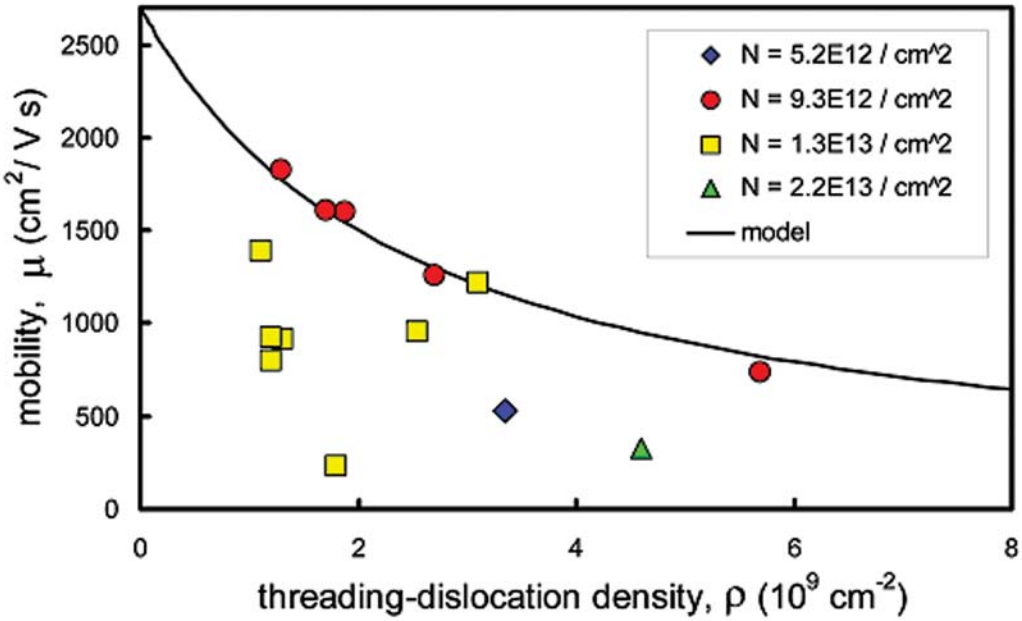

Figure 2. Room-temperature 2-D electron-gas mobility versus threading-dislocation density for GaN-based HEMTs. In the legend, **N** is the sheet-carrier density of the 2-D gas. The model has the form $1/\mu = 1/\mu_p + 1/\mu_d$, where $\mu_p = 2700$ cm^2/Vs is the optical-phonon contribution, $\mu_d = C/\rho$ is a dislocation-related scattering contribution, and C is a fitting parameter. Downward deviations from the model may be due to additional scattering produced by roughness at the AlGaN/GaN interface.

Optical Measurements and Theory Test AlGaN/GaN High Electron Mobility Transistor (HEMT) Models

by Steven R. Kurtz

Motivation—GaN-based electronics offer radical miniaturization of microwave power amplifier and radar circuitry. GaN's large bandgap, high breakdown field, high electron velocity, and excellent thermal properties have led to high electron mobility transistors (HEMTs) with up to ten times the power density of GaAs and other traditional semiconductors at frequencies up to 20 GHz.

Further contributing to the outstanding performance of GaN-based amplifiers is the highly conducting, 2-dimensional electron gas (2DEG) used for the HEMT channel. Intrinsic polarization and piezoelectric properties of GaN materials can produce a 2DEG at an AlGaN/GaN interface with a sheet carrier concentration of $10^{13}/cm^2$, well in excess of that achievable in any other III-V material system. The physics and material science of the AlGaN/GaN 2DEG are critical to the performance and future development of GaN-based electronics.

Accomplishment—To further reduce dislocation densities, we are evaluating alternative substrates to sapphire. Focusing on the properties of AlGaN/GaN devices grown on SiC substrates, we found that overall material quality and transport properties of the 2DEG were much improved over structures grown on sapphire. Hall mobility versus electron density measurements revealed that 2DEG mobility was limited by scattering in the AlGaN barrier, not dislocations, in devices grown on SiC.

Electronic properties of AlGaN/GaN heterostructures and HEMTs on SiC were determined using a contacted electroreflectance technique. This optical probe augments conventional electrical characterization of GaN-based field-effect transistors. By studying variations in the electroreflectance with applied electric field, spectral features associated with the AlGaN barrier, the 2DEG at the interface, and bulk GaN are clearly identified. The 2DEG produced a broad, first-derivative-like electroreflectance feature. Changing bias voltage, the 2DEG electroreflectance narrowed and converged with the GaN band-edge. A first-principle, Golden Rule calculation of the dielectric function was developed which described the variation of 2DEG electroreflectance with voltage (see Fig. 1). The AlGaN barrier displayed Franz-Keldysh oscillations (FKO), and the period of the FKO varied with bias voltage. Airy function lineshape fits provided accurate determinations of AlGaN barrier composition and polarization electric field. Comparing measured AlGaN electric fields with values predicted by a standard model of the AlGaN/GaN heterostructure conduction band, we found < 10% discrepancy between the measured polarization field and that predicted by a standard model for devices grown on SiC (see Fig. 2). However, AlGaN electric field measurements for devices grown on sapphire produced anomalous results, indicating the presence of trapped space charge.

Significance—An optical probe of AlGaN/GaN heterostructures and transistors augments conventional electrical characterization tools. The electroreflectance technique and supporting calculations provide the first optical measurements of AlGaN barrier electric field and composition and 2DEG Fermi energy and electron density. This new information allows us to test and refine basic models of AlGaN/GaN heterostructures and transistors.

Sponsors for various phases of this work include: DOE Office of Basic Energy Sciences, Laboratory Directed Research & Development, and Cooperative Research & Development Agreement
Contact: Steven R. Kurtz, Semiconductor Physics, Dept. 1123
Phone: (505) 844-9637, Fax: (505) 844-3211, E-mail: srkurtz@sandia.gov

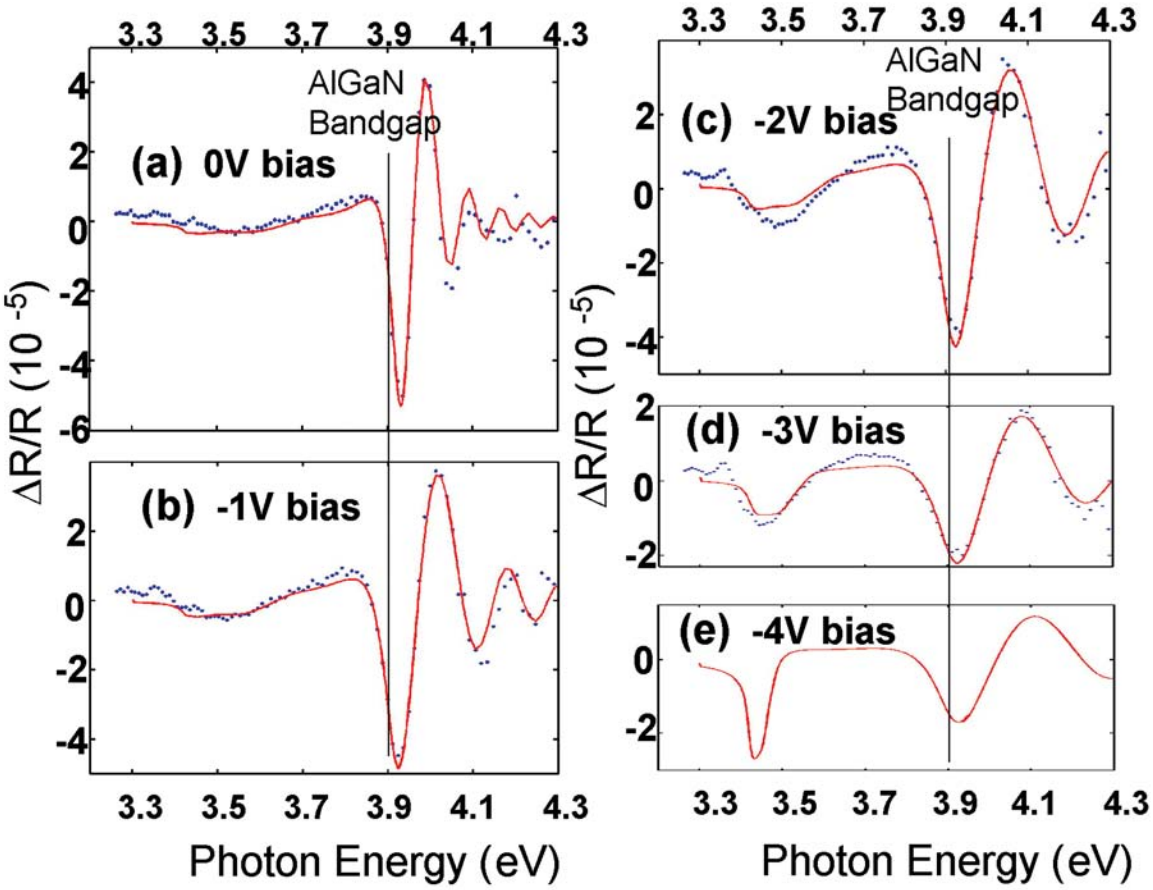

Figure 1. Electroreflectance spectra (300 K) for the $Al_{0.19}Ga_{0.81}N$ (320Å)/GaN heterostructure at 0V (a), –1V (b), –2V (c), and –3V (d) gate bias. (same scale) Solid lines are the AlGaN FKO lineshape fit plus the contribution from the 2DEG dielectric model. Based on the models, the –4Vspectrum (e) was simulated.

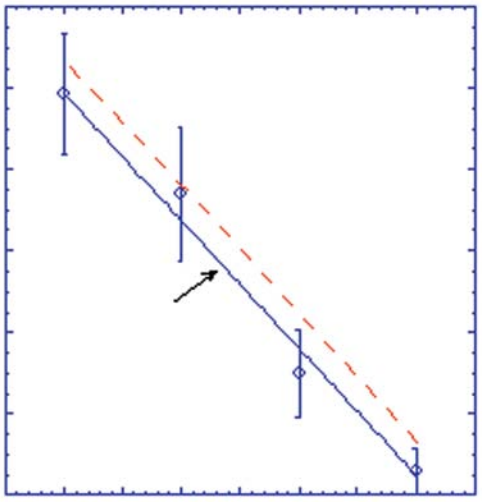

Figure 2. Electric field versus gate bias obtained from the electroreflectance spectra in 1(a)-(d). The electric field predicted by the "standard model" for an $Al_{0.19}Ga_{0.81}N$ (320Å)/GaN heterostructure is indicated by the dotted line.

Nanoscale Structures, Phenomena, and Devices

Size Selection in Self-Assembled Quantum Dot Molecules for Nanologic Devices

by J. A. Floro (Sandia National Laboratories) and Jennifer L. Gray, Nitin Singh, Dana Elzey, and Robert Hull (University of Virginia, Department of Materials Science and Engineering)

Motivation—In order to overcome the fundamental limits that will prevent continued shrinking of microelectronics, revolutionary new quantum computing schemes will be needed within the next two decades. However, if we are to realize the extraordinary information processing potential offered by quantum logic, control at near-atomic length scales is required to build devices based on ordered assemblies of nanoscale quantum dots. While such structures are well beyond the capabilities of standard lithographic techniques, *directed self-assembly* ap-proaches are already demonstrating how complex 3D nanostructures can be constructed via manipulation of the natural processes associated with their growth. We self-assemble quantum dot nanostructures by exploiting intrinsic strain relaxation processes during heteroepitaxial growth of thin SiGe alloy films on Si substrates. This growth/materials strategy is well aligned with current device fabrication procedures, making its acceptance by the microelectronics indus-try far more likely than other techniques for quantum dot production.

Accomplishment—While existing research has emphasized formation of individual quantum dots, we have extended our investigations to self-assembly of quantum dot molecules, (QDMs) which consist of four quantum dots elastically bound together by a central "anti-dot", as shown in Fig. 1. This year we have demonstrated that QDMs prefer a narrowly selected lateral size. Figure 2 shows a statistical summary of the size distributions of QDMs formed of strained $Si_{0.7}Ge_{0.3}$, where both thickness variation and annealing have been em-ployed in order to test the tendency to size se-lect. The result is remarkable—QDMs form the same preferred lateral size even when film thickness is increased by more than 200%, or during annealing for times up to 1600% longer than the QDM growth time. Through experi-ment and modeling we have obtained a heuristic understanding of the origins of size selection. We find that size selection is not thermody-namic; indeed, when annealing temperatures are raised sufficiently, the QDM structure com-pletely breaks down. Instead, QDMs size select due to kinetic limitations associated with the growth conditions. Two factors are at work. First, there is an intrinsic length scale due to the competition between strain and surface energy that governs the formation of the precursor QDM structure. Second, we find that QDM growth stops completely when the four dots coa-lesce to form a continuous ring. This ring effec-tively traps atoms inside, elastically preventing their escape from the central anti-dot region, thereby suppressing QDM enlargement.

Significance—Size selection in QDMs is critically important to their ultimate application in quantum computing. An example is the use of a QDM in a logic architecture based on quantum cellular automata, which requires the use of four-fold QDMs (these are the charge-switching logic elements) that are size-selected (in order to have uniform electronic properties). In collaboration with University of Virginia and Notre Dame University, we have begun exploring the use of our kinetically self-assembled QDMs in this exciting application. Figure 3 shows a SiGe QDM that is being "wired-up" to external test circuitry. Further improvement of our science-based control over these structures may enable a significant advancement in the development of quantum-logic computers.

Sponsors for various phases of this work include: DOE Office of Basic Energy Sciences and National Science Foundation

Contact: Jerrold A. Floro, Surface and Interface Sciences, Dept. 1114
Phone: (505) 844-4708, Fax: (505) 844-1942, E-mail: jafloro@sandia.gov

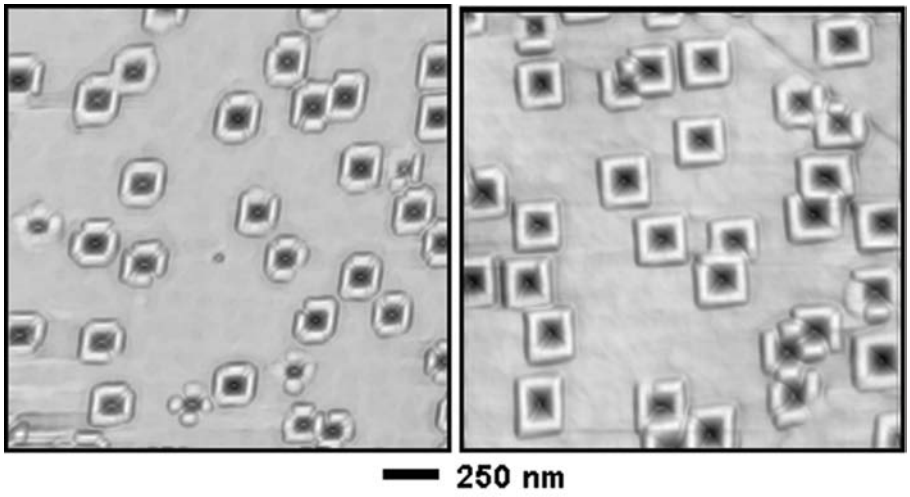

Figure 1. Heteroepitaxial QDMs in $Si_{0.7}Ge_{0.3}$/Si at 200 Å (left) and 300 Å (right) film thickness.

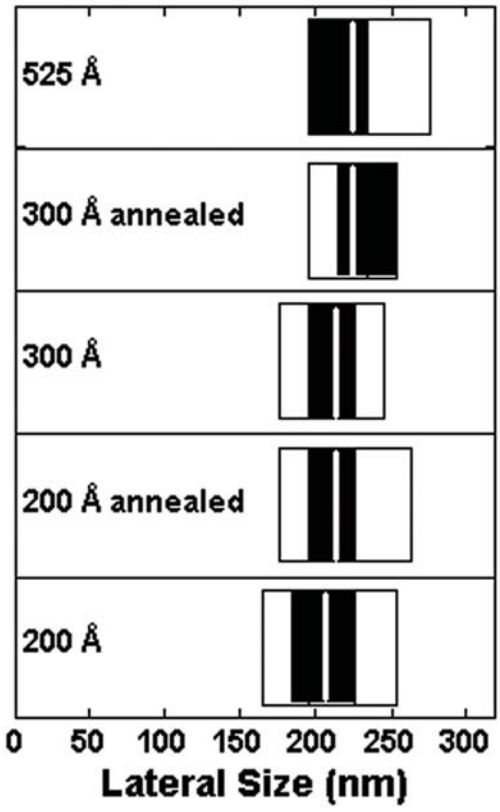

Figure 2. A percentile plot summary of the size distributions for $Si_{0.7}Ge_{0.3}$ films of different thicknesses, with and without annealing. Each open box encloses the inner 90% of the data, each filled box encloses the inner 50% of the data, and the white bar represents the mean.

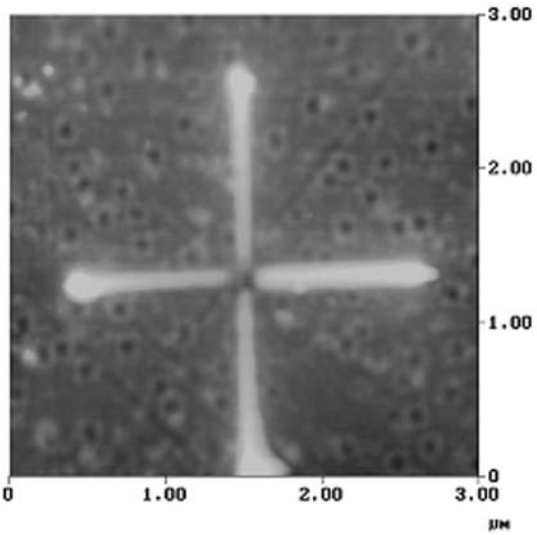

Figure 3. Platinum leads written onto a single QDM using focused ion beam techniques (in collaboration with G. Snider, Notre Dame, and R. Hull, UVa).

Ballistic Transport in 5 μm Quantum Wires

by M. P. Lilly, E. Bielejec, J. A. Seamons, J. L. Reno, S. K. Lyo, and J. A. Simmons

Motivation—In very low disorder two dimensional electron systems, the mean free path of the electron determined from transport measurements can exceed 100 μm. In the same material with a one dimensional (1D) constriction, electrons will travel ballistically (i.e., without scattering) a much shorter distance. Maximizing the length for ballistic transport, and understanding the nature of diffuse transport in longer wires will be crucial for studies of interacting nanostructures such as coupled quantum wires. We present transport results on the ballistic to diffuse crossover in low disorder long single quantum wires.

Accomplishment—Quantum wires of varying length are fabricated in 2D electron systems using a pair of metallic gates separated by a narrow gap where the wire forms (see SEM image in Fig. 1). Low background disorder in the nanostructure is achieved by using semiconductor heterostructures grown by molecular beam epitaxy where the embedded 2D electron system can have a mobility exceeding 10^7 cm^2/Vs. The conductance of a short wire is shown in Fig. 1. In the main panel, the 2D electron gas is initially unconstrained, and the conductance is very high. For $V_{gate}<-0.7$ volts, electrons must flow through the 0.5 μm wide gap between the gates. Further reduction of the gate voltage narrows the wire until the conduction ceases at $V_{pinchoff} \approx -3.0$ volts. Before pinchoff, many plateaus in the two-terminal conductance data are observed. After correction for contact resistance, the plateaus form steps that are spaced by integer values of $2e^2/h$, where e is the charge of the electron and h is Plank's constant. These equally spaced steps in the conductance indicate that transport is ballistic in the 1D wire. For the short wire in Fig. 1, over 14 conductance steps are observed. The large number of steps testifies to the high quality of the quantum wires fabricated at Sandia.

As the length of the quantum wires are increased scattering in the wire becomes important, and eventually a transition from ballistic to diffuse transport occurs. In Fig. 2, data corrected for contact resistance are shown for wires of length 0.5, 5 and 10 μm. In the 5 μm wire, the higher conductance steps are washed out, but the last 4 steps remain quantized at integer multiples of $2e^2/h$, indicating that current flows through the this longer wire without scattering. The absence of quantized steps for the 10 μm suggest that the 1D mean free path is between 5 and 10 μm. We are exploring the role of phonons, roughness and impurity scattering for the significant reduction from the 2D mean free path. Even though conductance steps are not observed for the 10 μm quantum wire, magnetoconductance measurements show some evidence that even for long wires a fraction of the electrons continue to behave ballistically.

Significance—For the high quality 1D wires fabricated at Sandia, electrons travel ballistically in quantum wires exceeding a length of 5 μm. The long 1D mean free path observed in single wires enables the fabrication of more complicated interacting nanostructures. These types of structures are expected to provide the basis for future ultra-low noise detectors and other novel electronics, possibly even quantum computing.

Sponsors for various phases of this work include: DOE Office of Basic Energy Sciences, Nuclear Weapons/Science & Technology, and Laboratory Directed Research & Development
Contact: Michael P. Lilly, Semiconductor Materials and Device Sciences, Dept. 1123
Phone: (505) 844-4395, Fax: (505) 844-1197, E-mail: mplilly@sandia.gov

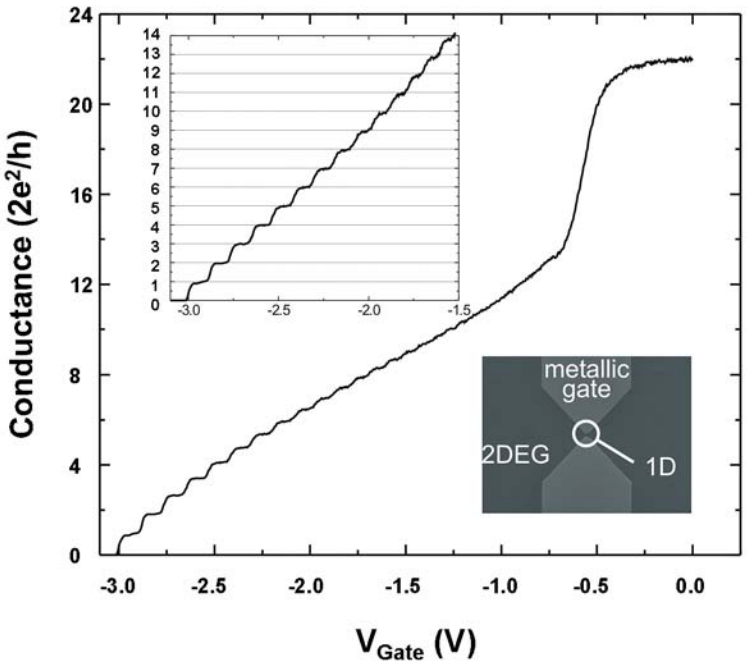

Figure 1. Conductance at $T = 0.3\ K$ as a function of split gate voltage for a quantum wire of length 0.5 μm and width 0.5 μm (SEM image). For $V_{Gate} < -0.7$ V we observe a 2D-1D transition, and as we further deplete the 2D electrons we observe the onset of steps. Upper inset: Quantized conductance steps at integer values of $2e^2/h$ (after correction for contact resistance).

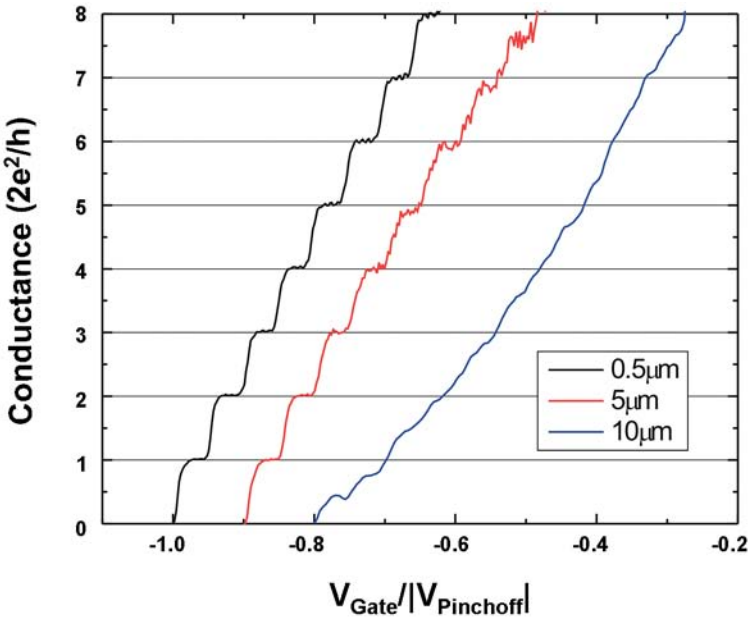

Figure 2. Conductance steps (corrected for contact resistance) for several quantum wires of different length. The gate voltage has been normalized to the voltage where conductance drops to zero ($V_{pinchoff}$) and each curve is offset by 0.1 for clarity. We observe a transition from ballistic to diffuse transport as we increase the length of the wire.

Terahertz Quantum-Cascade Laser Operating Up to 137K

by J. L. Reno

Motivation—Terahertz (1-10 THz, or 4-40 meV, or 30-300 μm) frequencies are among the most underdeveloped electromagnetic spectra, even though their potential applications are promising for spectroscopy in chemistry and biology, detection of trace gas for military and security applications, astrophysics, plasma diagnostics and end-point detection in dry etching processes, remote atmospheric sensing and monitoring, imaging, noninvasive inspection of semiconductor wafers, high-bandwidth free-space communications, and ultrahigh-speed signal processing. This underdevelopment is primarily due to the lack of coherent solid-state THz sources that can provide high radiation intensities (greater than one mW) and continuous-wave (CW) operation.

Semiconductor quantum wells are human-made quantum-mechanical systems in which the energy levels can be designed and engineered to be any value. Consequently, unipolar lasers based on intersubband transitions (electrons that make lasing transitions between subband levels within the conduction band) were proposed for long-wavelength sources as early as the 1970s (Kazarinov & Suris 1971). However, because of the great challenge in epitaxial material growth and the unfavorable fast nonradiative relaxation rate, it took more than two decades to realize this proposal experimentally. Electrically pumped unipolar intersubband-transition lasers (also called quantum-cascade lasers (QCL)) at ~ 4-μm wavelength were first developed at Bell Laboratories in 1994 (Faist *et al.* 1994). Since then, the frequency characteristics have been extended from mid-infrared frequencies to the terahertz range.

Accomplishment—In collaboration with the group at MIT lead by Qing Hu, we have pursued a unique approach to achieve lasing in QCLs at THz frequencies. We have investigated the possibility of using fast LO-phonon scattering to depopulate the lower radiative level (Xu et al. 1997, Williams *et al*. 1999), and using double-sided metal waveguides for THz mode confinement (Xu 1998). These efforts are bearing fruit. The calculated band structure of one such device is shown in Fig. 1a. This structure lased at about 3.8THz. One-dimensional mode profiles were calculated for both the earlier semi-insulating (SI)-surface-plasmon waveguide and the new metal-metal waveguide. The results shown in Fig. 1b-c clearly demonstrate the improved confinement that has been achieved using the metal-metal waveguide. This structure was grown by molecular beam epitaxy on a semi-insulating GaAs substrate with 178 cascaded modules. When the device was fabricated into a ridge structure with the metal-metal waveguide it lased in a pulsed mode up to 137K. Pulsed spectra taken over a range of temperatures are shown in Fig. 2.

Significance—To use QCLs as a compact, coherent THz source in applications, the operating temperature must be raised and cw operation improved. We have significantly extended the temperature range for lasing in resonant phonon terahertz QCLs by improving device design and reducing waveguide losses. Improved design of the injector region, along with improvements in metallic wafer bonding and heat sinking will allow for robust cw operation.

Sponsors for various phases of this work include: Nuclear Weapons/Science & Technology
Contact: John L. Reno, Semiconductor Material and Device Sciences, Dept. 1123
Phone: (505) 844-9677, Fax: (505) 844-3211, E-mail: jlreno@sandia.gov

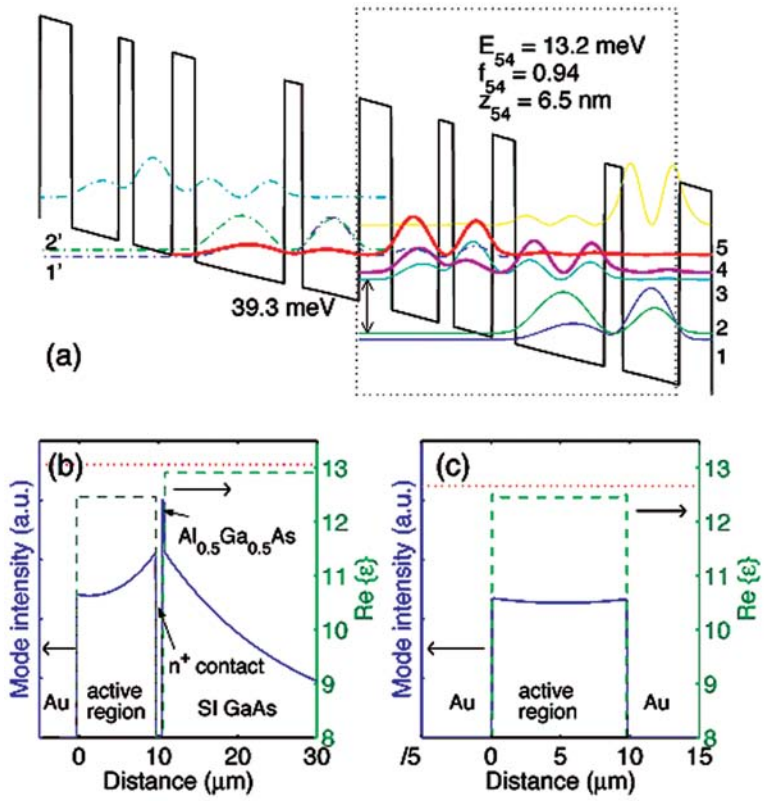

Figure 1. (a) Calculated conduction band profile for the QCL. The lasing transition is from the n = 5 state to the n = 4 state. Also shown are the mode profiles (solid lines) and the real part of the dielectric constant e(w) (dashed lines) for (b) SI-surface-plasmon and (c) metal-metal waveguides.

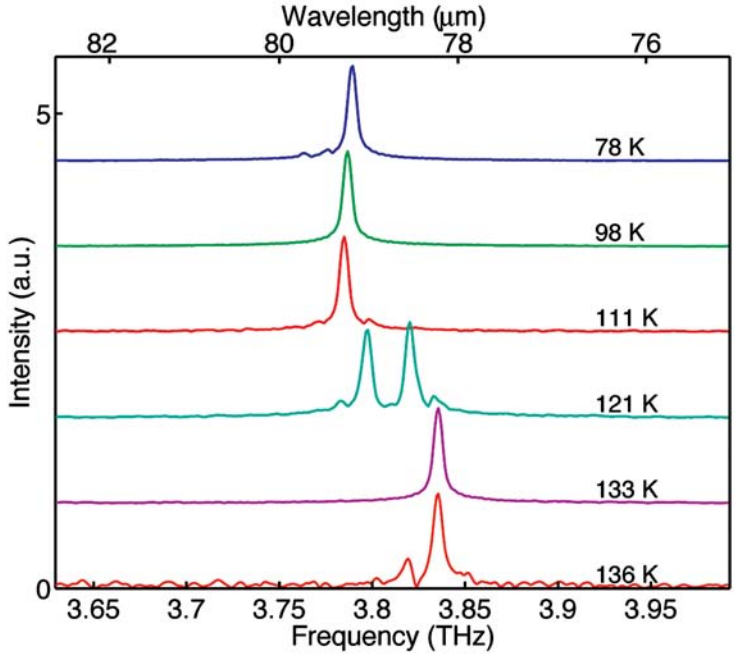

Figure 2. Laser emission spectra taken during pulsed operation at various heat sink temperatures. The linewidth is limited by the spectrometer resolution.

Nanoelectromechanical Oscillators (NEMOs)

by J. P. Sullivan, T. A. Friedmann, D. W. Carr, and J. R. Wendt

Motivation—Mechanical oscillators have been widely used in electronics as frequency sources in timing circuits or filters. The resonance frequency of the oscillator is determined by its material properties and its physical dimensions. Nanolithography permits the creation of nanoelectromechanical oscillators (NEMOs) with critical dimensions of only a few tens of nanometers. These oscillators have high resonance frequencies, in the radio frequency (rf) range, permitting their application in rf circuits. In addition, the low mass and high surface area of the oscillators makes them extremely sensitive to chemical adsorption, and this is useful for chemical sensing applications.

Accomplishment—We have successfully created NEMOs that have a unique structure using nanolithography and microelectromechanical systems (MEMS) surface micromachining of amorphous diamond (a-D). Examples of some of these NEMOs are shown in Fig. 1. These devices consist of an array of singly-clamped beams that are designed to oscillate in the film plane. In an effort to reduce coupling, each oscillator is paired to one neighbor, yet spaced far apart from its other neighbor. (In a future study, coupling between oscillators will be intentionally increased to explore collective behavior in large nanomechanical systems.) This structure is unique in that linear arrays of identical oscillators are actuated, as opposed to the actuation of individual isolated oscillators. Furthermore, the motion is in the film plane, in contrast to out-of-plane motion typically found for most cantilever oscillators. The use of a-D also permits high oscillator resonance frequencies due to the high elastic modulus of this material (about 70% that of crystalline diamond), and it allows the possibility of achieving low surface dissipation due to its atomically abrupt surface, i.e., no surface oxide.

The in-plane array of NEMOs that have been developed in this study permits a novel optical detection scheme. Optomechanical modeling performed by D. Carr (1769) has shown that these NEMO arrays exhibit strong modulation of the optical reflectance normal to the film plane at the oscillator resonance frequency. Measurement of subpicometer motion of the NEMOs is achievable using this technique (patent pending). Figure 2 shows an example of the measured resonance response for one particular NEMO array. The width of the resonance peak provides the quality factor, Q, which is an indication of the amount of internal dissipation in the oscillator. These measurements permit fundamental studies of the factors that control internal dissipation in nanomechanical structures - an important area of study for the development of nanomechanical systems coupled with nanoelectronics and for the development of nanomechanical structures used for single molecule sensing.

Significance—NEMOs are important for enabling miniaturized rf signal processing/ timing circuits, for fundamental studies of internal dissipation in nano-sized structures, for enabling studies of the complex dynamics of large systems using coupled nanomechanical elements, and for providing a platform for the development of extremely high sensitivity chemical or molecular sensors. The NEMOs developed in this work are unique in their design and material of construction and offer promise for rf electronics, sensing, and exploring physics at the nano-scale.

Sponsors for various phases of this work include: Laboratory Directed Research & Development
Contact: John P. Sullivan, Nanostructure and Semiconductor Physics, Dept. 1112
Phone: (505) 845-9496, Fax: (505) 844-4045, E-mail: jpsulli@sandia.gov

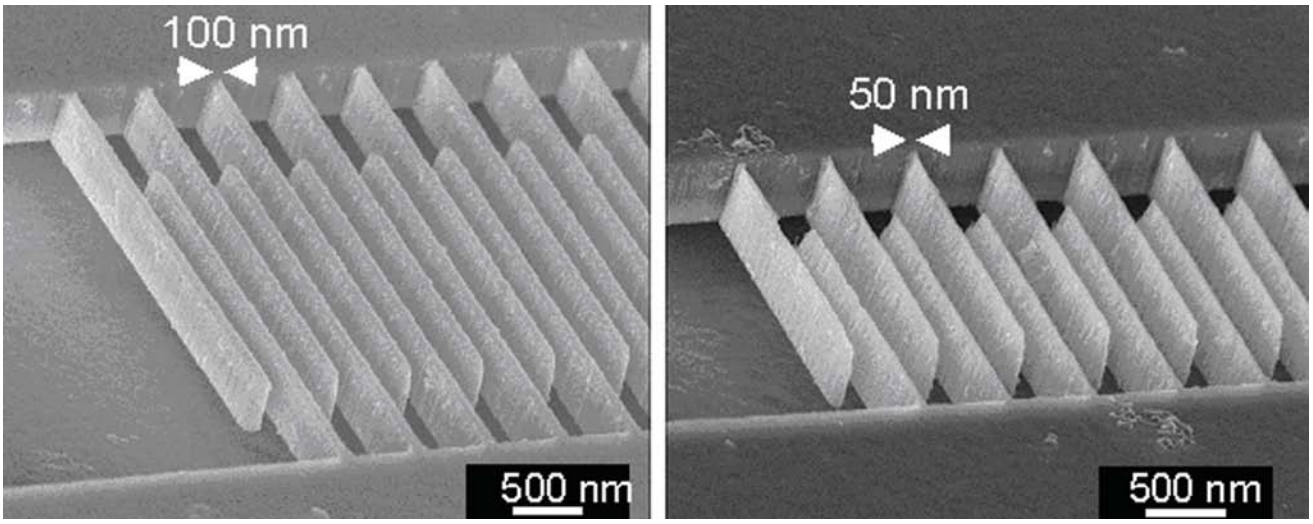

Figure 1. Two examples of NEMO arrays fabricated out of amorphous diamond. The array on the left consists of nanomechanical elements of 100 nm width and 3200 nm length with a design resonance frequency of 25 MHz. The array on the right consists of nanomechanical elements of 50 nm width and 1600 nm length with a design resonance frequency of 50 MHz.

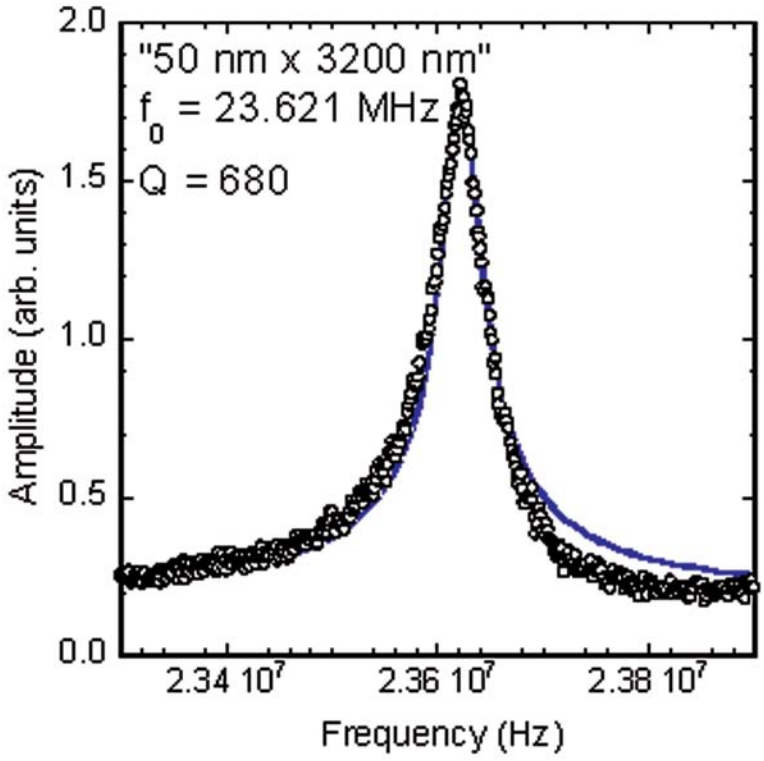

Figure 2. The measured amplitude vs. frequency for a NEMO array of 50 nm by 3200 nm oscillators. The resonance frequency is 23.6 MHz, and the width of the resonance peak is consistent with a quality factor of 680.

Isotope Effects in Ferroelectricity*

by E. L. Venturini and G. A. Samara

Motivation—Displacive ferroelectrics (FEs) are characterized by a coordinated displacement of the atoms within a crystal lattice to produce a static internal polarization. At the FE transition there is a cancellation between the short- and long-range forces acting on the atoms, and the frequency of one displacement mode approaches zero. Hence, the lattice is termed "soft" and the dielectric constant becomes large. When the forces are delicately balanced, isotopic substitution for one of the atoms can produce significant changes in the soft mode behavior. This is the case for $SrTiO_3$. We have combined isotopic substitution of oxygen with the application of hydrostatic pressure to probe the detailed physics of this crystal.

Accomplishment—$SrTiO_3$ with naturally occurring ^{16}O (STO-16) is a classic incipient FE: the frequency, ω_s, of one displacement mode decreases and the dielectric constant, ε', rises with decreasing temperature, but the lattice is stabilized at the lowest temperatures by quantum fluctuations of the atoms. This is shown in Fig. 1 where the dashed red line reflects STO-16 data at ambient pressure: ε' (left axis) rises from ~ 300 at room T to a plateau near 20,000 below 10 K, referred to as the quantum paraelectric state. The soft mode frequency $\omega_s(T)$ can be obtained from these data since $\omega_s \sim 1/\sqrt{\varepsilon'}$. Plotting $10^3/\varepsilon'$ (right axis) shows that the displacive mode becomes very soft as $T \rightarrow 0$, but the lattice remains stable due to quantum fluctuations. This stability is broken in a crystal where 97% of the ^{16}O is replaced by the isotope ^{18}O (STO-18). $\varepsilon'(T)$ for STO-18 (blue triangles, left axis in Fig. 1) has a pronounced maximum near 24 K, indicating an equilibrium transition to a FE state. The heavier isotope induces a FE state by (a) providing an additional softening in ω_s and (b) reducing the quantum fluctuations. The FE in $SrTiO_3$ (the Slater mode shown by the inset in Fig. 1) is primarily a vibration of the Ti ions against their surrounding oxygen octahedra. Replacing ^{16}O by ^{18}O should reduce ω_s by the ratio of the effective masses in the Ti-O_6 octahedral units or 3%. Our dielectric data accurately confirm this prediction: $10^3/\varepsilon'$ (Fig. 1, right axis) for STO-18 lies 6% below STO-16.

Hydrostatic pressure counteracts the softening from ^{18}O substitution as shown in Fig. 2. Using the maximum in $\varepsilon'(T)$ for different P, the FE transition temperature, T_c, is suppressed at a very rapid –20 K/kbar (inset to Fig. 2). $T_c \rightarrow 0$ near 0.7 kbar and the FE state is replaced by the quantum paraelectric state (shown by the plateau in the 0.7 kbar data at low T). The line through the $T_c(P)$ data shows agreement with the theory for quantum ferroelectrics which predicts that $T_c = A \cdot \sqrt{(1 - P/P_c)}$ where $T_c(P_c) = 0$.

Significance—^{18}O substitution induces a FE state in single crystals of $SrTiO_3$. Our dielectric data $\varepsilon'(P,T)$ demonstrate quantitatively the additional softening of the soft mode frequency that enables a displacive equilibrium FE transition. Because this transition occurs at low T (24 K at ambient P), pressure provides an excellent variable to delicately reverse the mode softening and ultimately suppress the FE state at modest P. These large P effects arise from the fact that T_c is low (in the quantum regime) and the characteristic energies are small. The experiments provide new insight and a better understanding of the physics of ferroelectricity in quantum paraelectrics and perovskite materials in general.

*In collaboration with Prof. M. Itoh, Tokyo Institute of Technology

Sponsors for various phases of this work include: DOE Office of Basic Energy Sciences and Nuclear Weapons/Science & Technology

Contact: Eugene L. Venturini, Nanostructures & Advanced Materials Chemistry, Dept. 1122
Phone: (505) 844-7055, Fax: (505) 844-4045, E-mail: elventu@sandia.gov

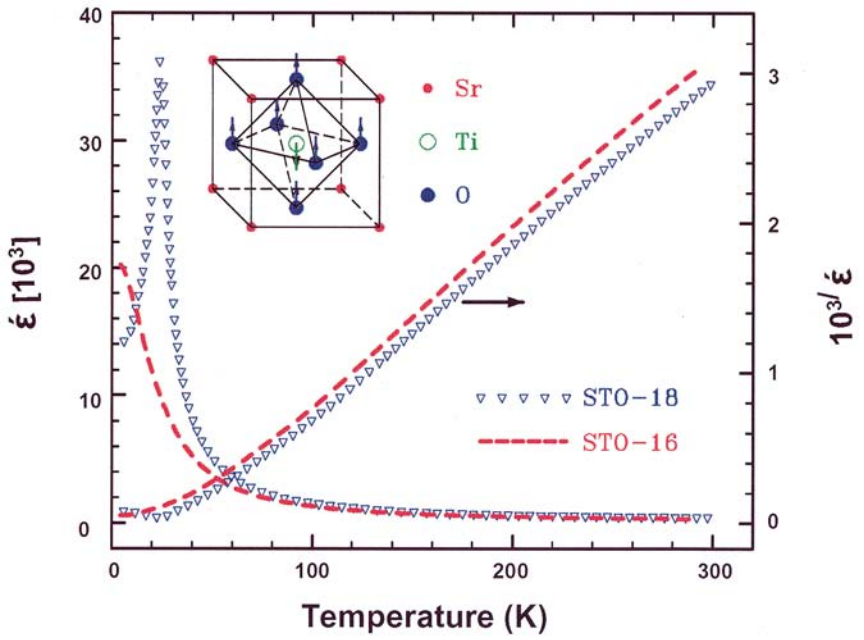

Figure 1. Ferroelectricity in $SrTiO_3$ appears when ^{16}O is replaced by the stable isotope ^{18}O.

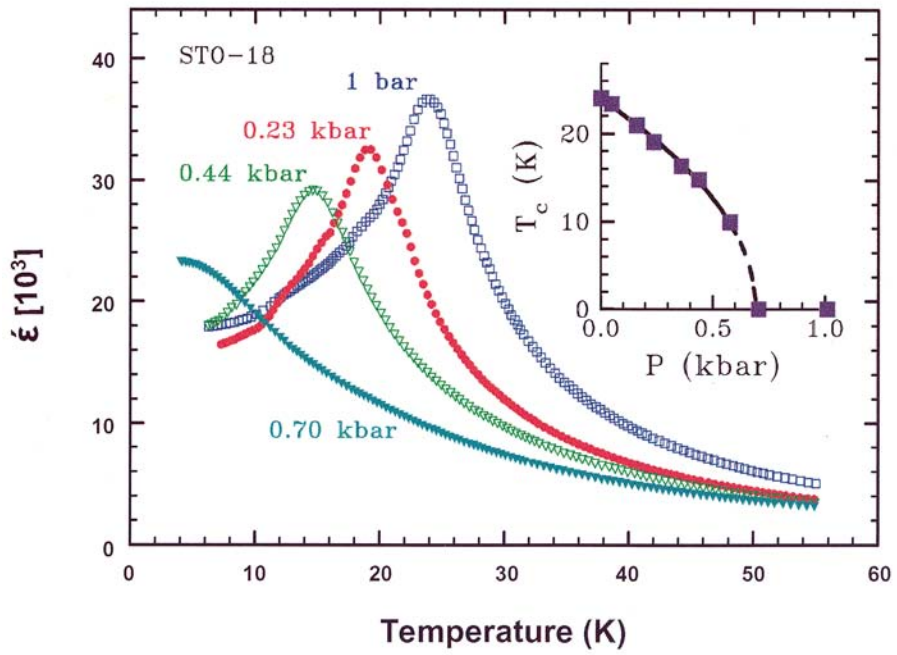

Figure 2. Hydrostatic pressure suppresses the ferroelectric transition in STO-18 near 0.7 kbar.

Hydrogen as a Dopant in Zinc Oxide

C. H. Seager and S. M. Myers

Motivation—Zinc oxide, already a widely used electronic material, has the potential to become an important material for the fabrication of light emitting diodes for short wavelength and white light applications. Two principal problems persist which have stymied the use of this wide-bandgap semiconductor. The first is the lack of a reproducible method for p-type doping, and the second is the poor understanding of the "native dopant" which causes nominally pure ZnO to be always n-type. Recent calculations using density functional theory (DFT) have suggested that hydrogen, which is usually present when ZnO is grown by hydrothermal techniques, might be an important "accidental dopant" in this material.

Accomplishment—In order to make a quantitative connection between the amount of dissolved hydrogen and any observed changes in electrical properties of this material, we have annealed single crystal ZnO samples from several sources in H_2 and D_2 gas at 750°C and compared the observed changes in electron concentration and mobility with Nuclear Reaction Analysis and Secondary Ion Mass Spectrometry profiles of deuterium. In addition we studied the evolution of local vibrational modes of H-related defects before and after these anneals with Fourier Transform Infrared Vibrational Spectroscopy. This study is the first quantitative correlation of H/D densities with carefully measured electrical and optical properties of ZnO. We find that the amount of deuterium remaining in our gas-charged samples ranges from 3.6 to 5.5 x 10^{17} cm^{-3}, substantially larger than the increase in conduction band electron densities deduced from Hall effect measurements. Our modeling indicates that these gas treatments produce a hydrogen-related donor state at 0.036 $\pm$ 0.004 eV below the conduction band minimum (Fig. 1) and also cause significant increases in the measured conduction band electron mobility. Another key finding is the observation of a local vibrational mode of dissolved D at 2619 cm^{-1} and an H analog at 3546 cm^{-1}. These modes are close to the DFT-predicted frequencies for D/H in a bond-centered position between zinc and oxygen. Using this mode as a measure of H content, we deduce that hydrogen is present in significant amounts in as-received samples but is not the "native donor". Using this optical indicator of H content and our modeling of electrical data, we conclude that all of the H in as-received ZnO is passivating acceptor impurities that are unintentionally incorporated during the growth process. When more H or D is deliberately added, it preferentially bonds to un-passivated acceptors, with the remaining amount functioning as an isolated shallow donor. This provides a convincing explanation for both the improved carrier mobilities and the discrepancy between the NRA-measured deuterium densities and the electrically active donor concentrations in our D_2 gas-charged samples.

Significance—These experiments have shown that hydrogen can play a key role in the electronic properties of ZnO. Since we find that hydrogen is present at the 10^{17} cm^{-3} level in most ZnO and it readily binds to acceptor impurities (effectively preventing them from donating holes to the valence band), great care must be taken to control the hydrogen content during growth of p-type ZnO layers for optoelectronic devices.

Sponsors for various phases of this work include: DOE Office of Basic Energy Sciences and Laboratory Directed Research & Development

Contact: Carleton H. Seager, Radiation-Solid Interactions, Dept. 1111
Phone: (505) 844-9168, Fax: (505) 844-1197, E-mail: chseage@sandia.gov

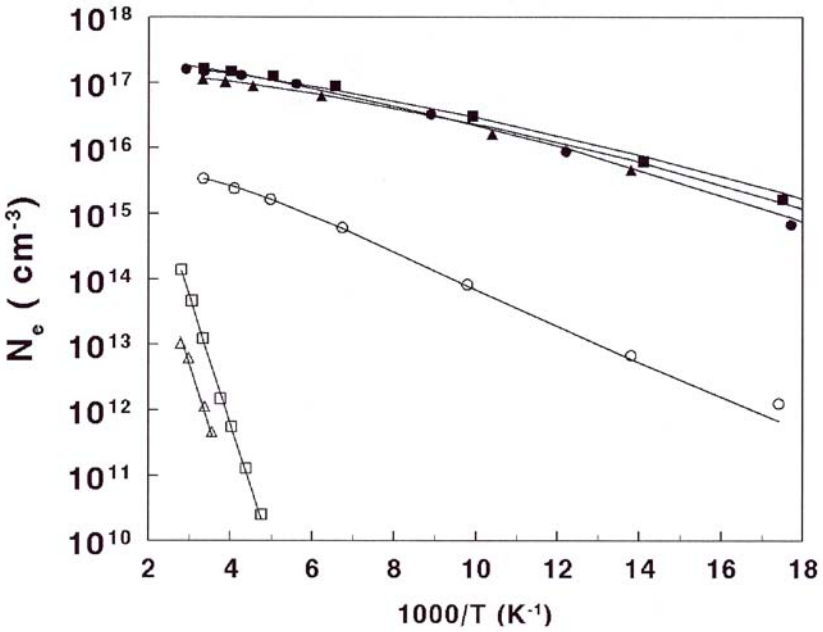

Figure 1. The electron concentration in ZnO from three different growers, plotted as a function of inverse temperature. Open symbols are data from as-received samples, filled symbols are data obtained after anneals in H_2 gas at 750°C. Hydrogen functions both as a shallow donor and as a passivator of pre-existing acceptors, raising the electron concentration in the material and reducing its variation with temperature. Lines are theoretical fits made to deduce donor and acceptor densities.

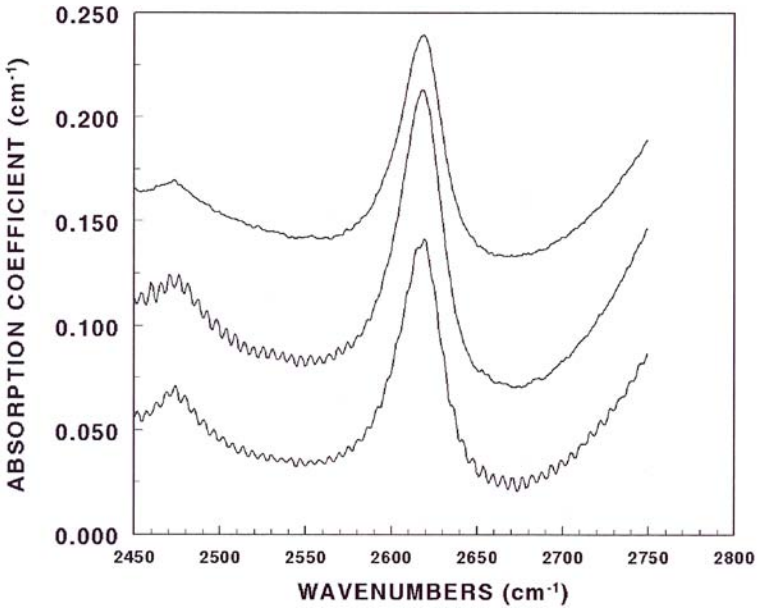

Figure 2. Local vibrational mode spectra of ZnO treated in D_2 gas at 750°C. The peak at 2619 cm^{-1} is consistent with theoretical predictions of the infrared absorption expected from a D atom bonded to oxygen in ZnO. The three spectra are from samples grown by different vendors.

White Light Nanophosphors for Solid State Lighting

J. P. Wilcoxon, S. Woessner, L. Rohwer-Shea, B. Abrams, and S. Thoma

Motivation—Development of highly efficient GaN-based solid-state illumination sources requires new types of phosphors that absorb near UV energy strongly while re-emitting visible, white light. Phosphors based on semiconductor nanoparticles offer advantages compared to conventional powder phosphors including negligible optical backscattering due to the small diameter of the dots. More importantly, we discovered that direct white emission from a single size dot is possible, obviating the need to blend two or more dots of differing size. Use of a single size dot eliminates self-absorbance of the emitted light while maintaining optical transparency in the visible, 450 to 700 nm regime.

Accomplishment—It has been established that semiconductor quantum dots (QDs), due to the confinement of the photogenerated electron-hole (e-h) pairs, have absorbance and emission energies determined by the size of the dot. We have discovered that, for sufficiently small CdS or CdSe dots, with diameters, d ~ 2 nm, the enormous interfacial area of the dots and lack of translational symmetry allows one to independently adjust the absorbance onset and the emission energy. The decoupling of these two features allows one to select a material type and size to match the desired excitation source while changing the interface morphology or chemistry to alter the emission color. Thus, we have demonstrated blue, green, and red emission from a single size QD sample without changing its absorbance onset. Such extremely small dots, like organic dyes, have negligible self-absorbance of their emitted light. For solid-state lighting this allowed us to optimize the QD phosphor optical properties to ensure that 90-100% of the ~ 400 nm excitation LED source is absorbed in the required short optical path. This materials development enabled the first demonstration of spectrally broad, white emission from a single size QD of cadmium sulfide (CdS) by simple changes in the interface passivation of the dot. The absorbance edge was selected to match the excitation energy of a Cree™ UV LED, while techniques for incorporating the QDs into a transparent epoxy dome without agglomeration of the dots were developed. The latter is key to maintaining high fluorescent quantum yields. Our white emitting device is shown in Fig. 1, while Fig. 2 compares the spectral energy distribution of our nanophosphor to that of the most commonly used GE "soft-white" conventional phosphor used in fluorescent lighting. (This GE phosphor has no absorbance above 300 nm and so cannot be used with an LED) It is possible to obtain subtle shifts in the tint of the white coloration of our CdS QD nanophosphor by further changes in the surfactant used to passivate the surface, shifting the broad energy distribution to either the blue or the red of that shown in Fig. 2, yielding a blue-white or orange-white nanophosphor. We measured a record quantum efficiency of 60% from the encapsulated blue-white QD phosphors in an actual device.

Significance—The use of near-UV LEDs in white light illumination sources requires novel phosphors which can efficiently re-emit all the absorbed ~ 400 nm excitation. Conventional white light phosphors fail to absorb this energy while larger QD phosphors suffer from self-absorbance, which makes white light production by mixing of blue, green, and red emitting QDs very difficult. We have shown that smaller dots, with over 70% of their atoms at surface sites, can have their emission energies tuned by changes in the interface passivation alone, while their absorbance is determined by their size and remains invariant. The basic scientific principle of separation of absorbance from emission in very small QDs is extendable to novel systems, such as Si or Ge QDs doped with emitting ions like Mn.

Sponsors for various phases of this work include: DOE Office of Basic Energy Science and Laboratory Directed Research & Development

Contact: Jess P. Wilcoxon, Nanostructures and Advanced Materials Chemistry, Dept. 1122
Phone: (505) 844-3939, Fax: (505) 844-4045, E-mail: jpwilco@sandia.gov

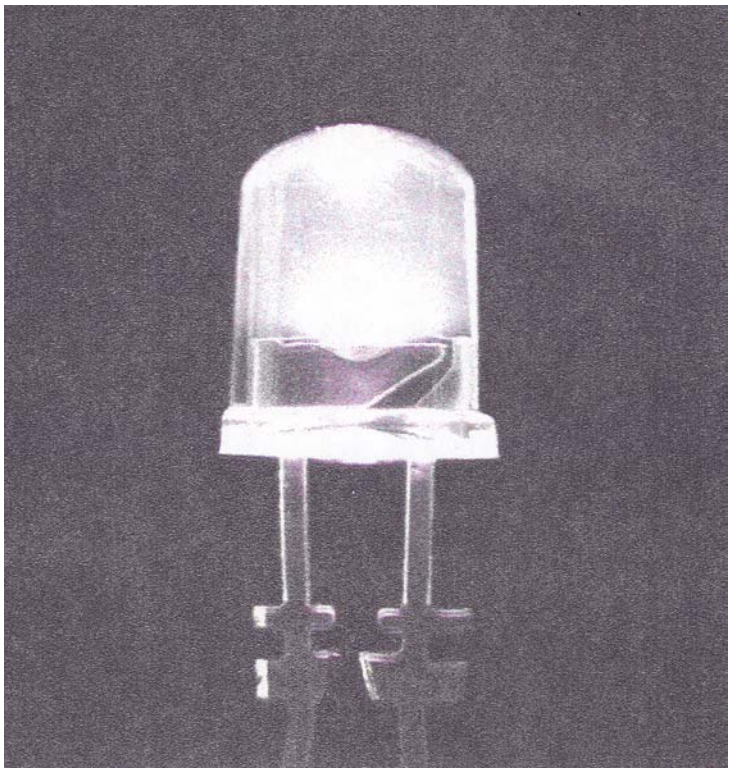

Figure 1. Photograph of a white light emitting LED using a commercial CREE 390 nm excitation LED and d = 2 nm CdS quantum dots incorporated into the epoxy dome.

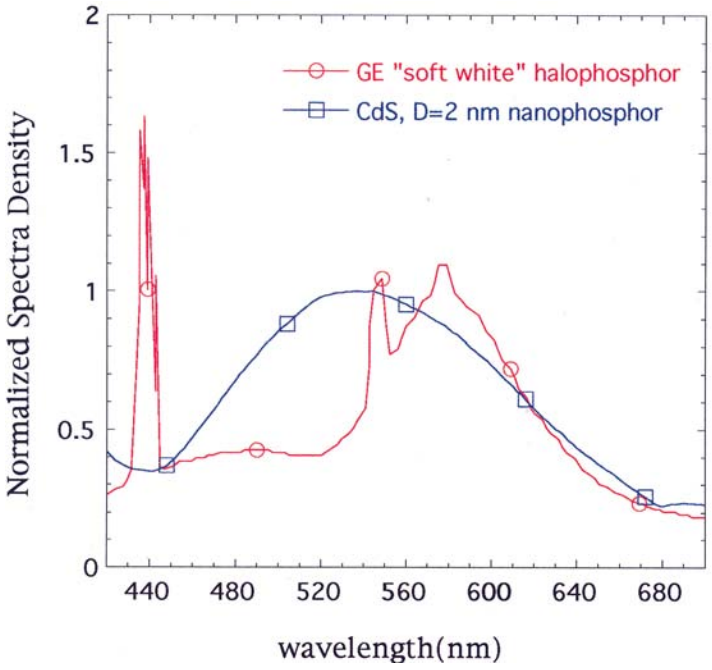

Figure 2. Spectra Energy Density of a white emitting CdS nanophosphor compared to that of a commercial GE "soft-white" phosphor used in fluorescent lamps. The latter must be excited below 300 nm, and thus cannot be used with a GaN-based LED.

Science of Surfaces and Interfaces

Electric Field-Dependent Diffusion Mechanisms of Ge-Si Dimers on Si(001)

by B. S. Swartzentruber, L. M. Sanders, R. Stumpf, and T. R. Mattsson

Motivation—The desire to develop ever smaller functional electronic and mechanical structures—in which just a few atoms out of place could destroy their utility—necessitates a complete understanding of atomic motion at solid surfaces and material interfaces. This is particularly important during heterogeneous growth where surface diffusion could lead to undesirable alloying or unintended segregation. The exploration of compound semiconductor structures, such as Si-Ge quantum dots, for future nanoelectronic devices motivates the present diffusion studies.

Accomplishment—When Ge atoms are deposited onto a Si(001) surface they pair with Si atoms to form dimers. These heterogeneous Ge-Si dimers are adsorbed on the surface and become mobile at elevated temperatures. Using an atom-tracking scanning tunneling microscope (STM), we measured the diffusion rate of adsorbed Ge-Si dimers on Si(001) as a function of electric field at 100 ^{o}C. Because the diffusion rate depends exponentially on the diffusion barrier, small changes in the barrier can be easily measured.

The measured field dependence for Ge-Si dimers is strikingly different than that for pure Si-Si dimers. The diffusion barrier of Si-Si dimers increases monotonically as the applied field is changed from negative to positive, i.e., a continuous positive slope. However, in the case of Ge-Si dimers, the slope changes from positive to negative as the applied field changes sign. These data are shown at the top of Fig. 1. At positive field we observe that the Ge atom in the adsorbed dimer is about 10 times more likely to exchange into the substrate than at negative field. Although the dimers sit at individual sites long enough to measure where they are, the transition from one site to the next happens so fast that the pathway cannot be measured experimentally. Fortunately, state-of-the-art first-principles calculations can determine the relative likelihood of arbitrary paths. With theory, the problem lies in determining which paths are actually relevant. We used density functional theory, modified to include the effect of an externally applied electric field, to investigate the field dependence of various low-energy diffusion paths.

We found two distinct processes that have the same diffusion barrier within the uncertainty of the calculations. In so-called "walking" diffusion, the dimer bond remains intact throughout the transition and is oriented parallel to the substrate dimer bonds. In "piecewise" diffusion, the dimer bond is substantially stretched at the transition state and is oriented perpendicular to the substrate dimer bonds. The key feature of the calculations is that the electric field dependence for the two processes is opposite to each other. The results of the calculations are shown at the bottom of Fig. 1. Comparison of the theoretical calculations with the measurements enables us to conclude that the diffusion process in negative field is that of walking diffusion, whereas, in positive field the dimers diffuse via the piecewise mechanism.

Significance—The electric field-dependence is a new way to control both the diffusion rate and material mixing during growth. As a research tool, field-dependent kinetic measurements combined with state-of-the-art first-principles total energy and barrier finding calculations provide a means to experimentally probe otherwise elusive transition state structures.

Sponsors for various phases of this work include: DOE Office of Basic Energy Sciences
Contact: Brian S. Swartzentruber, Surface and Interface Science, Dept. 1114
Phone: (505) 844-6393, Fax: (505) 844-1197, E-mail: bsswart@sandia.gov

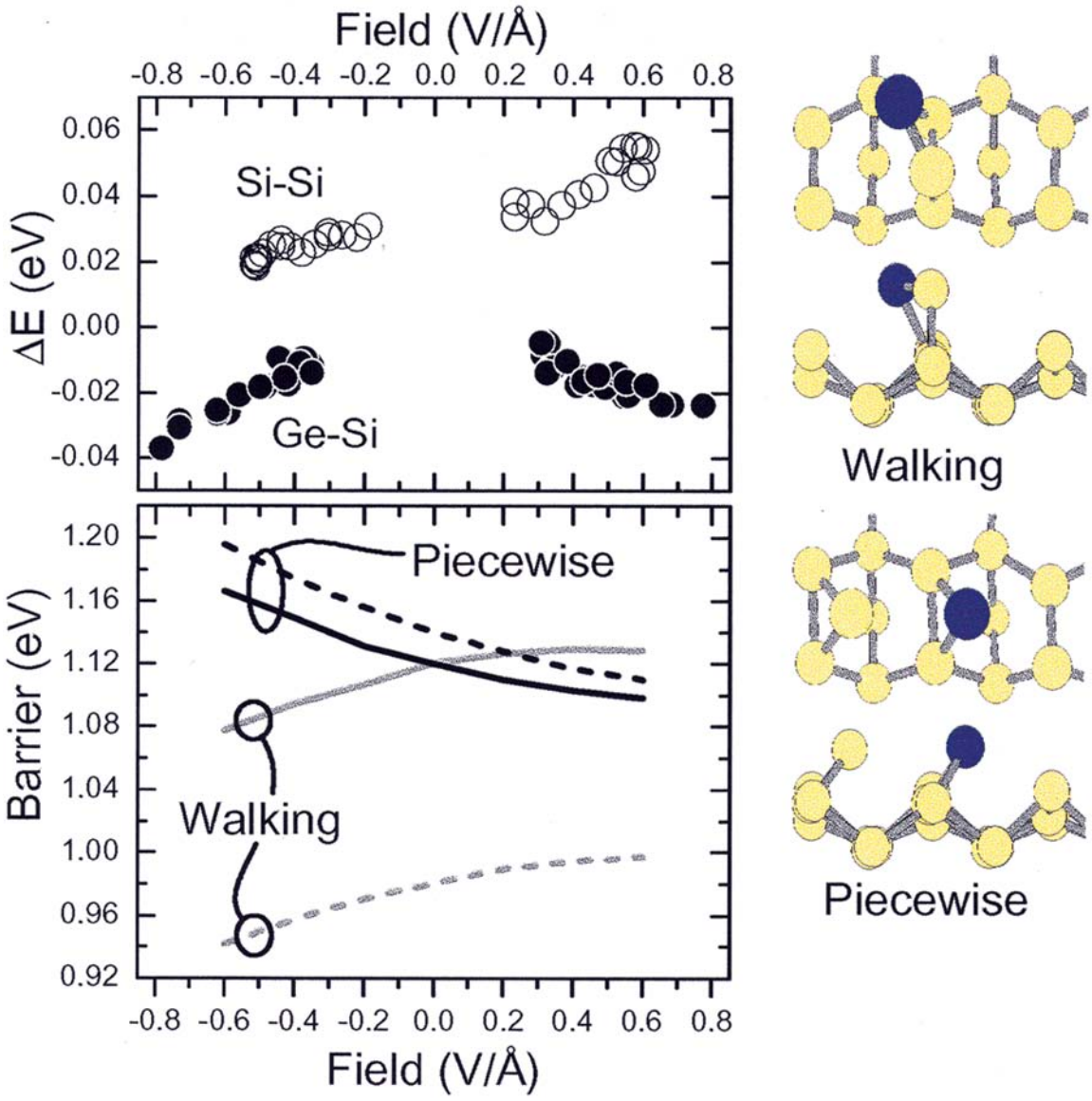

Figure 1. Measured (top) and calculated (bottom) electric field dependence of adsorbed-dimer diffusion barrier on Si(001). Solid symbols are the measured change in Ge-Si barrier relative to the interpolated zero-field value. Open circles are measured Si-Si values offset from the Ge-Si data by their relative rates at at –0.4 V/Å. The bottom panel shows the calculated barrier values for the two Ge-Si diffusion mechanisms, "walking" and "piecewise". Solid (dashed) lines are the LDA (GGA) results. Models of the transition states of the two processes are shown at the right.

Multiscale Modeling of Small Molecules in Zeolite-4A

by N. A. Modine and M. E. Chandross

Motivation—Confinement within the nanoscale pores of a zeolite strongly modifies the physical and chemical behavior of small molecules such as water, ammonia, and carbon dioxide. Realistic modeling of such phenomena requires simultaneously capturing the detailed behavior of chemical bonds and the possibility of collective dynamics occurring in a complex unit cell (672 atoms in the case of Zeolite-4A). Classical simulations alone cannot reliably model the breaking and formation of chemical bonds, while quantum methods alone are incapable of treating the extended length and time scales characteristic of complex dynamics. Therefore, we have taken a mixed quantum/ classical approach in which we embed a small region treated with the Kohn-Sham density functional theory (DFT) within a larger system represented by classical potentials.

Accomplishment—A key ingredient of an efficient and accurate quantum-to-classical coupling is the reformulation of the DFT in terms of a spatially localized set of electronic state functions. In order to obtain such a localized representation of the electronic structure, we have implemented and compared two alternative approaches, one based on Green's function techniques and the other using the Grassmann Conjugate Gradient algorithm. We have found that these approaches have complementary strengths, and are currently engaged in developing a hybrid approach that we believe will combine the advantages of both. These approaches are implemented in fully functional software, and we have integrated the Socorro *ab initio* electronic structure code with the LAMMPS classical molecular dynamics code in order to obtain an initial length-scale-bridging dynamic model. On the materials science front, we have investigated ion rearrangements, modifications of the cage structure, and the absorption of three molecules (water, ammonia, and the ammonium ion) in Zeolite-4A. Unlike previously studied systems, we have found that these molecules prefer to absorb into the 8-oxygen rings of the zeolite structure, where crowding effects between the absorbed molecules and the native ions are important. Based on these observations, we are investigating a possible explanation for the irreversible aging observed in zeolite-based weapons desiccants. In order to perform these studies, we have developed a hierarchy of models for the Zeolite-4A system including one-eighth cell and one-half cell models. These models capture many of the important features of Zeolite-4A, but the strict Si-O-Al alternation of the cage is interrupted. We are currently systematically evaluating the accuracy of this hierarchy of models.

Significance—This project provides the basic principles and techniques to understand the aging of Zeolite-based desiccants (used in most modern weapons systems) and to predict the effects of environmental changes following refurbishment. The scientific understanding and approaches developed in this project will serve as a prototype for studying other complex materials involving the interplay of chemistry and collective phenomena. The software developed in this project will provide a flexible, efficient, production-level tool for materials science research.

Sponsors for various phases of this work include: Laboratory Directed Research & Development and Advanced Strategic Computing Initiative

Contact: Normand A. Modine, Nanostructure and Semiconductor Physics, Dept. 1112
Phone: (505) 844-8412, Fax: (505) 844-1197, E-mail: namodin@sandia.gov

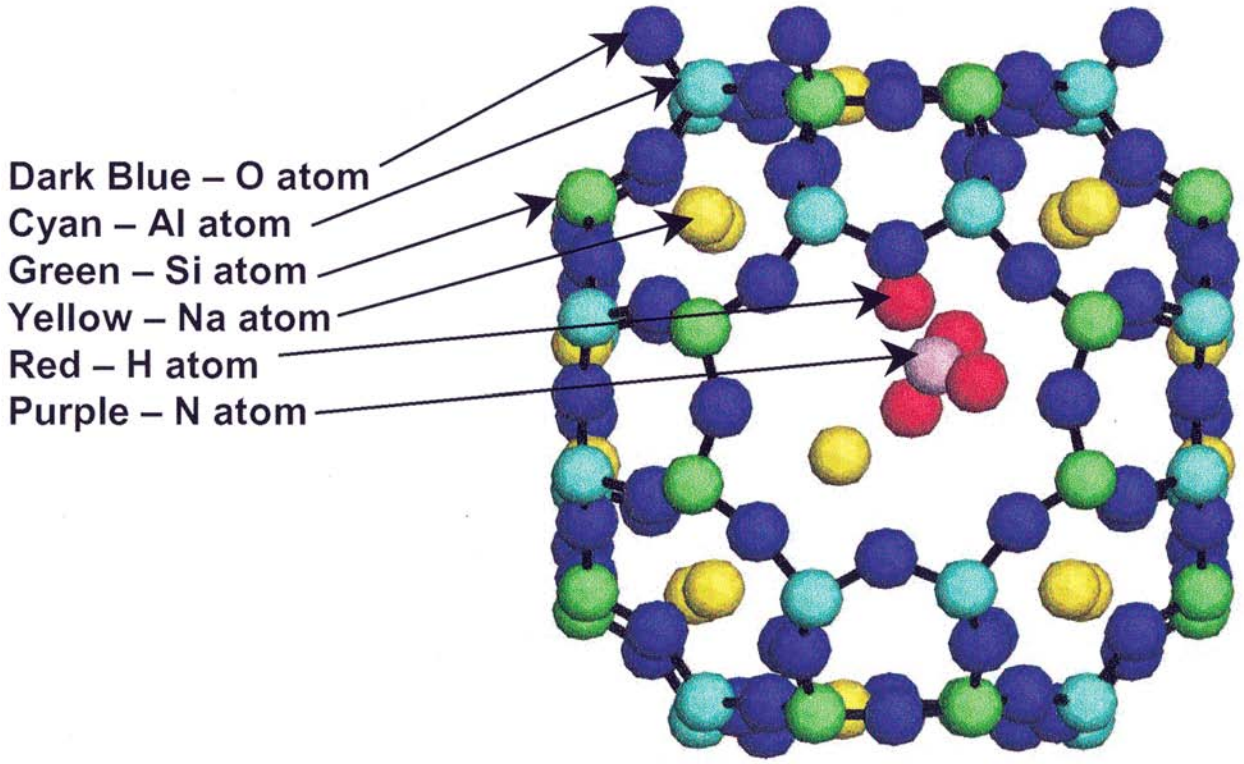

Figure 1. Low energy configuration of an ammonium ion absorbed in our one-eighth cell model of Zeolite-4A. The ammonium ion may block the movement of water through the 8-oxygen ring, reducing the ability of zeolite-based desiccants to absorb water.

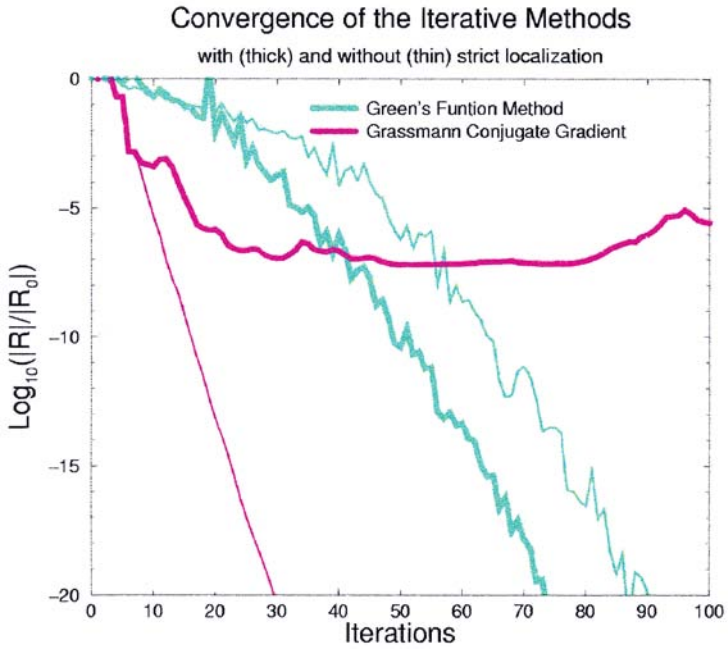

Figure 2. The Green's function method converges rapidly when the orbitals are not strictly localized (forced to be zero outside some radius), but it fails to converge with strict localization. The Grassmann Conjugate Gradient algorithm converges more slowly, but it is also more robust.

Ab Initio Molecular Dynamics and Multiscale Simulation of Formate Ion Hydration—a Comparative Study

by Kevin Leung and Susan B. Rempe

Motivation—The interaction of water with molecular/ionic species and material surfaces is crucial to understanding biology, corrosion, water transport in nanochannels, adhesion, and wetting of microelectromechanical systems (MEMS) components. A major theoretical goal is to accurately model hydration structure using multiscale, quantum mechanics/molecular mechanics (QM/MM) methods. In this scheme, the solute or surface atoms, and sometimes the first hydration shell water molecules, are treated quantum mechanically, while cost-effective empirical force fields suffice for the rest of the water. The accuracy of existing QM/MM results has never been systematically tested. For the biologically important glycine tautomerization reaction in water, QM/MM in fact strongly overestimates free energy differences between tautomers. This is a prototype proton transfer reaction, and its modeling aspects are pertinent to acid/base related problems like corrosion and geochemistry. Our goal is to improve the accuracy of existing multiscale methods by (a) implementing existing QM/MM methods; and (b) performing costly but accurate, purely *ab initio* molecular dynamics simulations as benchmarks. Glycine molecule fragments will be used as test cases.

Accomplishment—We implemented a QM/MM capability into the Vienna atomistic simulation package (VASP) and applied it to analyze glycine hydration. There are two functional groups in glycine, namely the ammonium and carboxylate groups. We treat these fragments—the ammonium (NH_4^+) and formate ($HCOO^-$) ions—quantum mechanically, and model water molecules using force fields. *Ab initio* molecular dynamics predictions for NH_4^+ hydration exist in the literature but not for $HCOO^-$. Thus we also simulate formate ions solvated in water, with all species treated quantum mechanically. VASP as well as CPMD (the Car-Parrinello Molecular Dynamics code) are used.

Figure 1 compares the formate ion-water pair correlation functions at ambient conditions as predicted by *ab initio* molecular dynamics and QM/MM methods. The results are significantly different. The former predicts roughly two and a half hydrogen bonds between water and each HCOO- formate oxygen, in agreement with recent experiments. Figure 2 depicts snapshots of the hydration structure. In *ab initio* molecular dynamics, one formate oxygen typically forms two hydrogen bonds while the other forms three. In contrast, QM/MM incorrectly predicts a total of seven hydrogen bonds, similar to molecular dynamics simulations where all species are treated empirically. On the other hand, the hydration structure of NH_4^+ is well predicted by QM/MM methods.

Significance—This work shows that the accuracy of multiscale QM/MM methods needs to be improved and benchmarked against *ab initio* molecular dynamics simulations and experiments. Much of the body of existing, widely accepted theoretical results, including those pertaining to water interacting with biomimetic, COOH group-functionalized surfaces, needs to be re-evaluated. Sandia's theoretical and computational expertise is leading to improved multiscale methods.

Sponsors for various phases of this work include: Advanced Strategic Computing Initiative, Laboratory Directed Research & Development, and Nuclear Weapons/Science & Technology
Contact: Kevin Leung, Nanostructure and Semiconductor Physics, Dept. 1112
Phone: (505) 844-1588, Fax: (505) 844-1197, E-mail: kleung@sandia.gov

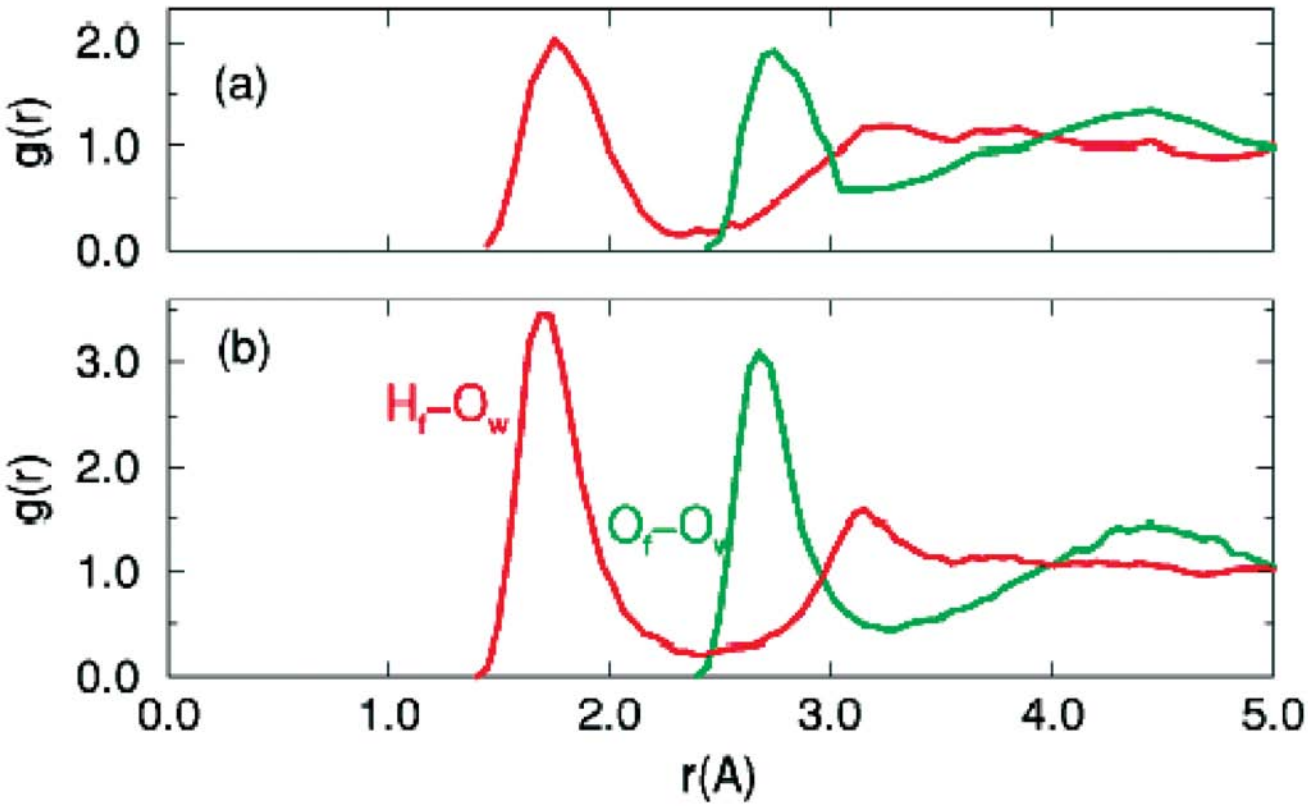

Figure 1. Pair correlation functions between the oxygen and hydrogen sites of the formate ion and the oxygen atom in water molecules. (a) *ab initio* molecular dynamics; (b) QM/MM.

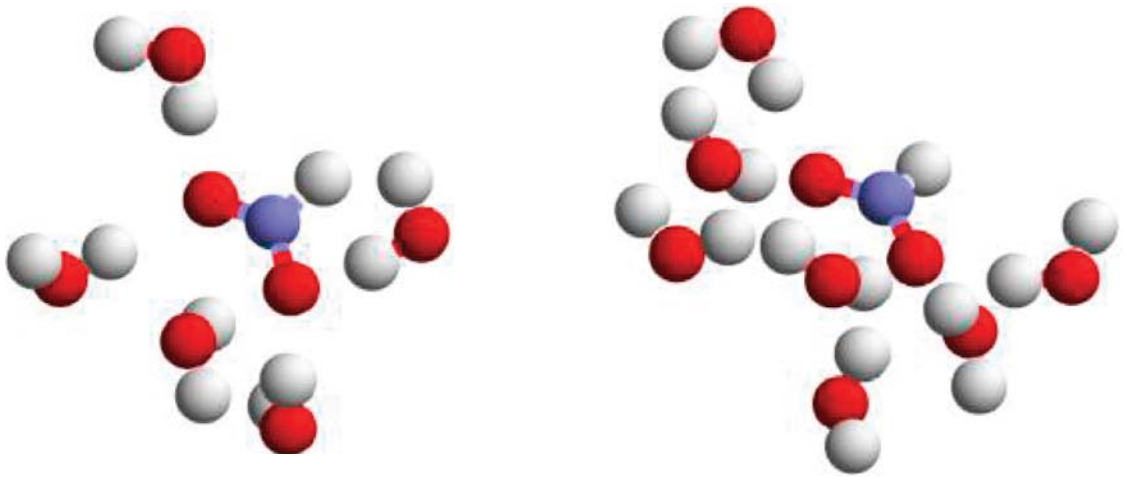

Figure 2. Snapshots of formate ion in water. Oxygen, hydrogen, and carbon atoms are depicted as red, white, and blue spheres, respectively. Left panel: *ab initio* molecular dynamics; right panel: QM/MM. They predict 5 and 7 water molecules in the first hydration shell, respectively.

Erosion of Materials by Fusion Plasma and Implications for U.S. and International Magnetic Fusion Energy Programs

by W. R. Wampler

Motivation—Erosion and redeposition of materials by fusion plasmas impacts lifetime of plasma-facing components and tritium inventory that are critical issues for next-step magnetic fusion energy devices such as the International Thermonuclear Experimental Reactor (ITER). Erosion and deposition of materials by fusion plasmas are complex processes, and experiments are necessary to determine rates of erosion and deposition in tokamaks. Ion beam analysis (IBA) is one of the principal experimental methods to examine erosion and redeposition and has been used at most tokamaks throughout the world. The Ion Beam Materials Research Laboratory (IBMRL) at Sandia, in collaboration with US Plasma Physics Laboratories, has been conducting experiments to measure rates of erosion and deposition in US tokamaks.

Accomplishment—Early studies in the TFTR tokamak at the Princeton Plasma Physics Laboratory (PPPL) showed that a large fraction (40%) of deuterium used to fuel plasmas remained inside the vessel due to codeposition with carbon eroded from plasma-facing components. These IBA measurements of fuel retention provided key information needed to plan subsequent tritium plasma operation and machine conditioning procedures in TFTR that led to the achievement of 11 MW fusion power with the constraint of keeping the on-site tritium inventory below 5 grams.

Erosion and redeposition of materials by divertor plasmas have been extensively studied using the Divertor Materials Evaluation System (DiMES) in the DIIID tokamak, which enables controlled exposure of probes to well characterized plasmas. The rate of erosion at the outer strike-point (OSP) was measured for various materials and plasma conditions. Erosion rates decreased with increasing atomic mass (see Fig. 1) consistent with erosion by physical sputtering by light ions. Erosion of carbon is also enhanced by hydrocarbon formation. Detaching the edge plasma through cooling by injecting deuterium gas greatly reduced erosion, but cooling by injection of neon caused very high carbon erosion.

Erosion, deposition and deuterium retention were also studied in Alcator C-Mod at MIT, which has molybdenum instead of carbon plasma-facing components. The erosion rate of molybdenum was low and similar to values measured in DIIID (see Fig. 1). Deuterium retention was also low. These results show that codeposition with redeposited material, the principal mechanism of long-term deuterium retention in tokamaks with carbon plasma facing components, is greatly reduced in C-Mod. Sandia and PPPL are also conducting studies of erosion, deposition and wall conditioning in the National Spherical Torus Experiment (NSTX).

Significance—The design and choice of plasma-facing materials for next-step magnetic fusion experiments are based on knowledge obtained from studies of erosion and deposition in present machines. Carbon components are widely used in present tokamaks because of their resistance to thermal damage, but have erosion and tritium retention rates that are unacceptably high for next-step machines. Proposed burning plasma experiments, ITER and FIRE, thus avoid carbon where possible and use beryllium in the main plasma chamber and tungsten in the divertor (see Fig. 2). Divertor plasmas will be detached to reduce heat flux and erosion in the divertor. These next step machines will explore burning plasma conditions required for a fusion reactor and are planned to be built and tested in the next decade.

Sponsors for various phases of this work include: DOE Office of Fusion Energy Sciences
Contact: William R. Wampler, Radiation-Solid Interactions, Dept. 1111
Phone: (505) 844-4114, Fax: (505) 844-7775, E-mail: wrwampl@sandia.gov

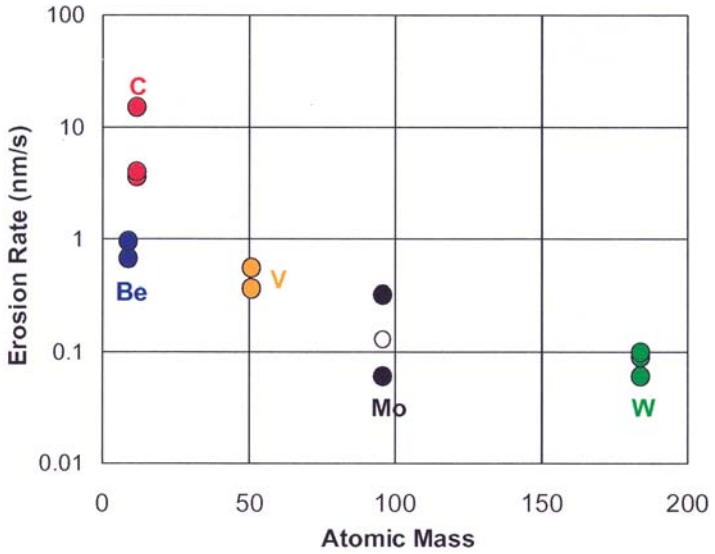

Figure 1. Erosion rates of various materials measured by IBA at the divertor strike point in DIIID (solid symbols) and C-Mod (open symbol) tokamaks.

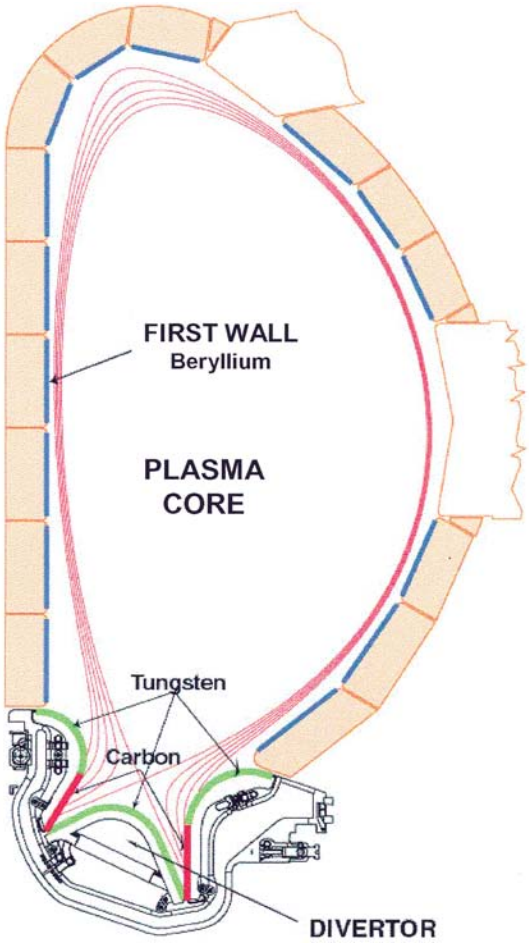

Figure 2. The ITER design uses a beryllium wall in the main plasma chamber, and a lower divertor with carbon and tungsten. The nested red lines show magnetic field contours in the plasma boundary.

Self-Assembly of Organic Semiconducting Films from Oligothiophene Surfactants

by D. Y. Sasaki

Motivation—Conductive organic materials offer the promise of easily fabricated thin films for a variety of applications, such as backlit displays for light emitting diode (LED) devices and low-end storage materials. Among the many materials that have been prepared and tested, the poly- and oligo-thiophenes offer some of the best ion mobilities and on/off rates to date. In terms of processability, however, the polythiophenes are problematic with their low solubility in most solvents and high temperatures needed for vacuum deposition. Alternative routes for film preparation use oligothiophenes with pendent functionality to improve solubility, but environmentally harmful solvents must typically be used. Through proper design of the headgroup and oligothiophene dimensions we hoped to develop a surfactant that disperses and self-organizes in water.

Accomplishment—We designed molecule **1** as our first entry into the development of aqueous phase lyotropic oligothiophene surfactants. By connecting a short oligoethylene glycol on one end of a tetrathiophene unit a surfactant of cylindrical dimensions could be prepared that should have the tendency to form lamellar bilayer assemblies in water. Surfactant **1** was prepared synthetically through Stille coupling to form the tetrathiophene moiety and Williamson ether synthesis to attach the hydrophilic triethylene glycol headgroup.

Sonication of **1** in pure water produced clear dispersions of small vesicles. Dynamic light scattering (DLS) measurements of the solutions found that the dispersed surfactant formed a narrow distribution of 83 ± 5 nm diameter particles. Interestingly, the size and distribution were independent of surfactant concentration. Transmission electron microscopy (TEM) of the particles found them as unilamellar vesicles with elliptical shape (Fig. 1).

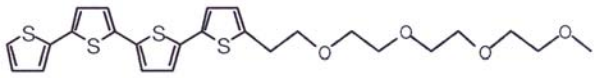

1

Films cast from water, organic solvent, and from tetraethylorthosilicate sol spontaneously formed ordered lamellar structures on glass substrates. X-ray diffraction (XRD) measurements of the sol-gel films found that the surfactants formed stacked lamellae with a perpendicular orientation of the surfactants to the glass surface (Fig. 2).

In a preliminary study, we performed a bulk conductivity measurement of these cast films. The undoped films exhibited conductivity on the order of 10^{-7} $\Omega^{-1}cm^{-1}$, which is of similar range for typical undoped organic semiconductor materials. Signs of photoconductivity were also observed as well as a negative effect of electrical conductivity towards humidity.

Significance—The ability of π-conjugated materials to form ordered and oriented supramolecular structures is essential for the electronic performance of these materials. The oligothiophene-containing molecule **1** forms bilayer structures in water and as cast films on solid substrates. This molecule provides a route towards the preparation of highly oriented and packed superstructures of organic conductors via an environmentally safe deposition solvent.

Sponsors for various phases of this work include: DOE Office of Basic Energy Sciences
Contact: Darryl Y. Sasaki, Biomolecular Materials and Interfaces, Dept. 1141
Phone: (505) 845-0824, Fax: (505) 844-5470, E-mail: dysasak@sandia.gov

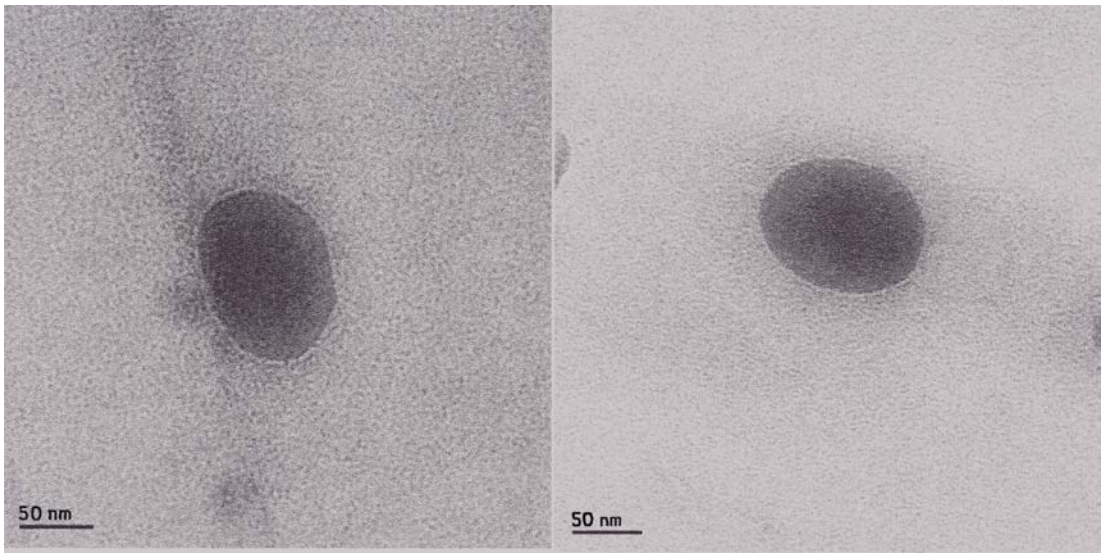

Figure 1. Cryo-TEM images of vesicles of surfactant **1** prepared in water and stained with ammonium molybdate. These images are representative of the structures visible in the sample revealing their ellipsoidal shape and narrow size distribution.

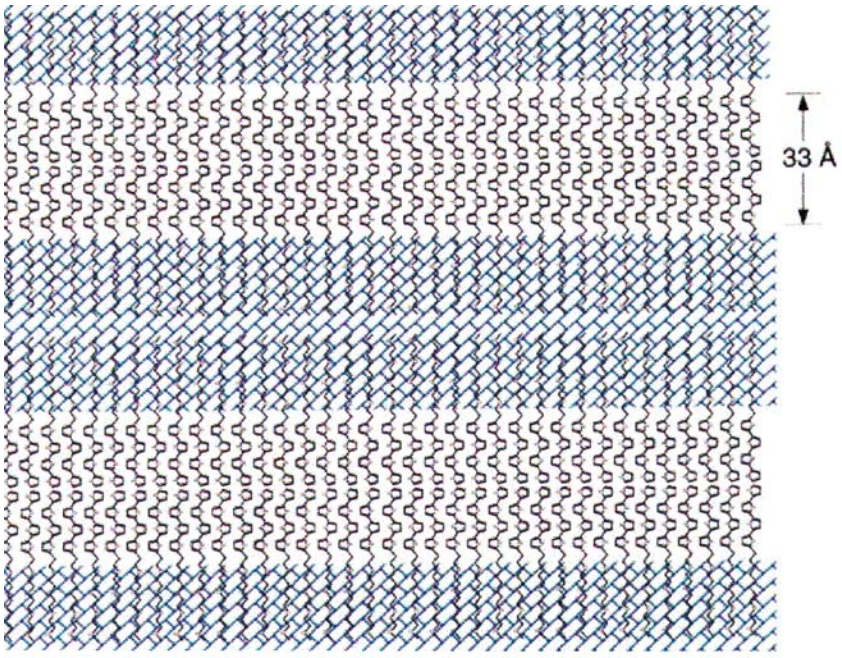

Figure 2. Illustration of the lamellar structure formed from TEOS sol-gel dip-cast film with **1**. XRD measurement of the film showed a spacing of 33Å, consistent with the hydrophobic core segment of the **1** bilayer in a perpendicular orientation.

Tools for Biological Discovery and Detection

Imaging Domains in Membranes with Atomic Force and Fluorescence Microscopy

by A. R. Burns

Motivation—Lipid bilayer membranes in living systems have many critical functions in sensing and transport. Recently, it has been postulated that these functions occur within small domains of chemically or structurally distinct lipids that have undergone phase separation from the bulk membrane constituents. As schematically depicted in Fig. 1, these domains mediate the lateral organization required for complexes of transmembrane proteins and other membrane-associated proteins involved in membrane function. We are currently working on advanced imaging techniques to reveal the structure and properties of these domains in both intact biological and model membranes.

Accomplishment—Over the years, labeling of specific membrane lipids and proteins with fluorescent tags has enabled the use of optical imaging to visualize their location and to follow important dynamical processes such as diffusion. There are significant limitations, however, to fluorescence techniques. The small size (< 100 nm) of many membrane domains precludes lateral resolution with diffraction-limited optics (> 300 nm). Also, since it relies on specific fluorescent probes, optical imaging will not provide information with regard to the overall membrane landscape or topography. These limitations can be overcome by atomic force microscopy (AFM). We have shown that AFM has the ability to map topographic details of membrane organizational structure such as phase-separated lipid rafts and transmembrane proteins with 1 nm resolution. We are now able to perform *simultaneous* fluorescence and AFM imaging in order to provide full correlation of the location of fluorescently-tagged lipids or proteins with detailed membrane structure.

Simultaneous AFM and fluorescence images are shown in Fig. 2 for a model lipid bilayer supported on a glass substrate. The bilayer is a mixture of two lipids that have phase-separated into gel-like and liquid-like domains on the basis of structural differences in the long alkyl chains. As in Fig. 1, the gel-like lipids have straight chains (pink lipids), whereas the liquid-like lipids have bent chains (blue lipids). The straight chains result in densely-packed domains that are thicker or higher relative to the loosely-packed bent chains (AFM image in Fig. 2). A fluorescent probe lipid mixes with the liquid domains, but is excluded from the gel-like domain (fluorescence image in Fig. 2). Thus it verifies the identity of the lipids. These model bilayers are being used to determine the important chemical and physical factors that give rise to domain formation and probe partitioning. We are also working with the University of New Mexico Medical School on AFM/fluorescence imaging to map the location and follow the dynamic activity of specific membrane proteins involved in the immunological response of cells.

Significance—Mapping of membrane signaling pathways in biological systems is of great interest to the worldwide community. Knowledge of nanometer-scale lateral organization and its function in cellular membranes is required in the analysis of receptor-based signaling. Our unique imaging capabilities enable us to examine membrane structure and function with much greater detail than was previously possible since we are able to take advantage of both selective labeling and high topographic resolution.

Sponsors for various phases of this work include: DOE Office of Basic Energy Sciences and Laboratory Directed Research & Development

Contact: Alan R. Burns, Biomolecular Materials and Interfaces, Dept. 1141
Phone: (505) 844-9642, Fax: (505) 844-5470, E-mail: aburns@sandia.gov

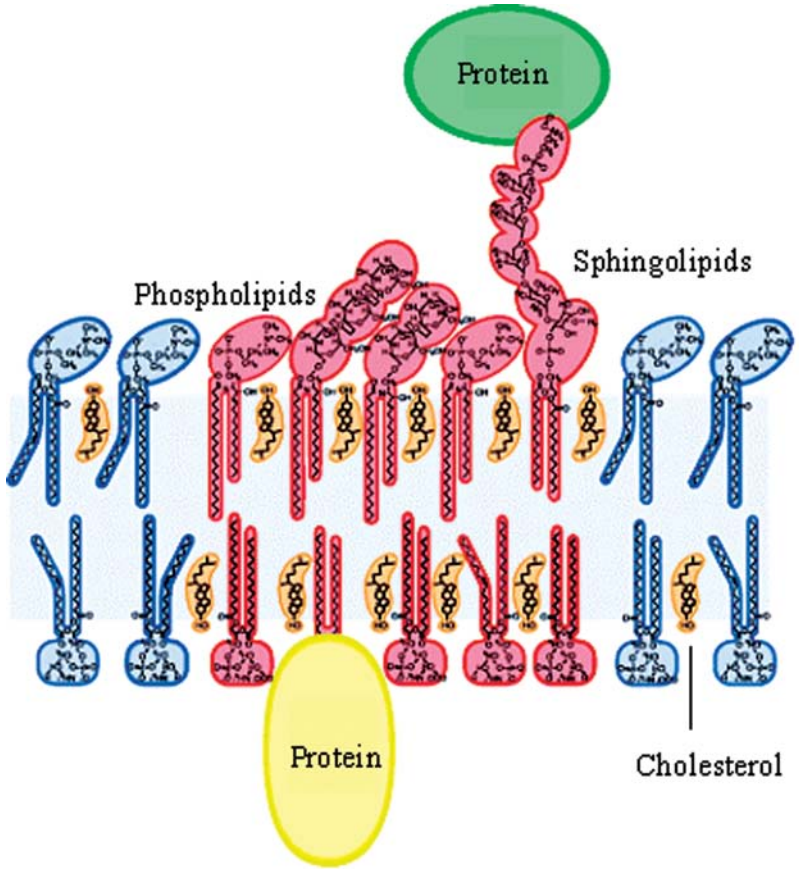

Figure 1. Membranes are organized by phase separations of phospholipids into liquid-like (blue) and gel-like (pink) domains. Proteins involved in cellular processes tend to associate with the gel-like domains or "rafts." Cholesterol molecules stabilize the rafts.

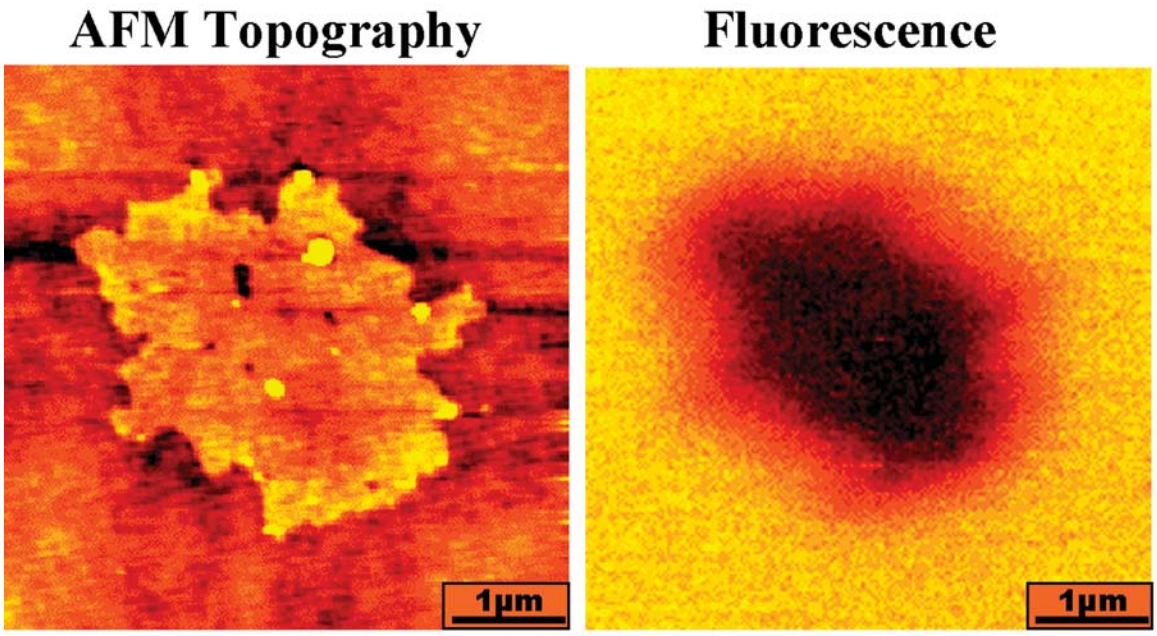

Figure 2. Simultaneous AFM topograph (left) and fluorescence (right) image of a gel-like lipid raft in a model membrane. The raft is 10 Å higher than the surrounding liquid phase. A fluorescent probe is excluded from the raft and thus the raft appears darker than the liquid phase. Scale bar = 1 µm.

Anthrax Detection in a Biocavity Laser

by ***Paul Gourley, Anthony McDonald, Judy Hendricks, Guild Copeland, and Keith Barrett***

Motivation—The anthrax bio-terrorism threat has become a reality. Innocent people have died by inhalation of anthrax spores sent via U. S. mail. A transduction method that could quickly detect anthrax spores would be a valuable tool in the fight against bio-terrorism. To this end, we devised a highly sensitive quantum optics transduction method using biocompatible laser microcavities to detect submicron pathogenic spores. The method uses recent advances in surface chemistry of semiconductor materials to create the microcavity.

Accomplishment—Anthrax spores and their simulants are very tiny particles, less than a micron in diameter, and nearly as small as the wavelength of light. Detection and analysis of these ultra-small particles requires new spectral-imaging techniques with high sensitivity. We used quantum squeezing of spontaneous light emitted through a spore flowing at high speed in a biocompatible semiconductor microcavity. This quantum squeezing allows even tiny spores to generate a whoppingly large spectral signal that can be easily detected. The spectral images (hyperspectra) are rapidly recorded and analyzed in a newly devised biolaser INCEPTOR (intracellular protein transduction by optical resonance) spectral imager/analyzer using efficient recognition software. This method extracts critical biological information from the lasing hyperspectra, including the protein coat morphology, intracellular granularity, spore shape and intracellular protein density and uniformity. The highly sensitive testing and differentiation of two common spore types, *B. subtilus* and *B. pumilus* that appear identical under the microscope, are shown in Fig. 1.

Significance—These data indicate that, with further development and testing, the biolaser INCEPTOR could rapidly identify different types of-anthrax spores, within a population of non-pathogenic spores. This analysis could be very useful for rapid, front-end screening of suspected pathogenic bacteria. The entire process, from set-up to diagnosis, could be completed in minutes. Such a field-deployable instrument is an attractive alternative to other, more time-consuming and labor-intensive DNA fragment analyses. Those analyses typically require restriction enzymes, PCR amplification, fluorescent tagging and cumbersome pulsed-field gel electrophoresis or specialized, expensive flow cytometry equipment. Further, the biolaser technique is compatible with immunofluorescence methods using molecular tags designed for anthrax antibodies. If intracavity surfaces are coated with an immunoassay antibody and the sample solution containing the conjugate antigen is flowed over the surface, the emitted light sensor will detect the interaction.

Sponsors for various phases of this work include: DOE Office of Basic Energy Sciences and Laboratory Directed Research & Development

Contact: Paul L. Gourley, Biomolecular Materials & Interfaces, Dept. 1141
Phone: (505) 844-5806, Fax: (505) 844-5470, E-mail: plgourl@sandia.gov

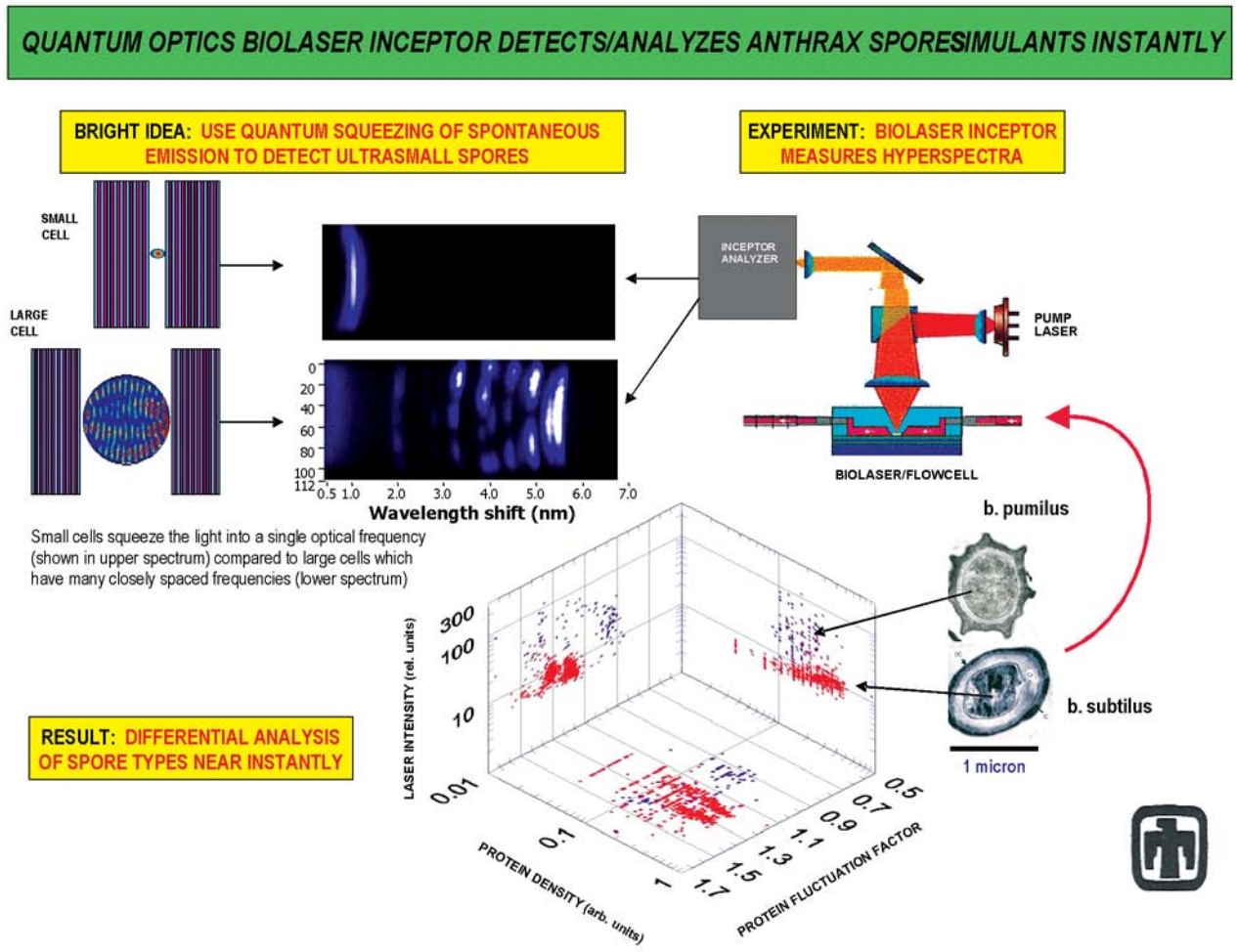

Figure 1. The upper left figure is an illustration of nano-squeezing of light through cells. The upper right figure represents an experiment for measuring spores. The lower figure is a measurement of spores showing different signatures for *b. pumilus* and *b. subtilus*.

Deep UV LEDs for Fluorescence-based Detection of Biological Agents

by A. J. Fischer, A. A. Allerman, M. H. Crawford, K. H. A. Bogart, S. R. Lee, R. J. Kaplar, W.W. Chow, and S. R. Kurtz

Motivation—Optical sources with emission from 280 - 340 nm are actively being sought for fluorescence-based detection of biological agents such as anthrax. Semiconductor sources emitting at these short wavelengths, although not currently available, would enable a new generation of light weight, low cost chem/bio detectors and hand-held detection systems. Although nitride-based emitters are currently the most promising candidates for emission below 300 nm, significant improvements in device output power and lifetime are still needed.

Accomplishment—LEDs with emission at 280 nm require the growth of AlGaN layers with Al concentrations of 50% or more. Compared to GaN, AlGaN layers grown on sapphire typically have higher densities of threading dislocations, lower mobilities, and lower n- and p-type doping levels. Although considerable progress has been made in the growth of AlGaN alloys, our LED epitaxial structure and device processing is designed to minimize the impact of these materials issues.

As shown in Fig. 1, our UV LEDs are designed with transparent base layers for improved light extraction. The n-AlGaN layer is grown as thick as stress will allow without cracking (1 mm) in order to improve lateral current spreading. The active region contains five 2.8 nm $Al_{0.36}Ga_{0.64}N$ quantum wells with $Al_{0.47}Ga_{0.53}N$ barrier layers. The p-side of the device includes a p-$Al_{0.47}Ga_{0.53}N$ layer that is graded down to a p-GaN contact layer. Although the p-GaN is absorbing below 370 nm, this layer has a much higher hole concentration than can be achieved with p-AlGaN, which results in better p-contacts and lower overall device voltage.

LED devices are fabricated using standard optical lithography to define features. Inductively-coupled plasma etching is used to expose the n-AlGaN for n-contact deposition. The top of the LED mesa is fully covered by the p-contact so that lateral transport through p-type material is not required. As shown in Fig. 2, interdigitated contacts are used to reduce the lateral current spreading distance in the n-AlGaN layer resulting in lower device voltages. LEDs are flip chip bonded to Si or SiC submounts which, in addition to improving light extraction, also helps with heat dissipation.

Electroluminescence spectra for an LED emitting at 295 nm are shown in Fig. 3. The defect emission at 330 nm, which is undesirable for fluorescence-based sensing, is 25 times weaker than the 295 nm emission (100 mA data). Further work is needed to eliminate this deep level contribution. As shown in Fig. 4, this 295 nm LED has an output power of 366 μW (CW) at 100 mA at 14.6 Volts, which is the highest power reported from a single device in this wavelength range. Recent effort towards shorter wavelengths has resulted in LEDs with emission as short as 275 nm.

Significance—LEDS with emission from 280 - 340 nm will enable handheld fluorescence-based chem/bio detectors with a low false alarm rate and excellent discrimination against common materials such as fuel fumes and exhaust. UV LEDs may also be used for nuclear materials detection, non-line-of-sight communication, as well as purification and sterilization applications.

Sponsors for various phases of this work include: Defense Advanced Research Projects Agency and Grand Challenge Laboratory Directed Research & Development

Contact: Arthur J. Fischer, Semiconductor Materials and Device Sciences, Dept. 1123
Phone: (505) 844-6543, Fax: (505) 844-3211, E-mail: ajfisch@sandia.gov

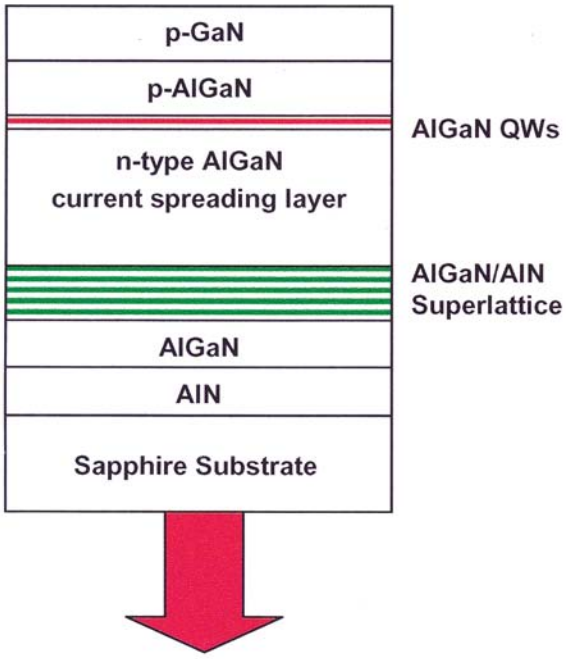

Figure 1. Schematic showing the structure used for the 295 nm LED. This bottom emitting structure utilizes transparent AlN and AlGaN base layers for improved light extraction through the sapphire substrate.

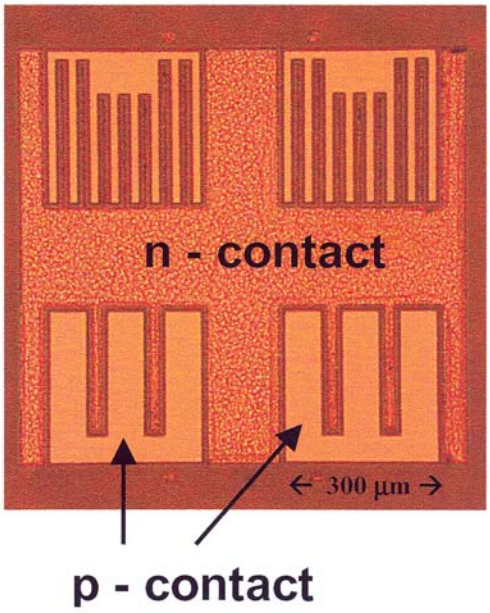

Figure 2. Optical microscope image showing two LED designs with interdigitated contacts. The thin fingers reduce the distance that current must spread through the n-AlGaN, which leads to reduced device voltages.

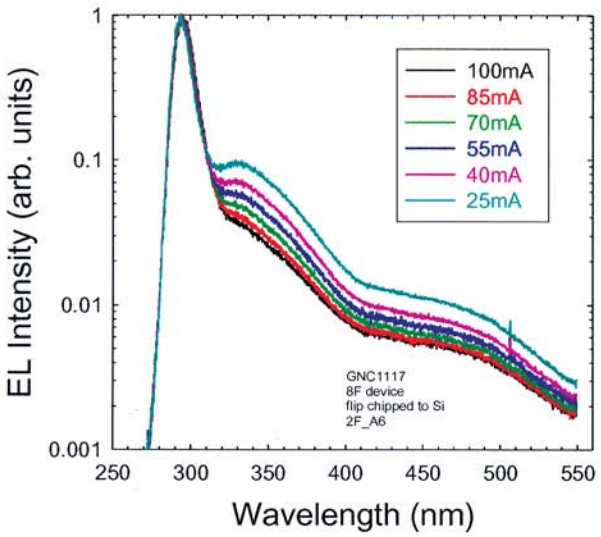

Figure 3. Normalized electroluminescence intensity showing emission at 295 nm. At 100 mA, the defect emission (330 nm) is 25 times weaker than the QW emission (295 nm).

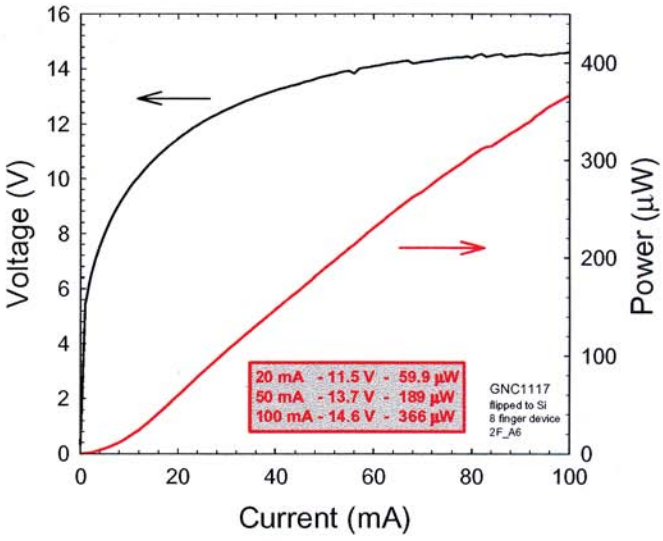

Figure 4. Light output power vs. current and current vs. voltage curves for a 295 nm LED. The maximum measured output power is 366 µW (100 mA, 14.6 V).

Understanding and Exploiting Complex and Collective Phenomena

Towards Programmable Self-Assembly in Biological and Artificial Systems

by A. M. Bouchard and G. C. Osbourn

Motivation—Dynamic self-assembly is a ubiquitous process in non-equilibrium physical and biological systems. Our research program pursues the theme that in such systems, dynamic self-assembly and computation are intimately related: that dynamic self-assembly can be used to perform computation, and that if the computational language can be understood, it can be used to program self-assembly. The first goal is to show that computation emerges in biological systems via self-assembly. This leads to two technological goals: (1) a novel self-assembling software technology modeled after biological computation, and (2) creating artificial systems (e.g., materials or circuits) that are programmed to dynamically self-assemble into desired hierarchical structures with the robustness of biological systems.

Accomplishment—We have built a common agent-based simulation infrastructure for use both in the self-assembling software and the stochastic simulations of self-assembling physical systems. Each agent embodies the properties of proteins that are required for self-assembly and computation-selective binding, which triggers actuation and the exposing or hiding of other binding sites.

We have implemented a variety of software self-assembly processes, including generating data structures, multiple kinds of executable code structures, dynamic execution pathways, hierarchies of software modules, movement of modules within the hierarchy and triggers that execute or inhibit certain code structures. We have also implemented a number of novel software constructs that are enabled by the self-assembly approach, such as the ability to override or monitor existing code externally, without modifying the original source code, recompiling, or terminating its execution.

As a first step toward developing programmed self-assembly in physical systems, we have demonstrated that selected idealized proteins can be designed to carry out computation. We find that stochastic versions of any deterministic Turing machine can in principle be obtained using dynamic self-assembly of proteins that exhibit commonly available properties. We also find that partial equilibration of the far-from-equilibrium stochastic protein networks intrinsically leads to increasing computational errors with length of computation, so that an ensemble of such computing networks diverges in configuration with time to different internal states and different computational results. This is a direct consequence of the stochastic nature of the protein networks and the second law of thermodynamics. (See figures.) This implies that if natural systems perform computations with low error rates, they must employ error-correction mechanisms as part of the algorithm.

Significance—These are our first results in the new Collective Hierarchical Systems technical thrust for Center 1100. This initial success suggests that programming complex self-assembly processes is, indeed, feasible. The next phase of this work will include: demonstrating error-correction schemes for the computational protein networks; developing an English-like language to autogenerate the self-assembling software; and developing simulations to guide experimentalists in harnessing cellular machinery (motor proteins and microtubules) to assemble novel materials.

Sponsors for various phases of this work include: DOE Office of Basic Energy Sciences and Laboratory Directed Research & Development

Contact: Ann M. Bouchard; Lasers, Optics, & Remote Sensing; Dept. 1118
Phone: (505) 845-0552, Fax: (505) 844-5459, E-mail: bouchar@sandia.gov

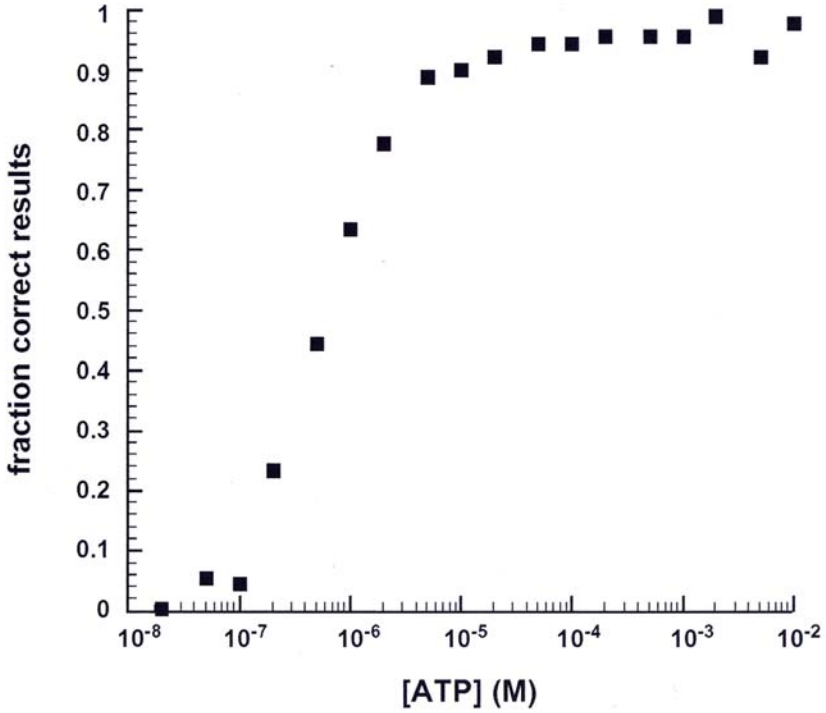

Figure 1. We implemented simulations of computing (a*b)+(c*d)+(e*f) using an ATP-driven dynamic stochastic protein network. The fraction of correct final results as a function of ATP concentration is shown. These results make clear that the dynamic, non-equilibrium behavior of these protein networks is driven by the free energy of the ATP population.

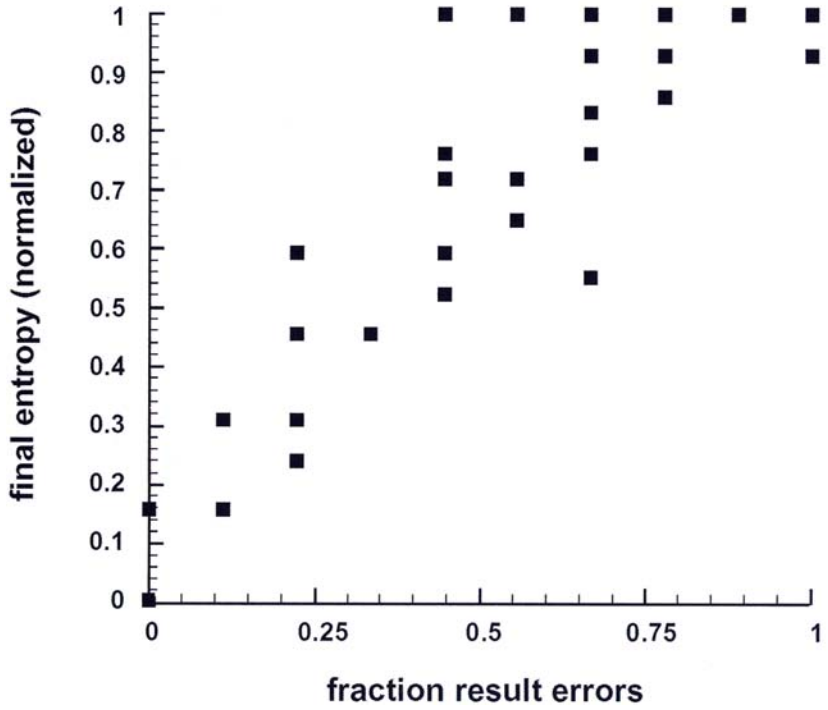

Figure 2. A scatter plot of final entropy as a function of errors for the computation described in Fig. 1. These results show that ending in a more highly ordered state is clearly correlated with high yields of correct computational results, so that maintaining far-from-equilibrium configurations is the desired outcome for these protein networks. The entropy captures all configurational differences, including those that do not disrupt the final register values, and this produces the scatter in the plot.

Binding Mechanisms in Plasma Crystals

by G. A. Hebner, M. E. Riley, E. V. Barnat and G. Axford

Motivation—Plasma crystals are formed when particles in an electrical plasma self-assemble into orderly arrangements due to long range and collective interactions. Scientific interest is high not only because of applications to astronomy and the semiconductor industry but also because the crystals serve as a macroscopic platform on which to develop and test theories of collective interactions in many-body assemblies and long range particle interactions. Examples include wave propagation in ionic solids, phase transitions in Coulomb and shielded-Coulomb crystals, lattice stability dynamics of crystallization, charging mechanisms within plasmas, and the physics of the surrounding plasma and sheaths. For this program, we are combining experimental and theoretical studies to develop a mature understanding of the fundamental long-range interactions and multi-particle dynamic behavior of macroion crystals.

Accomplishment—We have measured both the magnitude and shape of the attractive interaction between two negatively charged particles immersed in a charge neutral plasma. While our previous work demonstrated that the dominant force between particles in a stable 2D planar plasma crystal is repulsive, 3D particle assemblies include an attractive interaction that strongly influences the lattice kinetics. The attractive interaction originates from the positive space charge region produced by the focused flow of positive ions around the negatively charged particles. Our measurements are the first to map the entire 3D attractive binding potential and show that the structure of 3D assemblies is due to a delicate balance between repulsive Coulomb interactions and attractive forces.

To characterize the attractive interaction, we developed a new technique to determine the forces present during very low energy head-on particle collisions. By manipulating the electric fields within the plasma using a parabolic, grooved electrode (Fig. 1), a well-defined potential trough is formed. An analysis of the particle trajectories as a function of time yields the time dependent attractive and repulsive forces on the particles. Figure 2 shows an example of the radially dependent attractive force at one distance below the particle, a fit to the functional form predicted by our first principles model, and the attractive binding potential. For this case, the peak force was on the order of 60 fN (femtonewtons), comparable to the forces applied by laser tweezers. By changing the probe particle mass, we measure the force at a range of distances below the upper particle and integrate the force maps to generate a spatial map of the binding potential (Fig. 3).

Significance—Our measurement of the magnitude and shape of the attractive binding potential provides detailed new information about the forces that control the structure and dynamics of 3D, charged particle assemblies. While our measurements show the same trends as published calculations, current codes include a number of simplifying assumptions that must be addressed to improve agreement. In addition to applications to dusty plasmas, these measurements address longstanding and fundamental questions related to the structure of the plasma sheath in the presence of a flowing ion wind. Such sheaths are found in common plasma applications such as lighting, surface cleaning, flat panel displays, and semiconductor processing.

Sponsors for various phases of this work include: DOE Office of Basic Energy Sciences and Nuclear Weapons/Science & Technology

Contact: Greg Hebner; Laser, Optics, and Plasma Sciences; Dept. 1118
Phone: (505) 844-6831, Fax: (505) 844-5459, E-mail: gahebne@sandia.gov
Additional information at: http://www.sandia.gov/1100/X1118pchome.htm

Figure 1. Side view of the lower electrode assembly and the Argon plasma glow. The arrow is pointing to the slot in the lower electrode that produces the electrostatic trough in which the particles collide.

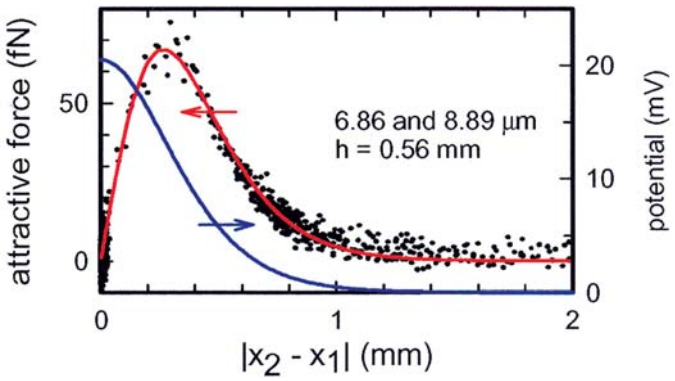

Figure 2. Measured attractive force (dots) that binds two negatively charged particles. The red curve is a fit to the data using a form predicted by our models and the blue curve is the binding potential obtained by integrating the force.

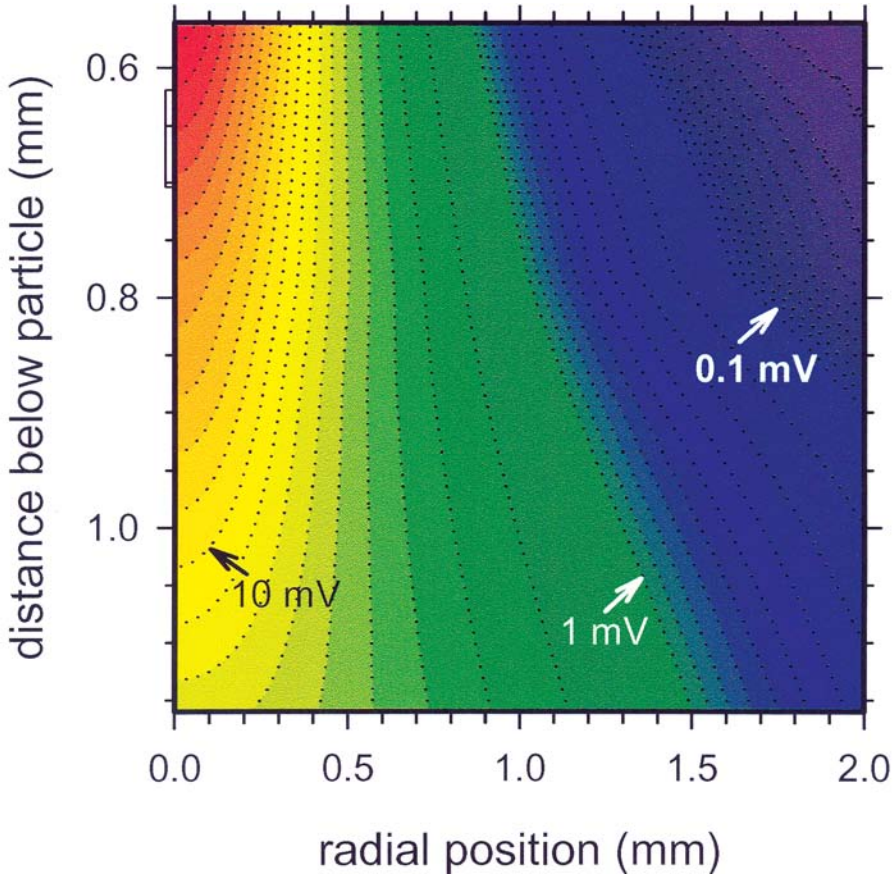

Figure 3. Measured binding potential (mV) as a function of the distance below the particle and the radial position. The 6.86 μm diameter particle is located at (0,0) and has a charge of 6000 electrons.

Giant Magnetostriction of Field-Structured Composites

by James E. Martin, Robert A. Anderson and Gerald Gulley

Motivation—There is a need for soft actuators that have a much larger strain response than piezoelectrics and that can respond in microseconds. Applications include artificial muscles for robots, and strain sensors based on permeability changes (an inverse effect). To meet these needs we have begun to investigate Magnetostrictive Elastomers, polymer/particle composites that contract in a uniform magnetic field. This experimental research is motivated by a recent theoretical paper [J. E. Martin and R. A. Anderson, J. Chem. Phys. 111, 4273 (1999)] that shows that using magnetic fields to structure magnetic particles into chains should significantly enhance the observed contraction, due to the strong dependence of the magnetic permeability of such field-structured composites (FSCs) on tensile strain.

Accomplishment—We have built an optical cantilever apparatus, Fig. 1, capable of measuring field-induced sample strains as small as 1 ppm. With this apparatus it is possible to apply a preload (a tensile stress) to the sample, and the sample geometry is designed to minimize the opposing effect of the demagnetization field. In accord with theory, structuring particles into chains greatly increases magnetostriction, Fig. 1, the observed increase being even larger than the factor of three predicted. In a saturating magnetic field the FSCs we have developed are capable of magnetic strains of 10,000 ppm, five times larger than Terfenol D at room temperature, the highest-performing homogeneous material. But these materials also show a puzzling increase of the magnetic strain with sample preload, Fig. 2, in contrast to the monotonic decrease expected. To understand this effect, we have completed an analysis of a single chain of particles embedded in an elastic gel that shows that a hierarchy of structural phase transitions occurs, Fig. 2, that reduce magnetostriction from that expected with strictly affine deformation of the composite. The critical field at which this clustering transition occurs depends strongly on the sample preload and gel modulus. A full scale simulation of this transition is now in progress for physically reasonable models of FSCs, and we hope that this might explain the anomalous dependence of magnetostriction on sample preload.

Significance—We have demonstrated that giant magnetostriction, far exceeding that possible with Terfenol D, is indeed possible in particle/polymer composites structured by magnetic fields. These investigations have led to the discovery that this effect is enhanced by preloading the sample, which has led us to postulate that a novel structural phase transition occurs in these materials. This transition reduces the dependence of the permeability on strain, which decreases magnetostriction. The effect is largest at small preload, in accord with the experimental data, but whether this transition is the primary cause of the preload effect is the object of current theoretical and simulation studies.

Sponsors for various phases of this work include: Laboratory Directed Research & Development and DOE Office of Basic Energy Sciences

Contact: James E. Martin, Nanostructures and Advanced Materials Chemistry, Dept. 1122
Phone: (505) 844-9125, Fax: (505) 844-4045, E-mail: jmartin@sandia.gov

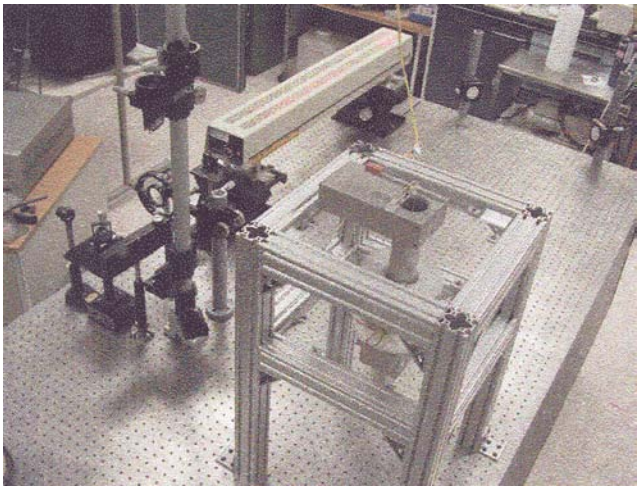

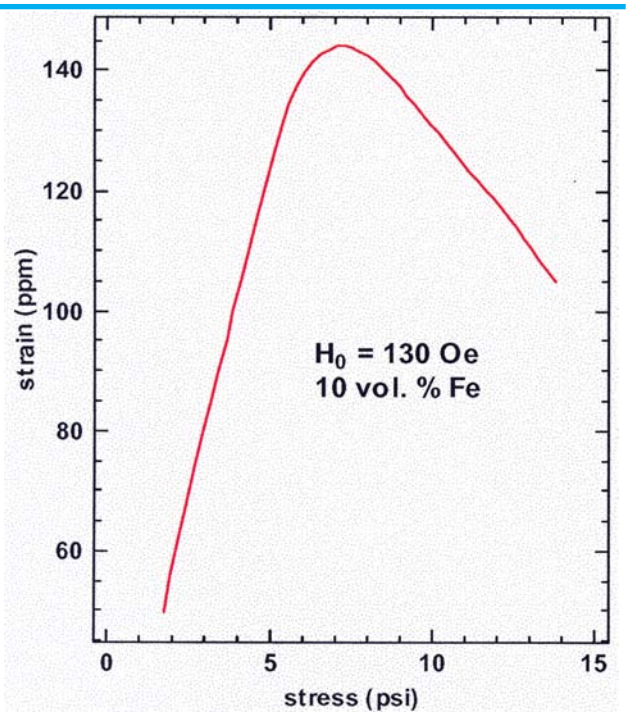

Figure 1. (left) Optical cantilever apparatus. (right) Magnetostriction is larger in FSCs than in random composites. Composites were 10 vol.% Fe in a silicone elastomer, and had a 11.6 psi preload.

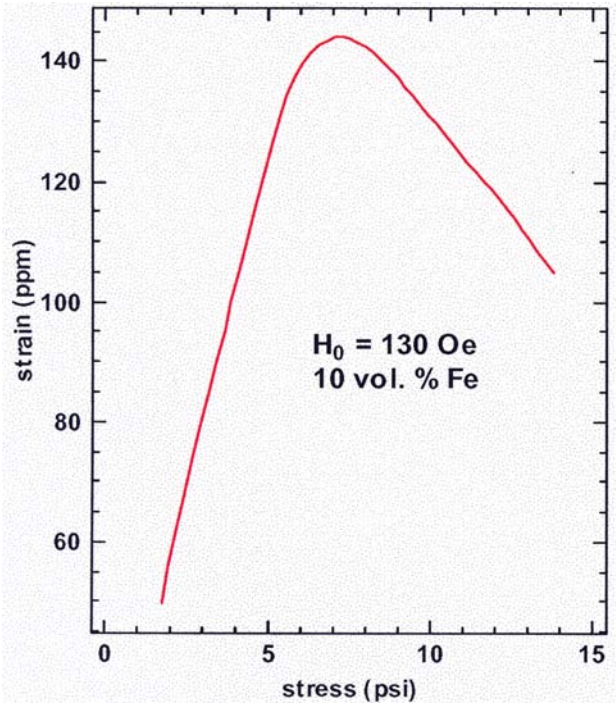

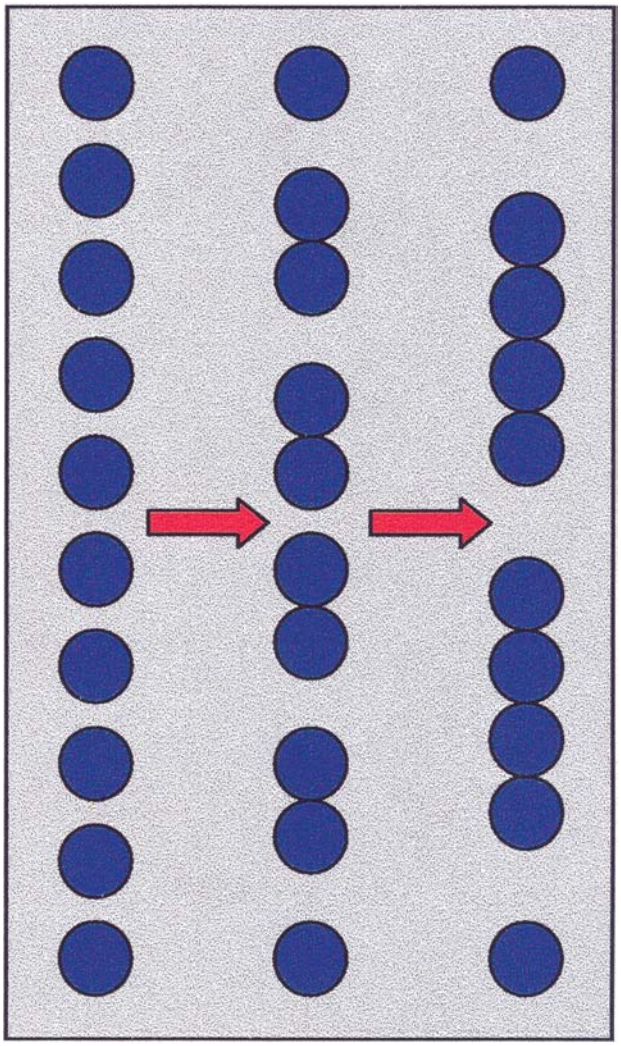

Figure 2. (left) Magnetostriction depends strongly on the sample prestress, actually increasing initially. (right) A chain of particles shows a hierarchy of phase transitions with increasing field.

Recent Awards and Prizes

Recent Awards and Prizes

National and International Awards

2002 — **Plasma Prize for Science and Technology** presented by the American Vacuum Society, Plasma Science and Technology Division, for innovative development of diagnostics and insightful fundamental studies of low temperature plasmas and their successful application to the advancement of plasma technologies. (Greg Hebner)

— **National Academy of Engineering:** Elected for originating the field of strained-layer superlattices and related structures, which has led to revolutionary advances in electronics and optoelectronics." (Gordon Osbourn)

2000 — **IEEE Third Millennium Medal** for Outstanding Achievements and Contributions (Paul V. Dressendorfer)

— **R&D 100 Award** for the Ion Electron Emission Microscope (IEEM) [Barney Doyle, George Vizkelethy, Robert Weller (Vanderbilt University), and Berthold Senftinger (Staib Instruments, Inc., Germany)]

DOE Basic Energy Sciences, Material Science Awards

2002 — **BES "Chunky Bullet Shootout":** Winner for "Ultrasensitive Chemical Sensors for Counter Terrorism Applications." (Jim Martin and Bob Anderson)

2000 — **DOE Energy@23 Award** (top 23 DOE innovations from 1977-2000 contributing to American consumers) for the Strained-Layer Semiconductor. (Gordon Osbourn)

— **Energy 100 Awards** (top one hundred discoveries and innovations from the Department of Energy that have resulted in improvements for American consumers from 1977-2000) for the Biological Microcavity Laser. (Paul Gourley)

Other Awards

2003 — **AAAS Fellow Appointment:** Elected Fellow of the American Association for the Advancement of Science (AAAS) for his "research advances, particularly the development and exploitation of interfacial force microscopy, leading to fundamental understanding of the interaction of solid surfaces with the environment." (Jack Houston)

— **Humboldt Research Award** for early experimental research on electrical discharge excimer lasers and for recent accomplishments on the microscopic theory of semiconductor lasers. (Weng Chow)

— **National Associate of the National Academies** (NAS, NAE, Institute of Medicine, NRC): Awarded for recognition of her "extraordinary service to the National Academies." (Julia Phillips)

— **Nellie Yeoh Whetten Award** from the AVS Science and Technology Society for recognition of excellence in graduate research by a woman in a scientific or technical area of interest to the AVS. (Meredith Anderson)

2002 — **AAAS Fellow Appointment:** Elected Fellow of the American Association for the Advancement of Science (AAAS) for her "seminal research on growth and properties of magnetic, superconducting, and optical thin films and for leadership in the management of interdisciplinary research." (Julia Phillips)

— **APS Fellow Appointments:** Elected Fellows of the American Physical Society (APS) for:

— contributions to the fundamental understanding of the gas-phase and surface chemical processes in the chemical vapor deposition of semiconductor materials. (Michael E. Coltrin)

— outstanding contributions to the physics of tunneling in two dimensional electronic materials, including fractional quantum Hall and double quantum well systems. (Jerry A. Simmons)

— pioneering studies of atomic-scale, kinetic, and thermodynamic aspects of the morphology of Si surfaces and significant innovations in scanning tunneling microscopy. (Brian S. Swartzentruber)

— **Federal Laboratory Consortium (FLC) Excellence in Technology Transfer Award** for the development of instrumentation and software analysis to measure, *in situ*, thin film growth rates and wafer temperature during the fabrication of compound semiconductor optoelectronic device structures. (Bill Breiland)

— **Horizon Award** presented by the New Mexico Commission on the Status of Women and the U. S. Department of Labor Women's Bureau: The recipient of this award must be a New Mexico resident who has contributed significantly to the acceptance and advancement of women in Science, Math, Engineering, and Technology. (Julia Phillips)

— **Humboldt Research Award** in recognition of research accomplishments in the area of polymer modeling, which will be used to further collaborations with colleagues in Germany. (Gary Grest)

— **Publication in "All Star" collection** of 25 significant and most cited articles that appeared in ECS journals since 1940. (M. E. Coltrin, R. J. Kee, and J. A. Miller)

— **Sandia Fellow Appointment:** By distinguishing himself and Sandia through his technical novations in several very important fields, including strained-layer technology, the application of biological vision and pattern recognition systems to computer-based sensor systems, and collective intelligence and self-organizing systems. (Gordon Osbourn)

— **Weapon Award of Excellence**: The CY 2001 Weapons Award of Excellence winners included two teams at Sandia Laboratories led by Center 1100:

— (1) The Neutron Tube Production R&D Team for applying scientific tools and methods to improve yield and reliability of Neutron Tubes. (Paul A. Miller, Team Lead, et al.)

— (2) The Photonic Driver Team for developing a Photonic Driver capability for microscale shock wave physics research. (Bob Setchell, Team Lead, et al.)

2001 — **APS Fellow Appointment:** Elected Fellow of the American Physical Society (APS) for pioneering work in applying scanning probe microscopy techniques to elucidate the nanometer scale electronic and optical properties of novel materials, in particular the physics related to defect. (Julia Hsu)

— **The Lockheed Martin NOVA Award:** The NOVA Awards honored a Sandia/industry team that developed the first 1.3-micron electrically pumped vertical cavity surface emitting laser (VCSEL). (John Klem, Andy Allerman, Kent Choquette, et al.)

2000 — **APS Fellow Appointment:** Elected Fellow of the American Physical Society (APS) for the invention of numerous Micro-Ion Beam Analysis techniques and their innovative application to solid state physics, fusion energy, materials science and radiation effects of semiconductors. (Barney Doyle)

Patents Awarded

2003

— Patent 6,627,048
Title: Reductive Precipitation of Metals Photosensitized by Tin and Antimony Porphyrins
Originator: John A. Shelnutt

— Patent 6,406,931
Title: Conductivity Control of GaN Using LT AIN Buffer Layers
Originators: Jeffrey J. Figiel, Jung Han (Yale University)

— Patent 6,599,362
Title: Substrate Texturing for Cantilever Epitaxy of III-N and Other Materials
Originators: Carol I. Ashby, Christine C. Mitchell, David M. Follstaedt, Jung Han (Yale University)

— Patent 6,552,338
Title: Ion Photon Emission Microscope
Originators: Barney L. Doyle

— Patent 6,567,454
Title: Coupled-resonator Vertical-cavity Lasers with Two Active Gain Regions
Originators: Arthur J. Fischer, Weng W. Chow, Kent D. Choquette

— Patent 6,479,919
Title: Solid-state Nuclear-to-electric Energy Conversion: Beta-voltaic Cells of Icosahedral Borides
Originators: Terrence L. Aselage, David Jacob Emin

— Patent 6,570,333
Title: A Method for Generation of Surface Plasma Using Radio-frequency Power Across Pairs of Insulator Conductors where the Plasma Can Cover a Variety of Flat or Curved Surfaces, such as Aircraft Surfaces in High-altitude Flight Operation
Originators: Paul A. Miller, Ben P. Aragon

— Patent 6,600,761
Title: Semiconductor Laser with Multiple Lasing Wavelengths
Originators: Arthur J. Fischer, Weng W. Chow, Kent D. Choquette

— Patent 6,608,846
Title: Bistable Laser with Multiple Coupled Active Verticle-Cavity Resonators
Originators: Arthur J. Fischer, Weng W. Chow, Kent D. Choquette

2002
— Patent 6,304,675
Title: A New Cluster Analysis Method
Originators: Gordon C. Osbourn, Rubel F. Martinez
— Patent 6,393,038
Title: Frequency-doubled Vertical External Cavity Surface Emitting Laser
Originators: William J. Alford, Mary H. Crawford, Andrew A. Allerman, Thomas D. Raymond
— Patent 6,375,759
Title: Batch Fabrication of Precision Miniature Permanent Magnets
Originators: Terry J. Garino, Eugene L. Venturini, Todd R. Christenson
— Patent 6,391,393
Title: Nonvolatile, Dual Level, Magnetic Storage Media
Originators: James E. Martin, Chris P. Tigges, Robert A. Anderson, Eugene L. Venturini
— Patent 6,368,775
Title: 3-D Photo-Patterning of Refractive Index Structures in Photosensitive Thin Films
Originators: Barrett G. Potter, Jr.; Kelly Simmons Potter
— Patent 6,406,931
Title: Conductivity Control of GaN Using LT AIN Buffer Layers
Originators: Jeffrey J. Figiel, Jung Han
— Patent 6,365,428
Title: Buried Distributed Bragg Reflector for Planar Waveguide Applications
Originators: Walter J. Zubrzycki, Gregory A. Vawter, Andrew A. Allerman

2001
— Patent 6,288,394
Title: Highly Charged Ion Based Time of Flight Emission Microscope
Originators: Barney L. Doyle, LLNL Team
— Patent 6,291,823
Title: Ion Induced Electron Emission Microscopy
Originators: Barney L. Doyle, Gyorgy Vizkelethy, Robert A. Weller (Vanderbilt Univiversity)
— Patent 6,258,615
Title: Multiple Wavelength Vertical Cavity Resonance Devices Fabricated by Selective Area Epitaxy in MOVPE
Originators: Michael E. Coltrin, Hong Q. Hou, Kent D. Choquette
— Patent 6,187,592
Title: Method for Determining Hemoglobin Concentration in Individual Red Blood Cells
Originator: Paul L. Gourley

— Patent 6,245,200
Title: Visible Light Photooxidation of Toxic Organic Chemicals Using Nanoscale MoS2
Originator: Jess P. Wilcoxon
— Patent 6,252,287
Title: Heterojunction InGaAsN Solar Cells
Originators: Steven R. Kurtz, Eric Daniel Jones, Andrew A. Allerman, John F. Klem
— Patent 6,194,769
Title: Sensor Devices Based on Field-structured Composites
Originators: Robert C. Hughes, James E. Martin, Robert A. Anderson
— Patent 6,248,992
Title: Tailored Doping Profile for Photoconductive Semiconductor Switch
Originators: Guillermo M. Loubriel, Darwin James Brown, Fred J. Zutavern, Wesley D. Helgeson, Martin W. O'Malley, Gary J. Denison, Charles T. Sullivan, Hong Q. Hou, Albert G. Baca, Thomas E. Zipperian, Andrew A. Allerman, Harold P. Hjalmarson
— Patent 6,290,868
Title: Field-structured Chemical Sensor
Originators: Robert C. Hughes, James E. Martin, Robert A. Anderson

2000
— Patent 6,147,793
Title: Short-Cavity, Pulsed Optical Parametric Oscillators
Originators: Arlee V. Smith, William J. Alford
— Patent 6,110,390
Title: A Double Electron Layer Tunneling Transistor (DELTT)
Originators: Timothy J. Drummond, Marc E. Sherwin, Jerry A. Simmons
— Patent 6,035,246
Title: Chemical Recognition Software
Originators: John S. Wagner, Gary C. Tisone, Philip J. Hargis, Jr.
— Patent 6,048,546
Title: Lipid Bilayer Entrapment in Sol-gel Materials
Originators: Douglas A. Loy, Darryl Y. Sasaki, Stacey A. Yamanaka
— Patent 6,103,305
Title: Zero Stress Amorphous Diamond
Originators: Thomas A. Friedmann, John P. Sullivan
— Patent 6,057,377
Title: Molecular Receptors in Functionalized Sol-gel Materials Generated through Molecular Imprinting
Originators: Carol S. Ashley, C. Jeffrey Brinker, Darryl Y. Sasaki
— Patent 6,022,748
Title: Immobilization of Colorimetric Liposomes into Sol-gel Matrices for Direct Colormetric Detection
Originators: Darryl Y. Sasaki, Stacey A. Yamanaka

— Patent 6,085,581
Title: Three-dimensional Two-location Positioner with Reverse Referencing
Originators: Gary D. Jones, Jack E. Houston, Kenneth T. Gillen
— Patent 6,071,109
Title: The Preparation of AllnSb by Metal-Organic Chemical Vapor Deposition
Originators: Kevin C. Baucom, Robert M. Biefeld, Andrew A. Allerman
— Patent 6,117,369
Title: Improved Molecular Optical Switch Based on Nickel Porphyrins
Originator: John A. Shelnutt
— Patent 6,083,360
Title: Use of Supplemental Heating for Deposition Tooling Shields
Originators: John A. Hunter, Diane E. Peebles, James A. Ohlhausen, Kenneth Hall Eckelmeyer

Government Advisory Boards and Professional Societies/International Committees/Journals

Government Advisory Boards

Argonne National Laboratory

— Materials Science Division External Review Committee: Julia Phillips, member, 1995-2000; Chair, 2003

Lawrence Berkeley National Labs (LBNL) Committee

— Accelerator and Fusion Research/Directors Review Committee; Barney Doyle, member; 2003

National Institute of Biomedical Imaging and Bioengineering (NIBIB)

— National Institutes of Health (NIH) Study Panel; Alan Burns, Special Emphasis Panel member; 2003

National Research Council

— Committee on Nanotechnology for the Intelligence Community; Wil Gauster, member, 2003-2004
— National Materials Advisory Board: Julia Phillips, member, 1999-2001; Chair, 2002-2004
— Board on Physics and Astronomy; Julia Phillips, member; 2000-2006
— National Academy of Engineering, Symposium on Frontiers of Engineering; Julia Hsu, participant; 2003
— U.S. Liaison Committee for the International Union of Pure and Applied Physics; Julia Phillips, member; 2000-2002
— Committee on Materials Research for the Defense-After-Next; Julia Phillips, member; 1999-2002
— National Academy of Sciences, Symposium on Frontiers of Science; Julia Hsu, participant; 2001
— Solid State Sciences Committee; Julia Phillips, Vice Chair; 1998-2001

National Science Foundation

— Advisory Committee, Mathematics and Physical Sciences Directorate; Julia Phillips, member; 2000-2003

Professional Societies/International Committees/Journals

American Association for the Advancement of Science

— Council; Julia Phillips, member; 2003-2005
— Physics Section Nominating Committee; Julia Phillips, member; 2003-2005
— Physics Section; Julia Phillips: Chair-elect, Chair, Past Chair; 2003-2005

American Association for Crystal Growth

— 15th American Conference on Crystal Growth and Epitaxy; Bob Biefeld, Co-chair; 2002

American Physical Society

— Committee on Meetings; Mark Lee, member; 2003-2006
— Maria Goeppert Mayer Award Committee: Julia Phillips, member, 2001; Chair, 2002
— APS Division of Materials Physics (DMP) Executive Committee; Julia Phillips, Member at Large; 1997-2000

American Vacuum Society

— AVS Board of Directors; Neal Shinn, member; 2003-2006

Professional Societies/International Committees/Journals (continued)

— AVS 39th Annual Meeting of the New Mexico Chapter; Kate Bogart, Symposium Chair; 2003
— AVS Chapters, Divisions, Groups Committee; Neal Shinn, member; 2002-2004
— AVS Surface Science Division; Neal Shinn, Chair; 2001-2002
— AVS Surface Science Division; Neal Shinn, Program Chair; 2000

Army Research Office (ARO) Multi University Research Initiative (MURI)
— Technical Advisory Committee; Mark Lee, member; 2001-2002

BES Materials Council
— Workshop on Issues in Nanomechanics; Charles Barbour, Panel Chair; 2003

Gaseous Electronics Conference (GEC)
— 56th Annual Meeting; Greg Hebner: Chair-elect, Chair, Past Chair; 2003-2006

Institute of Electrical and Electronics Engineers
— IEEE Nuclear and Plasma Sciences Society (NPSS); Paul Dressendorfer, Editor-in-Chief; 2002-present
— IEEE NPSS Radiation Instrumentation Steering Committee; Paul Dressendorfer, member; 1997-present
— IEEE Nuclear and Plasma Science Society (NPSS) Administrative Committee; Paul Dressendorfer, member; 1993-present
— IEEE Transactions on Nuclear Science; Paul Dressendorfer, Editor; 1993-present
— IEEE NPSS Radiation Effects Steering Group (RESG); Paul Dressendorfer, member; 1988-present

International Conference on Ion Beam Analysis
— Gyorgy Vizkelethy and Barney L. Doyle, Chairmen; 2003
— International Committee; Gyorgy Vizkelethy and Barney L. Doyle, members; 2003

International Conference on Nuclear Microscopy Technology and Applications
— International Committee, Barney L. Doyle; 1990-2004

International Journal of PIXE (IJPIXE)
— Editorial Board, Barney Doyle; 1996-present

International Union for Vacuum Science, Technique, and Applications (IUVSTA)
— IUVSTA Surface Science Electoral College; Neal Shinn, United States Representative; 2001-2004
— IUVSTA Surface Science Division; Neal Shinn, Secretary; 2001-2004
— Surface Science Program, 15th International Vacuum Congress; Neal Shinn, Surface Science Chair; 2001
— Surface Science Program, 16th International Vacuum Congress; Neal Shinn, member; 2004

Professional Societies/International Committees/Journals (continued)

Industrial and Professional Advisory Council for the Engineering Science and Mechanics Department at Penn State University
— Neal Shinn, member; 2003-2006
— Wil Gauster, member; 2001-2004

Ion Beam Modification of Materials Conference
— International Committee; Charles Barbour, member; 1996-present

Journal of Chemical Physics
— Jim Martin, Editorial Board; 2003-2006

Journal of Vacuum Science and Technology
— Neal Shinn, Associate Editor; 2002-present

Materials Research Society
— MRS Meetings: Julia Hsu, Chair, Fall 2004; Jerry Floro, Chair, 2001
— MRS Board of Directors; Jerry Floro, member; 2002-2004
— MRS Task Force on Meeting Program/Board of Directors Interactions; Julia Phillips, Chair; 2003
— MRS Task Force on Government Agencies Committee; Charles Barbour, member; 2002
— MRS Symposium: Sean Hearne, Organizer, Fall 2002; Tom Friedmann, Organizer, 2001; Alan Wright, Organizer, Fall 2001; Eric Jones, Organizer, 2000
— MRS Membership Committee; Charles Barbour, Chairman; 2001-present
— MRS Task Force 2020 Committee; Charles Barbour, member; 2000

Materials Sciences and Engineering Programs in the Office of Basic Energy Sciences
— Committee of Visitors (COV); Julia Phillips, member; 2003

NASA Review Panel
— Robert Biefeld, member; 2002

Nuclear Instruments and Methods in Physics Research, Section B: Beam Interactions with Materials and Atoms
— Barney Doyle, Editorial Board; 2003-2006

Optical Society of America
— OSA-Committees for 2000 Awards; Arlee Smith, Max Born Award Member; 2000

Radiation Effects in Insulators Conference
— Charles Barbour, International Committee member; 1997-present

Physical Review E
— Gary Grest, Senior Editor; 2002-present

Professional Societies/International Committees/Journals (continued)

The Minerals, Metals, and Materials Society (TMS)
— Electronic Materials Committee; Julia Hsu, member; 2000-2006
— Electronic Materials Committee: Bob Biefeld, member, 2002-present; Secretary, 2002-2004

Twelfth International Conference on Metal-Organic Vapour Phase Epitaxy
— Bob Biefeld, Organizing Committee member; 2002

US-Organometallic Vapor Phase Epitaxy Workshop
— Bob Biefeld, Organizing Committee member; 2002

Resources and Capabilities

Resources and Capabilities
Physical and Chemical Sciences Center

— Diagnostics and Characterization —

Atomic-Level Imaging and Spectroscopy

We have developed technical capabilities in:

- Scanning Tunneling Microscopy (STM) with the ability to track the diffusion of single atoms on surfaces,
- Low Energy Electron Microscopy (LEEM) with nanometer spatial resolution and real-time spectroscopic imaging capability at sample temperatures from 300K to over 1000K,
- Field Ion Microscopy (FIM) with single atom resolution and accurate temperature control to 1 Kelvin,
- Atom Probe Microscopy (APM) with pulsed laser desorption capability,
- Interfacial Force Microscopy (IFM) with feedback for accurate, simultaneous normal and frictional force profile measurements for the quantitative study of adhesion, tribology, and nanomechanics, and
- Atomic force microscopy (AFM) for imaging, force profiling, and manipulation of individual biomolecules in fluid environments with simultaneous fluorescence detection.

Scanning Probe Metrology

We have developed a unique wide-field scanning Interfacial Force Microscope with calibrated force detection for the dynamic measurement of normal and lateral forces of micro-electrical-mechanical system components in operation.

Simultaneous Measurement of H, D, and T in Materials

We have designed and implemented a new ion beam analysis (IBA) system to simultaneously measure the absolute quantities of H, D, and T in materials using an elastic recoil detection (ERD) technique. The technique uses an E-dE detector arrangement, or particle telescope, to provide for accurate separation of the H, D, and T signals. The system can also simultaneously acquire information about medium and high Z elements in the sample using Rutherford backscattering spectrometry (RBS). Measurement of other light elements is possible using the nuclear reaction analysis (NRA) technique, which is isotope specific. The system will have an accuracy of < 2% for measuring the composition of solids.

Ion Accelerator Nuclear Microprobe

We have facilities for nuclear microscopy and radiation effects microscopy based on a 6 MV tandem Van de Graaff ion accelerator. We generate ion species from hydrogen to gold for both radiation effects research and quantitative high-energy ion beam analysis of materials containing light elements (hydrogen to fluorine) using heavy ion elastic recoil detection (ERD) and heavy elements using high-energy backscattering spectrometry, and Heavy Ion Backscattering (HIBS). (Includes Patent #5,059,785 issued October, 1991.) An external Micro Ion Beam Analysis (X-MIBA) capability enables multi-elemental analysis and ion irradiation of samples, which are vacuum incompatible or extraordinarily large. The Sandia Nuclear Microprobe with micrometer size high-energy ion beams is used to study materials and devices. Special emphasis is given to the evaluation of the radiation hardness of microelectronic devices using three new advanced diagnostic techniques invented at Sandia: Single-Event-Upset Imaging, Ion-Beam-Induced-Charge-Collection Imaging (IBICC), and time-resolved IBICC. A recent development is the Ion Electron Emission Microscope (U. S. Patent No. 6,291,823 and 2001 R & D-100 Award winner), which can perform radiation microscopy using very highly ionizing particles without focusing the ion beam.

Materials Microcharacterization

Our capabilities in this area include optical microscopy, scanning, electron microscopy, analytical transmission electron microscopy, double crystal x-ray diffraction, ion beam analysis of materials (RBS, channeling, ERD, PIXE, NRA), Hall measurements, microcalorimetry, photoluminescence, light scattering, electronic transport, deep level spectroscopy, magnetization, and dielectric and magnetic susceptibilities.

Surface and Interface Spectroscopies

We maintain capabilities in Auger electron spectroscopy (AES), x-ray photoelectron spectroscopy (XPS), low energy electron diffraction (LEED), thermal desorption spectroscopy (TDS), and infrared reflectance-absorption spectroscopy (IRAS) for quantitative determination of materials structure and chemical composition.

Vision-Science Laboratory

The vision science laboratory consists of state-of-the-art hardware and software capabilities for carrying out video inspection, multi-spectral image analysis, and sensor-based pattern recognition. (Includes Imaging Processing System, Patent #5,495,536.) These capabilities are used in applications ranging from microsensor-based chemical detection and recognition to automated video/SEM inspection of semiconductor materials and circuits (Patent #5,901,247). This is a new approach to pattern recognition, coupling perception-oriented research with machine algorithms.

Chemical Vapor Deposition (CVD)

Our experimental tools for investigating CVD include optical probes (such as reflectance-difference spectroscopy and emissivity correcting pyrometry) for gas-phase and surface processes, a range of surface analytic techniques, molecular beam methods for gas/surface kinetics, and flow visualization techniques. These tools are integrated in a unique manner with research CVD reactors and with advanced chemistry and fluid models.

Growth Science Laboratory

Capabilities for in situ characterization of materials during thin film deposition, molecular beam epitaxial growth, and low energy ion beam simulated growth, include intensity profile sensitive reflection high energy electron diffraction (RHEED) for surface structure, energy dispersive x-ray reflectrometry for in situ surface and interface structure, multibeam wafer curvature for strain (Patent #5,912,738), and Auger electron spectroscopy for surface composition.

KMAP X-ray Diffractometer

Based on double crystal x-ray diffractometry in combination with position sensitive x-ray detection, our KMAP x-ray diffraction analysis is used to determine the lattice constant, strain relaxation, composition, layer orientation, and mosaic spread for a large variety of advanced epitaxial semiconductor material systems.

Nanoelectronics Laboratory

We have the capabilities for fabrication of nanoscale quantum device structures, together with capabilities for ultra-low-noise measurement of transport from 0.3 Kelvin to ambient at high magnetic fields.

Lasers and Optics

We provide characterization and advanced understanding in the area of solid-state lasers and non-linear optics, especially as coherent sources of broadly tunable light in rugged, compact geometries. We also have established expertise in long-term and transient radiation effects characterization of optical materials. (Includes patented Wavefront Sensor Patent #5,493,391, and Monolithic Optical Amplification Devices Patent #5,463,649.) Capabilities include the widely used (approximately 2000 users worldwide) SNLO (Sandia

Non-Linear Optics) code, which is a lab-tested code for predicting the performance of non-linear optical components. In the area of integrated optical materials, our laboratories produce new types of photosensitive materials (processing patent applied for) for directly-writeable waveguides and reconfigurable optical interconnects.

Laser and Optical Spectroscopies

Our capabilities in characterizing semiconductor materials by photoluminescence and magnetoluminescence extend down to low temperatures by optical laser imaging and laser microscopy, by laser excitation spectroscopy, and by the time-resolved measurements of optical emission. We also have developed a high lateral resolution, near-field scanning optical microscopy (NSOM) capability with time and frequency resolution.

Low-Temperature Plasma Analysis

We have state-of-the-art capabilities for the analysis of low-temperature plasmas as found in commercial processing reactors. These include emission spectroscopy, electrical characterization, laser and microwave-based measurements of species concentrations, in situ electric field measurements, and others. Sandia is the only lab that combines new diagnostics, relevant process chemistries (complex mixtures), and massively parallel (MP) computer models for simulation of continuous and transient plasmas.

— Synthesis and Processing —

Synthetic Organic Laboratory

Novel lipids, surfactants, and other small molecules are prepared in this laboratory via synthetic organic techniques. The laboratory is also capable or forming and characterizing self-organized structures (e.g., liposomes, micelles, self-assembled monolayers, LB films) generated with the newly synthesized molecules in pure or mixed molecular systems.

Biomaterials Laboratory

The Biomaterials Laboratory possesses equipment to perform numerous molecular biology and biochemistry research including genomic DNA, RNA, and plasmid isolation from a variety of sources (e.g., bacteria, viruses, and eukaryotic tissues and ells). DNA sequences can be cloned into a variety of organisms, permitting the manipulation and modification of DNA and protein sequences, structure, and function. Cloned DNA sequences can be genetically engineered using reverse transcription, the polymerase chain reaction and site-directed mutagenesis. Native and recombinant proteins also can be expressed, purified, characterized, and functionalized in this laboratory.

Monolayer Deposition of Organic Films

We have a Langmuir-Blodgett facility for controlled deposition of mono- and multi-layer organic films. The facility includes two computer-controlled troughs, in situ fluorescence microscopy, vibration isolation, and a dust-free down flow work area.

Nanocluster Laboratory

We have developed and patented a process based on the use of inverse micelles for the synthesis of large quantities of monodisperse clusters of metals, semiconductors, and oxides.

Electron Cyclotron Resonance (ECR)

This plasma facility has been built for studying fundamental processes governing the growth of oxide and nitride dielectric films used in optoelectronics and used as hard coatings. This is the only system in the U.S., which combines ECR plus e-beam evaporation.

Molecular Beam Epitaxy (MBE)

We have research semiconductor growth laboratories for ultra-pure and ultra-flexible MBE growth of III-V materials. In addition, we have

research systems for Group IV semiconductor growth.

Metal-Organic Chemical Vapor Deposition (MOCVD)

We maintain research facilities with capabilities in MOCVD of III-V compound semiconductor materials including GaN-based materials and self-assembled quantum dots. These capabilities include research reactors designed specifically for studies of CVD chemistry, fluid dynamics, the development of advanced in situ diagnostics, and the development of advanced semiconductor heterostructures and devices.

Crystal and Thin Film Growth

Capabilities in this area include pulsed laser deposition chambers, a high vacuum metal deposition chamber, a thin film oxide deposition chamber, a diamond-like carbon deposition chamber, a hot filament chemical vapor deposition chamber, and various apparatus for single crystal growth. Our capabilities for stress relief of diamond-like carbon films and structures produced by pulsed laser deposition are not available elsewhere.

400 kV and 180 keV Ion Implanters

These systems are equipped with a variety of sources (gas, sputter, and metal vapor). This facility provides ion species from hydrogen to bismuth that can be used for studying fundamental irradiation mechanisms and selective chemical doping in semiconductors, metals, ferroelectrics, and superconductors.

High Pressure and Shock Wave Physics and Chemistry Laboratories

Our capabilities in this area include large volume static high pressure apparatus which can be operated at temperatures ranging from 2 to 700 K and in magnetic fields, as well as gas gun and explosive loading facilities with state-of-the-art, time-resolved diagnostics. Recovery fixtures have been developed for use with the gas gun and explosive shock loading facilities that allow unique material synthesis over broad ranges of shock pressures and temperatures.

— Theory and Simulation —

Electronic Structure and Linear Scaling

We have developed state-of-the-art massively parallel electronic structure algorithms, based on ab initio pseudopotentials and plane-wave/Gaussian basis functions. These codes are used to develop a fundamental understanding of physical phenomena and materials, including compound semiconductor band structure, diffusion of point defects, dopants and impurities, optoelectronic properties of extended defects, adsorbate interactions on surfaces, bonding at metal-oxide interfaces, and enhanced reactivity of nanoparticles. To allow the investigation of more complex systems and phenomena, we have developed new computationally efficient algorithms, e.g., self-consistent linear scaling density functional theory and variable and real-space gridding.

Molecular Dynamics Simulation

Large scale, classical molecular dynamics simulations using the massively-parallel code LAMMPS (Large-scale Atomic/Molecular Massively Parallel Simulator) are being used to model a wide variety of systems. These classical simulations cover the length and time scale intermediate between quantum and continuum calculations. Systems of current interest include adhesion and friction in self-assembled monolayers, degradation of polymer adhesives, wetting and spreading of multi-component fluids and transport in polymer membranes for fuel cells. Modifications of the algorithm to include particle rotation and friction have been implemented to study granular materials.

Chemical Processes

We have extensive capabilities, including massively-parallel computation, to model complex chemically reacting flows such as occur in chemical vapor deposition manufacturing processes. Our numerical simulations can include the coupled gas-phase and gas-surface chemistry, fluid dynamics, heat, and mass transfer to provide predictive models of a chemical process.

Low-Temperature Plasmas

We have extensive capabilities in massively parallel codes to simulate the time and space evolution of low-temperature plasmas, focusing on new theoretical techniques for achieving rapid convergence and on direct comparisons with experimental results.

Optical and Wave Propagation

We have developed advanced simulation codes for understanding wave propagation in optical parametric oscillators and amplifiers for the purpose of designing highly efficient, tunable laser sources. We also have capabilities in novel optical designs, including resonators for compact laser geometries. These capabilities are coupled to in-house micro-optics construction facilities and state-of-the-art optics testing.

Physical and Chemical Sciences Center
FY03 Budget

Physical and Chemical Sciences Center
FY03 Budget - By Customer

Capital ($1.8M)

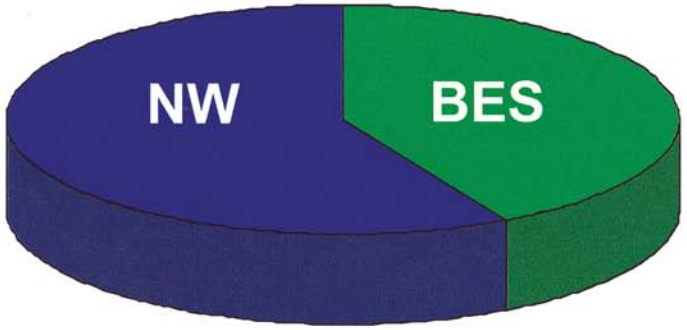

Operating ($36M)

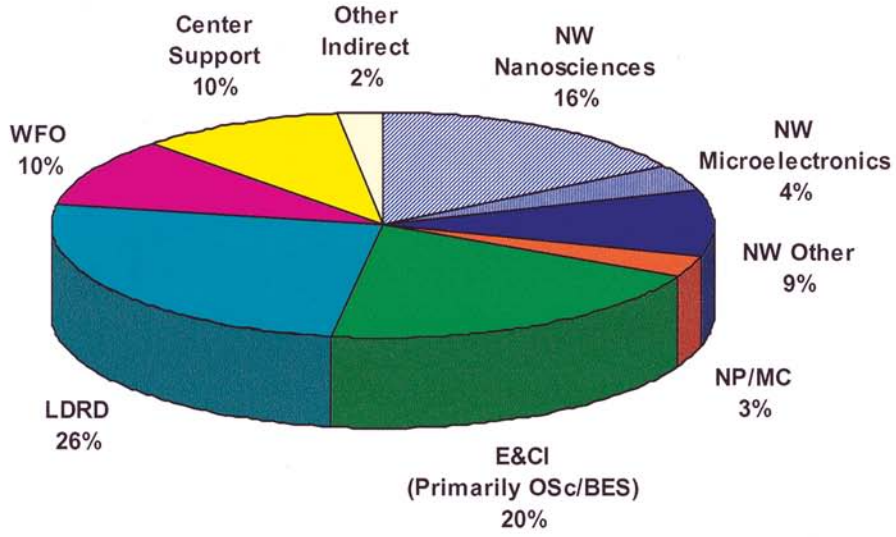

NW	Nuclear Weapons	NP/MC	Nonproliferation & Materials Control	E&CI	Energy & Critical Infrastructure	OSc	Office of Science
BES	Basic Energy Sciences	LDRD	Laboratory Directed Research & Development	WFO	Work for Others		

SAND2003-3949P: Prepared by Sandia National Laboratories, Albuquerque, New Mexico 87185 and Livermore, California 94550. Sandia is a multiprogram laboratory operated by Sandia Corporation, a Lockheed Martin Company, for the United States Department of Energy under Contract DE-AC04-94AL85000

Printed 2003